UNIVERSITY OF WARSAW

DOCTORAL THESIS

Spatial characterization of single photons and entangled photon pairs

Author:
Sanjukta Kundu

Supervisors:
Dr. Radosław Łapkiewicz
Dr. hab. Piotr Fita

A thesis submitted in fulfillment of the requirements for the degree of Doctor of Philosophy

in the

Quantum Imaging Laboratory
Optics Division, Institute of Experimental Physics
Faculty of Physics, University Of Warsaw

October 4, 2023

"I am enough of an artist to draw freely upon my imagination. Imagination is more important than knowledge. Knowledge is limited. Imagination encircles the world."

Albert Einstein

UNIVERSITY OF WARSAW

Abstract

Faculty of Physics
Optics Division, Institute of Experimental Physics

Doctor of Philosophy

Spatial characterization of single photons and entangled photon pairs

by Sanjukta Kundu

Quantum entanglement is a fundamental phenomenon in quantum mechanics. Entangled particles behave as a single unit, regardless of the distance separating them. Over the past few decades, photons have played a leading role in experimental research on quantum entanglement. Entanglement was present in various degrees of freedom, but photons' polarization was most commonly used due to the ease of manipulation of this degree of freedom. The polarization of a single photon is described by a two-dimensional Hilbert space – it allows one to physically realize a qubit. It turns out that higher-dimensional Hilbert spaces open up wider possibilities for transmitting and processing information, and the spatial degree of freedom of a photon can serve as a natural implementation of such "qudits".This thesis focuses on investigating the transverse spatial profiles of single photons and two-photon spatial entanglement. The thesis introduces experimental tools for fundamental research, and at the same time can lead to technological advances of considerable importance in the field of quantum communication and quantum imaging.

This thesis presents three main projects, which focus on characterizing the spatial degrees of freedom of heralded single photons and entangled photon pairs.

In the first project, we explore the quantitative characterization of the spatial profile of heralded single photons. However, this task is particularly difficult for single photons, given their indeterminate global phase. To tackle this issue, we introduce a self-referenced interferometric technique, relying on a single photon interfering with itself, that enables the complete characterization of a two-dimensional probability amplitude of a single photon.

In the second project, we characterize spatially entangled photon pairs generated using spontaneous parametric down-conversion (SPDC). In order to achieve this aim, we develop a hybrid intensified camera setup for observing their spatial correlations with a high acquisition rate. This hybrid single-photon camera combines an image intensifier with a high spatial resolution sCMOS sensor and a high temporal resolution single pixel detector (photomultiplier tube). This combination allows us to monitor and control the number of photons detected within each frame. This camera setup facilitates spatially resolved detection of single photons while increasing the data acquisition rate.

Lastly, we focus on a nonlinear Zou-Wang-Mandel (ZWM) interferometer where we utilize a technique known as quantum imaging with undetected photons (QIUP) for the characterization of quantum correlations. QIUP allows for image formation without requiring the detection of light that has interacted with the object being imaged. Instead, it is rooted in the generation of entangled photon pairs in a quantum superposition, originating from two distinct, spatially separated SPDC sources. In this process, one photon from the SPDC pair (idler photon), interacts with the object under investigation. Remarkably, this idler photon is never detected. Our setup facilitates the analysis of correlations of down-converted photon pairs without relying on coincidence measurements. This is enabled by the fact that the spatial resolution of QIUP is limited by the strength of momentum correlations. A stronger correlation leads to a higher resolution. We employ this interferometric technique for characterizing transverse momentum correlations of photons and also explore possibilities of characterization of high-dimensional entanglement involving orbital angular momentum.

Collectively, these projects expand the toolbox for spatial characterization of single photons and entangled photon pairs, contributing to the ongoing development of quantum communication, quantum imaging, and entanglement research.

Acknowledgements

I would like to express my gratitude to several people without whom my PhD journey would not have been possible.

First of all, I would like to thank my supervisor dr Radek Lapkiewicz for giving me the opportunity to be a part of his research lab and to work on all those exciting research problems. He taught me to ask questions and how to lose neither the big picture nor the small one. I would also like to thank Prof. Piotr Fita for his support and guidance. I thank all the members of the Quantum Imaging Lab group at FUW, past and present. You all contributed to creating a really special, supportive, stimulating, and of course fun atmosphere.

Jerzy Szuniewicz, for being awesome to work with, for all the discussions and cool ideas whenever we faced a seemingly unresolvable problem, and also for being a great friend; Wiktor Szadowiak for being such a chill and efficient co-worker and for all the problem-solving we've done together; Adrian Makowski for being an amazing friend and always being there whenever I needed him, both for research and fun; Aleksandra Sroda for being one of the first friends I made in Poland and making my life easier in a foreign country. And my earnest thank you to all the other members of our group, Paweł Szczypkowski, Stanisław Kurdziałek, Alexander Krupiński-Ptaszek, Bohnishikha Ghosh, Anat Daniel, Monika Pawłowska, Grzegorz Firlik – I have learned from all of you in some way. A special thanks to Inna Kviatkovsky for all the fruitful discussions about the quantum imaging setup.

I would also like to thank the wonderful collaborators I was, and am, privileged to work with; the hugely knowledgeable Prof. Gabriela Barreto Lemos from the Federal University of Rio de Janeiro for being such an amazing and friendly collaborator and for guiding me whenever needed, Prof. Mayukh Lahiri from Oklahoma State University for his theoretical collaboration and astute observations, Prof. Robert Fickler from Tampere University - who has given me the opportunity to join his Experimental Quantum Optics group for an internship. A big thank you to him, Rafael Barros, and everybody else in prof. Fickler's group for their hospitality and kindness.

I also thank all the people with whom I shared an office and had fun – Ali Golestani, without whom bureaucracy would have devoured me, and who showed me the wonders of Persian cuisine, Sanjay Kapoor for office banter and hunting for Indian food when working late hours, Jerzy for making the office so green. Special thanks to Mrs. Halina Przychodzeń for her help in maneuvering the administrative pitfalls; she saved me from certain doom multiple times.

I also want to thank all my friends outside of the lab without whom PhD would not be easy at all – Deeksha, Laura, and Aknur for being my best buddies through all the ups and downs, Sudeep and Kaustav for teaching me how to cook Bengali food. A very special thanks to Sebastian, for all the love, the hugs, smiles, trips, movie nights, being there for me whenever I needed him, and all the wonderful stories he told me.

Finally and most importantly my huge thanks and love to my family – my parents for all your constant support and encouragement throughout my life; my elder brother, Narendra - my best friend and guide; and my elder sister, Sangita, for all her care and love.

Financial support: This work was funded by the First TEAM project "Spatiotemporal photon correlation measurements for quantum metrology and superresolution microscopy" co-financed by the European Union under the European Regional Development Fund (POIR.04.04.00-00-3004/17-00).

European Funds Smart Growth
Republic of Poland
FNP Foundation for Polish Science
European Union European Regional Development Fund

Contents

List of Abbreviations

SPDC	Spontaneous Parametric Down Conversion
SHG	Second Harmonic Generation
OPA	Optical Parametric Amplifier
SNR	Signal-to-Noise Ratio
QE	Quantum Efficiency
EPR	Einstein-Podolsky-Rosen
ppKTP	Periodially Poled Potassium Titanyl Phosphate
BBO	Beta Barium Borate
HWP	Half-wave Plate
QWP	Quarter-wave Plate
BS	Beam-splitter
PBS	Polarizing Beam-splitter
MZI	Mach-Zehnder interferometer
HOM	Hong-Ou-Mandel
QIUP	Quantum imaging with undetected photons
ZWM	Zou-Wang-Mandel
FTPI	Frustrated two-photon interference
NIR	Near-InfraRed
UV	Ultraviolet
MIR	Mid-InfraRed
CW	Continuous Wave

FWHM	Full Width at Half Maximum
SLM	Spatial Light Modulator
OAM	Orbital Angular Momentum
FPGA	Field Programmable Gate Array
OSA	Optical Spectrum Analyser
APD	Avalanche Photodiode
SPAD	Single Photon Avalanche Diode
IsCMOS	Intensified Scientific Complementary Metal-Oxide-Semiconductor
EMCCD	Electron Multiplying Charge-Coupled Device
TEC	Temperature Controller
CAR	Coincidences-to-Accidentals Ratio
FoV	Field Of View

Dedicated to my parents and teachers.

Chapter 1

Introduction

Quantum entanglement is a fundamental phenomenon in quantum mechanics where particles behave as a single unit, regardless of the distance separating them. In quantum studies, photons are particularly valuable due to their unique characteristics [1, 2, 3, 4]. Photons, as quantized packets of energy, possess multiple degrees of freedom – one of the pivotal degrees of freedom that my research focuses on is the transverse spatial degree of freedom. This explores the spatial distribution of their wavefunction and the associated phase patterns. By thoroughly investigating this domain, we aim to analyze both heralded single photons and the spatially entangled photon pairs. This exploration holds potential for advancements in applications such as quantum imaging and wider areas of quantum information processing and communication techniques.

In particular, in this thesis, I present methods conceived for characterizing the spatial degree of freedom of heralded single photons and entangled photon pairs. The study spans from self-referenced interferometric techniques for characterizing single photons (Chapter 2) [5], through a custom-built hybrid intensified camera setup for examining spatial correlations of photon pairs (Chapter 3) [6], to a nonlinear interferometric method using quantum imaging with undetected photons to study spatial correlations without relying on coincidence detection (Chapter 4) [7]. In all of the presented experiments, the key role was played by the careful manipulation of the spatial degree of freedom.

Up next, we'll cover the main elements of quantum optics relevant to this thesis, present the motivation for conducting this work, and introduce the central topics. Further into this chapter, we provide essential theoretical prerequisites to aid in understanding the results discussed in the subsequent parts of the thesis such as the generation of heralded single photons (Chapter 2) and photon pairs (Chapter 3 and Chapter 4) using spontaneous parametric downconversion (SPDC) and spatially resolved single photon detection systems.

1.1 Generating photon pairs with SPDC

Sources based on Spontaneous Parametric Down-Conversion are frequently employed to generate photon pairs that exhibit specific frequency and spatial characteristics. The interaction of a high-energy photon (usually called pump) with a nonlinear crystal during SPDC results in the production of two lower energy photons (usually called signal and idler) (Fig.1.1). The properties of the generated photons depend on both the pump mode and the crystal's properties, making SPDC sources a common choice for producing photon pairs and heralded single photons with defined frequency and spatial attributes [4, 8, 9].

1.1.1 Nonlinear optical process

Parametric downconversion is a nonlinear optical process. Central to the study of nonlinear optics is the relationship between the electric field and polarization which has been covered by many excellent textbooks [4, 2, 3]. I will provide here some essential equations. In a medium, the degree to which it becomes polarized in response to an electric field is termed its electric susceptibility (χ). For simplicity, let's assume P and E are scalar quantities. For a linear optical process within the medium, the polarization is described by:

$$P = \varepsilon_0 \chi E. \tag{1.1}$$

However, when it comes to nonlinear optical processes, higher-order terms are included to account for the nonlinear response of the medium. The polarization can then be expressed as a power series in the electric field i.e., the polarization P induced in the medium not only depends linearly on the electric field strength but also contains components that depend on the second, third, and higher powers of the electric field. It can be mathematically described as:

$$P = \varepsilon_0(\chi^{(1)}E + \chi^{(2)}E^2 + \chi^{(3)}E^3 + \ldots). \tag{1.2}$$

The electric displacement field D is then related to the electric field and polarization as:

$$D = \varepsilon_0 E + P = \varepsilon_0 E + \varepsilon_0\chi^{(1)}E + \varepsilon_0\chi^{(2)}E^2 + \varepsilon_0\chi^{(3)}E^3 + \cdots, \tag{1.3}$$

where $\chi^{(2)}$ and $\chi^{(3)}$ represent the susceptibilities of the second and third-order respectively. We denote, $P^{(2)} = \varepsilon_0\chi^{(2)}E^2$ as the second-order nonlinear polarization, and so forth. Note that above, for simplicity, we assumed P and E are scalar quantities. When representing vector fields, $\chi^{(1)}$, $\chi^{(2)}$, and so forth transform into second-rank, and third-rank tensors, respectively. Using the above equations, let's now see how the wave equation in nonlinear optical media turns out to be.

Let's assume zero charge density ($\rho = 0$), zero current density ($J = 0$), and that the medium is magnetically isotropic, that is, $B = \mu_0 H$. Consequently, Maxwell's equations in the medium can be formulated as:

$$\nabla \cdot \mathbf{D} = 0, \tag{1.4}$$

$$\nabla \times \mathbf{E} = -\mu_0 \frac{\partial \mathbf{H}}{\partial t}, \tag{1.5}$$

$$\nabla \cdot \mathbf{H} = 0, \tag{1.6}$$

$$\nabla \times \mathbf{H} = \frac{\partial \mathbf{D}}{\partial t}. \tag{1.7}$$

Further mathematical analysis when we express the curl of the curl of the electric field as a function of the magnetic field **H** and the electric displacement **D** will provide:

$$\begin{aligned} \nabla \times \nabla \times \mathbf{E} &= -\mu_0 \frac{\partial(\nabla \times \mathbf{H})}{\partial t} \\ &= -\mu_0 \frac{\partial^2 \mathbf{D}}{\partial t^2} \\ &= -\mu_0 \frac{\partial^2(\varepsilon_0 \mathbf{E} + \mathbf{P})}{\partial t^2}. \end{aligned} \tag{1.8}$$

This can be further condensed into the following expression:

$$\nabla(\nabla \cdot \mathbf{E}) - \nabla^2 \mathbf{E} + \mu_0 \varepsilon_0 \frac{\partial^2 \mathbf{E}}{\partial t^2} = -\mu_0 \frac{\partial^2 \mathbf{P}}{\partial t^2}. \tag{1.9}$$

In the scope of linear optics, the divergence of the electric field $\nabla \cdot \mathbf{E} = 0$, thus making the first term of the last equation disappear. Nonetheless, this is not the case for nonlinear optics. Even so, it can be demonstrated that even in nonlinear optics, the contribution from the first term of the equation remains infinitesimally small. Hence, we can simplify the equation to:

$$\nabla^2 \mathbf{E} - \frac{1}{c^2} \frac{\partial^2 \mathbf{E}}{\partial t^2} = \mu_0 \frac{\partial^2 \mathbf{P}}{\partial t^2}. \tag{1.10}$$

This is a wave equation for the electric field in a nonlinear optical medium. In a vacuum where $\mathbf{P} = 0$, we retrieve the standard form of the wave equation. It is often convenient to break down the polarization into its linear ($\mathbf{P}^{(1)}$) and nonlinear ($\mathbf{P}^{NL}$) components. The wave equation then takes the following form:

$$\nabla^2 \mathbf{E} - \frac{(1 + \chi^{(1)})}{c^2} \frac{\partial^2 \mathbf{E}}{\partial t^2} = \mu_0 \frac{\partial^2 \mathbf{P}^{NL}}{\partial t^2}, \tag{1.11}$$

where $n = \sqrt{\varepsilon^{(1)}} = \sqrt{1 + \chi^{(1)}}$ is the refractive index of the medium. The final equation can be viewed as a homogeneous wave equation with an inhomogeneous driving term [4, 8].

Now, let's explore some typical second-order nonlinear optical effects. For simplicity and clarity, we will assume that both the electric field and the polarization are scalar quantities.

1.1.2 Parametric down-conversion as a source of photon pairs

Let's take into consideration a real electric field, $E(t)$, composed of two different frequencies, expressed as follows:

$$E(t) = E_1 e^{-i\omega_1 t} + E_2 e^{-i\omega_2 t} + \text{c.c.} \tag{1.12}$$

In this case, the second-order polarization, $P^{(2)}(t)$, can be derived as:

$$\begin{aligned} P^{(2)}(t) &= \varepsilon_0 \chi^{(2)} E^2(t) \\ &= 2\varepsilon_0 \chi^{(2)} (E_1 E_2^* + E_1^* E_2) + \varepsilon_0 \chi^{(2)} \big[|E_1|^2 e^{-2i\omega_1 t} + |E_2|^2 e^{-2i\omega_2 t} \\ &+ 2E_1 E_2 e^{-i(\omega_1 + \omega_2)t} + 2E_1 E_2^* e^{-i(\omega_1 - \omega_2)t} \big] + \text{c.c.}. \end{aligned} \tag{1.13}$$

From this, the generation of sum frequency $\omega_1 + \omega_2$, difference frequency $\omega_1 - \omega_2$, and second harmonic frequencies, $2\omega_1$ and $2\omega_2$, can be clearly observed.

For the generation of difference frequency at $\omega_3 = \omega_2 - \omega_1$ from the field at frequency ω_1, the presence of the field at ω_2 is not necessarily required. In case it does exist, the difference frequency generation is stimulated by the field at frequency ω_2. This process has high efficiency and is referred to as optical parametric amplification (oscillation).

Even without ω_2, difference frequency generation is possible because the vacuum mode at frequency ω_2 always exists. However, since this process is stimulated by the vacuum mode, its efficiency is quite low, leading to what is called parametric down-conversion.

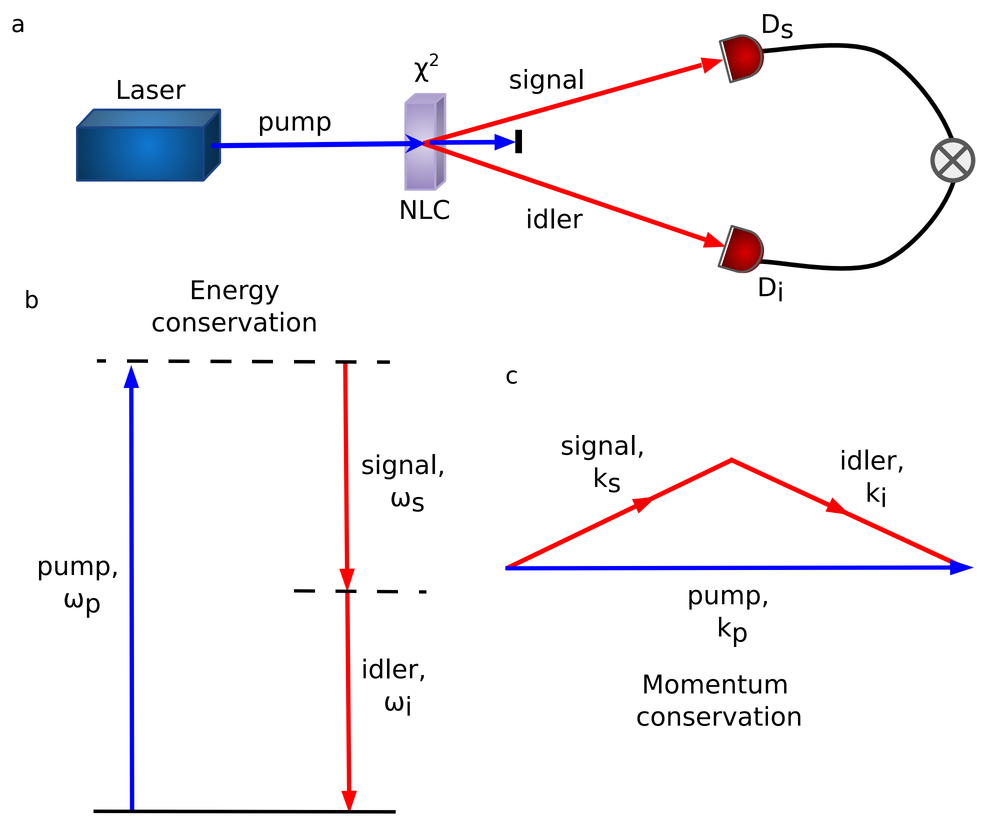

FIGURE 1.1: Spontanous parametric downconversion. **(a)** represents the scheme of down-converted photon pair generation where high energy pump photon after interacting with a nonlinear crystal (NLC) results in the production of two lower energy photons – signal and idler respectively in $\chi^{(2)}$ process. **(b)** and **(c)** represent the constraints of energy and momentum conservation in down-conversion that is the sum of the energies of the signal and idler photons are equal to the energy of the pump photon and that the sum of the momenta of the signal and idler photons are equal to the momentum of the pump photon. These conservation laws result in the two photons entangled in their time - energy, position - momentum, and angular position - OAM degrees of freedom. The phase matching conditions in SPDC can be tailored to ensure that both photons emerge in a direction aligned with the pump, termed collinear phase matching. On the other hand, the two photons can be directed to diverge, known as non-collinear phase-matching. Depending on the requirements, the phase-matching conditions can be set so that the polarizations of the two photons either align (type-I down-conversion) or are perpendicular to each other (type-II down-conversion).

To observe second-order nonlinear effects, the medium must possess a non-zero second-order nonlinear susceptibility. These effects, including the second-order nonlinear polarization, occur only in non-centrosymmetric crystals, i.e., those lacking inversion symmetry. For instance, let's consider a medium that is centro-symmetric and has a finite value of $\chi^{(2)}$. In this case, we would have:

$$P = \varepsilon_0 \chi^{(2)} E^2(t), \tag{1.14}$$

$$-P = \varepsilon_0 \chi^{(2)} (-E)^2, \tag{1.15}$$

which implies $\chi^{(2)} = 0$. Hence, only non-centrosymmetric media can demonstrate second-order nonlinear effects, including parametric down-conversions [9, 10].

1.1.2.1 Types of SPDC pair generation

The interaction of a high-energy photon with a non-linear crystal during SPDC results in the production of two lower energy photons (Fig.1.1).

A wide range of non-linear crystals can be used to generate these photon pairs, such as Beta Barium Borate (BBO), periodically poled potassium titanyl phosphate (PPKTP), Lithium Niobate (LN), and Potassium Dihydrogen Phosphate (KDP). For illustration, let's consider two cases – one with an experimental setup using a photon-pair source with a BBO, and another with a PPKTP crystal both pumped with a UV CW laser at 405nm.

Parametric down-conversion (PDC) is a process where a pump photon decays into a pair of photons, often referred to as signal and idler photons. The interaction between the original and resulting fields is made possible by the non-zero second-order susceptibility of the crystal. The properties of the light emitted are defined by both the energy conservation of the process and the phase-matching condition in the crystal:

$$\omega_p = \omega_s + \omega_i, \tag{1.16}$$
$$\mathbf{k}_p = \mathbf{k}_s + \mathbf{k}_i, \tag{1.17}$$

where ω_α represents the photon frequency, $\mathbf{k}_\alpha$ is the wavevector, and $\alpha = p, s, i$ denote the pump, signal, and idler.

PDC occurs in two forms as mentioned before – spontaneous and stimulated. In the spontaneous case, photon pairs are generated by decay processes. However, in a stimulated scenario, the first photon pair is emitted spontaneously and then serves as a seed for the lower-frequency field, stimulating the generation of other pairs. The spontaneous regime typically has a low probability of generating multiple photon pairs simultaneously.

There are different types of SPDC depending on the polarization of the pump photon (input of the birefringent nonlinear crystal) and the polarization of the signal and idler photons. In the case of type-0 SPDC, the polarization of the pump, signal, and idler are the same, whereas, in type-I, signal and idler photons have the same polarization but orthogonal to the pump, and in type-II, signal and idler photons have orthogonal polarizations.

1.1.2.2 Examples of type-I and type-II SPDC

As an example, here we discuss a non-collinear type-I and type-II BBO crystal as well as a collinear type-II PPKTP crystal pumped with a CW laser with a spectrum centered at 405 nm, which generates non-classical light. This light manifests as infrared photon pairs, with both signal and idler photons of centered wavelengths at 810 nm.

In the context of the BBO crystal and type-I SPDC, phase-matching conditions are met using a pump beam with the property of an extraordinary ray. The matching can be categorized as follows:

$$e \rightarrow o + o \qquad \text{(type I)}$$
$$e \rightarrow o + e \qquad \text{(type II)}$$

For Type-I down-conversion in BBO, a pump beam generates an entangled photon pair – the signal and idler photons. These entangled photons possess opposite momentum components in comparison to the pump photon but they have the same polarization and appear diagonally within the emission cone with the pump photon at the center (Fig.1.2a). Furthermore, their propagation direction depends on their individual frequencies, the refractive indexes of the crystal (represented as n_o for ordinary and n_e for extraordinary), the angle between the pump and the crystal, and the conservation principles (Eq.1.16, and Eq.1.17). The strength of the down-converted photons is also governed by phase-matching conditions, which are connected to the crystal's thickness (in our case it's 1 mm thick BBO) and how fast they travel through it. Since the speed at which light travels is influenced by the index of refraction, Type-I, and Type-II SPDC each have different phase-matching conditions.

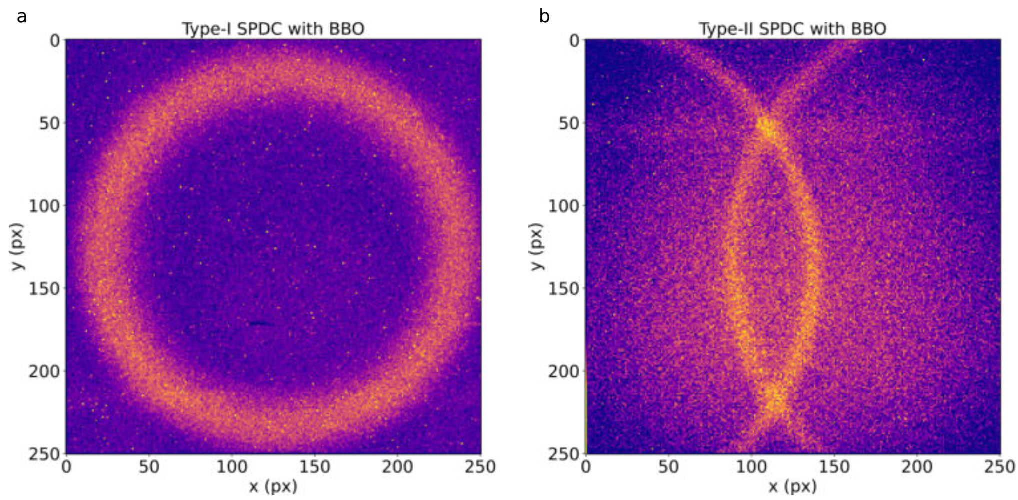

FIGURE 1.2: Spontaneous parametric downconversion with BBO crystal. **(a)** and **(b)** represent the measured intensity distribution of the down-converted photon pairs in the far field in type - I and type - II downconversion respectively.

In type-II down-conversion, the pump beam produces two down-converted photons. These photons can emerge anywhere on their respective cones, but they always appear on opposite sides of the original pump beam direction. One photon will have ordinary polarization, while the other will possess extraordinary polarization. At the points where these two cones intersect – polarisation entanglement occurs (Fig.1.2b).

In the case of a PPKTP crystal pumped with a CW laser centered at 405nm produces a pair of collinear downconverted photons with orthogonal polarisations (type-II). One photon aligns with the pump polarization and the extraordinary axis of the crystal, while the other is cross-polarized along the ordinary axis. This setup, therefore, results in photons with clearly distinguishable polarization states. The spectral properties of the resultant photons depend on the pump's spectral characteristics, the crystal's temperature, and the properties of any spectral filters used in the setup. The energy difference between the two photons can be adjusted by tuning the temperature of the crystal. In terms of spatial distribution, the design of periodically poled crystals, like the PPKTP, is often referred to as quasi phase-matching conditions. This design results in the creation of daughter photons that align collinearly to the pump mode. This alignment facilitates an efficient collection of the photon pairs.

1.2 Spatial correlation of SPDC pairs

In this thesis, while discussing parametric down-conversion, the main focus is on spatial correlations. This process generates photon pairs that show spatial entanglement [8]. The theoretical backdrop of SPDC, beginning with Klyshko's foundational work [11, 12], and developed further by Mandel and coworkers [13], serves as a basis for this exploration.

Over the past twenty years, the study of spatial correlations in photon pairs produced by spontaneous parametric down-conversion (SPDC) has gathered significant attention within the quantum physics community [8]. These spatial correlations, intrinsic to the SPDC process, have implications that stretch from foundational quantum mechanics to practical quantum communication and information processing. The vast dimensionality of the transverse spatial DOF offers two primary avenues for exploration – projection onto discrete bases, exemplified by modal structures such as the Laguerre–Gaussian modes [14, 15]. Additionally, analysis through a continuous basis is defined by the photons' transverse position or momentum [16]. This continuous mode of exploration provides a spectrum of spatial correlations, offering insights into broader patterns and behaviors inherent to SPDC. A particularly intriguing observation has been the demonstration of Einstein–Podolsky–Rosen (EPR) type correlations in the transverse position and momentum of these photon pairs – where Einstein, Podolsky, and Rosen presented a paradox [17]. The EPR paradox arises from a scenario where two entangled particles A and B, once separated, seem to retain instantaneous correlations. If one measures the position of particle A, the position of particle B becomes instantly determined, and similarly for momentum. This presents a dilemma because, according to the Heisenberg uncertainty principle, one cannot know both the position and momentum of a particle with absolute certainty. The paradox suggests that if quantum mechanics is correct, then it might be incomplete, as it can't describe these simultaneous determinate values. EPR's argument thus challenges the foundational principles of quantum mechanics and raises questions about the nature of reality, locality, and the completeness of quantum descriptions [18]. The presence of EPR-type spatial correlations is indicated when the inequality below is violated, as detailed in references [19, 20, 21]:

$$\Delta^2(\rho_1|\rho_2)\Delta^2(q_1|q_2) > \frac{1}{4}. \tag{1.18}$$

In the context of quantum mechanics, we can consider the variable ρ to represent the position and q to be its Fourier conjugate, representing the momentum. The conditional uncertainty in the position of system 1, given a measurement of system 2 at position ρ_2, is denoted by $\Delta^2(\rho_1|\rho_2)$. This represents the variance of the conditional probability distribution $P(\rho_1|\rho_2)$ for a well-defined value of ρ_2. Likewise, the variance in the momentum of system 1 conditioned upon a measurement of system 2 at momentum q_2 is given by $\Delta^2(q_1|q_2)$. This denotes the variance of the conditional probability distribution $P(q_1|q_2)$. If the inequality (Eq.1.18) is breached, it suggests the capability to predict the position ρ_1 or momentum q_1 from the respective measurements of position ρ_2 or momentum q_2 better than one would naively expect from the uncertainty principle. Moreover this information about the state of a distant system can be obtained irrespective of the spatial separation between the two systems. This observation contrasts with classical expectations, where such correlations would necessitate a local causal mechanism. In the quantum context, however, this strong correlation between ρ_1 and ρ_2 or q_1 and q_2 without a clear causal link becomes the core of the EPR paradox.

Building on the implications of the EPR paradox, the concept of spatial entanglement has been explored and evidenced. By scanning detectors in two conjugate planes and studying intensity correlations, researchers have checked for non-separability or EPR criteria [16, 19, 22]. Later, this also has been done with EMCCD [23, 24] and ICCD cameras [25, 26].

In SPDC sources, photon pairs exhibit unique behavior. Close to the source (in the near field), signal and idler display a strong position correlation because both photons originate from the same pump photon. In the far field, they show an anti-correlation: if one photon is detected at a position ρ, its counterpart is likely detected at position $-\rho$. This anti-correlation in the far field can be attributed to phase matching, a manifestation of momentum conservation in the SPDC process (Eq.1.17). From a mathematical perspective, the Hilbert space used to describe the spatial properties of the two-photon states is essentially a tensor product of the individual Hilbert spaces of each photon, represented as $H_1 \otimes H_2$. The assumption here is that these photons are distinguishable, either by their direction of propagation or by their polarization.

Thus, the two-photon state can be described using the function [8]:

$$|\Psi\rangle = \int\int d\boldsymbol{\rho}_1 d\boldsymbol{\rho}_2 \Psi(\boldsymbol{\rho}_1, \boldsymbol{\rho}_2) |\boldsymbol{\rho}_1\rangle_1 |\boldsymbol{\rho}_2\rangle_2 , \tag{1.19}$$

where $\Psi(\boldsymbol{\rho}_1, \boldsymbol{\rho}_2) = \langle \boldsymbol{\rho}_1, \boldsymbol{\rho}_2 | \Psi \rangle$ is the normalized wave function, and $|\boldsymbol{\rho}_1\rangle_1$ and $|\boldsymbol{\rho}_2\rangle_2$ specify the positions of the photons 1 and 2, – signal and idler respectively. Drawing insights from prior research, a Gaussian model has been widely adopted and utilized to depict the spatial structure of the photon pair emanating from the crystal. The pump's transverse spatial distribution is assumed to be a circularly symmetric Gaussian function of x and y. So the spatial structure of the two-photon field can be given as [19, 27, 24]:

$$\Psi(\boldsymbol{\rho}_1, \boldsymbol{\rho}_2) = N \exp\left[-\frac{|\boldsymbol{\rho}_1 + \boldsymbol{\rho}_2|^2}{4\sigma{+}^2}\right] \exp\left[-\frac{|\boldsymbol{\rho}_1 - \boldsymbol{\rho}_2|^2}{4\sigma{-}^2}\right]. \tag{1.20}$$

Here, $N = \frac{1}{\pi\sigma_-\sigma_+}$ acts as a normalization constant. The variable $\boldsymbol{\rho}_i = (x_i, y_i)$ refers to the transverse location of the i^{th} photon, where i is either 1 or 2. The values $\sigma_\pm$ are the standard deviations of the Gaussians, and they represent the correlations in momentum (given by σ_+^{-1}) and position (given by σ_-), respectively.

Further, while σ_+ is determined by the standard deviation of the Gaussian distribution of the pump laser, denoted as σ_p with a corresponding wavelength λ_p, σ_- is defined as:

$$\sigma_- = \sqrt{\frac{\alpha L \lambda_p}{2\pi}},$$

– L describes the length of the SPDC crystal, and α is an empirically determined adjustment constant [24]. The model outlined in Eq.1.20 has been identified as the two-photon SPDC field transverse wave function when the pump beam is Gaussian, as documented in prior literature [28, 19, 27]. Finally, the practicality of simultaneous photon detection is proportional to:

$$P(\boldsymbol{\rho}_1, \boldsymbol{\rho}_2) \propto |\Psi(\boldsymbol{\rho}_1, \boldsymbol{\rho}_2)|^2. \tag{1.21}$$

1.3 Detection systems for spatial correlation measurement

The task of characterizing photon pairs with correlated transverse spatial modes is not straightforward. It typically requires detectors that can resolve individual photons both in time and position. Analyzing spatial entanglement often involves measuring intensity correlations. One common method involves scanning single-pixel detectors across conjugate planes, exploring the position and momentum correlations [16]. However, over the years there have been quite a lot of advancements in single photon detection technology. Key examples of such devices include electron-multiplying charge-coupled devices (EMCCD) [23, 24], intensified CCD (ICCD) [25, 26], intensified scientific complementary metal oxide semiconductor (IsCMOS) cameras [29, 30, 31], intensified high-speed Timepix cameras [32, 33, 34, 35], and single-photon avalanche diode (SPAD) arrays [36, 37, 38, 39].

Let's discuss briefly some of the above-mentioned devices in regard to detecting individual photons with high spatial and temporal resolution.

1.3.1 EMCCD and ICCD or IsCMOS

Electron-multiplying CCD (EMCCD) cameras can achieve quantum efficiencies of more than 90%. EMCCD cameras can detect single photons. They also produce dark current which is unwanted signal from the camera itself, not from incoming photons. Cooling the camera helps reduce this dark noise, improving its low-light performance.

EMCCD, ICCD, and IsCMOS are imaging technologies designed for low-light conditions, utilizing different mechanisms of operation. In EMCCD cameras, signal amplification is achieved within the CCD chip. Electrons, generated from captured photons, move across the chip and undergo impact ionization in regions with elevated voltages, leading to an increased electron count and thus amplifying the signal. This amplification process, while efficient, introduces a measure of noise, yet it remains relatively low according to Daigle 2009 [23]. For optimal performance, EMCCD cameras are operated in low light and cooled to minimize thermal noise, enhancing the detection of signals from individual photons.

On the other hand, Intensified CCD (ICCD) and sCMOS cameras utilize a photocathode to convert incoming photons to electrons [29]. These electrons are then multiplied in a micro-channel plate (MCP), a separate electron-amplifying component, before they hit a phosphor screen, which turns them back into photons. The CCD or sCMOS chip then detects these photons. The electron multiplication within the MCP introduces statistical noise, a characteristic of the stochastic multiplication process [40]. Additionally, the incorporation of components such as the MCP and photocathode can elevate the cost of ICCDs or IsCMOS cameras. These components can also degrade faster when subjected to bright light sources.

Both types of cameras, though different in operation, have been used to characterize spatial entanglement of photon pairs produced in SPDC [24, 41, 30, 31, 25].

These cameras are designed with a focus on spatial resolution. Yet, they have their limitations, especially when it comes to frame rate. Their frame rate, however, is constrained by the readout speed of the CMOS or CCD sensor. To detect photons that are created simultaneously, the camera must be gated once for each frame, setting a specific period to detect coincidences [29]. This gating is essential for identifying the exact time relation between detected events. A notable downside is the low-duty cycle caused by this gating. The length of time the intensifier is gated, known as the gating time, sets the detection window for coincident photons.

Keeping the photon flux low, typically below one photon pair for every active window, reduces the risk of accidental coincidences. However, a drawback is that many frames end up without any photon detections, leading to longer measurement times to gather sufficient data. This often complicates tasks like coincidence imaging, especially when trying to map the spatial correlations of photon pairs from processes like SPDC.

1.3.2 SPAD arrays

In recent years, Single-Photon Avalanche Diodes (SPADs) have gained significant traction in the scientific community, predominantly due to their excellent temporal resolution and efficiency in photon detection [42]. At their core, SPADs operate in Geiger mode, making them exceptionally sensitive, and capable of detecting and counting individual photons in low-light environments. Placing multiple SPADs onto a single chip results in what is known as a SPAD array. These arrays, made using standard CMOS technology, can monitor photon events over a larger area, giving a detailed record of photon interactions across the sensor [36, 37].

So, how does a SPAD function? When a photon interacts with the diode, it sets off an 'avalanche' current due to the substantial electric field across the diode. This current is essentially an alert, signaling the arrival of a photon. As technology progressed, the need to not just detect, but also to timestamp these photon interactions emerged – time-tagging SPAD arrays. These SPAD arrays can detect photons' precise moment of arrival, often with an accuracy of picoseconds [38].

In comparison, while intensified CCD or CMOS cameras have the advantage of high pixel counts and sub-nanosecond gating times, their low duty cycles result in prolonged data acquisition times. In contrast, SPAD arrays excel in capturing rapid temporal changes through asynchronous readout, but this method restricts their spatial resolution. To achieve higher resolutions, on the scale of megapixels, a gating mechanism is imperative for these SPAD arrays. Thus, the challenge lies in optimizing both time and spatial resolutions concurrently. In summary, as technology keeps evolving, tools like time-tagging SPAD arrays are pushing the boundaries, enabling the task of coincidence imaging such as the spatial correlation of photon pairs produced via SPDC [39].

1.3.3 Timepix cameras

Timepix cameras are a specific type of hybrid pixel detector developed as part of the Medipix collaboration, an initiative associated with CERN. They are designed to capture and timestamp individual quantum events, such as photon or particle interactions, with high spatial and temporal resolution [32, 33, 34]. The Timepix camera operates based on a hybrid pixel detector, where each pixel functions independently to both detect and process signals. For single photon detection, when a photon strikes the detector, it generates an electronic signal within a specific pixel. The Timepix chip then records the spatial location of this interaction and the exact time of arrival. This is achieved by maintaining an electronic clock within the camera, which timestamps each photon event down to nanosecond precision. The combination of spatial and temporal data means that each photon can be precisely located in both space and time. Thus, Timepix cameras can capture highly detailed, time-resolved images of photon events, making them particularly useful for experiments that require single-photon sensitivity and high temporal resolution (down to tens of nanoseconds). Timepix cameras typically feature a 256×256 pixel which is still less than CCD or CMOS cameras. In recent work, researchers used such a time-stamping camera to show position-momentum EPR correlations and quantify the entanglement of formation [35].

With advancements in camera systems and photon sources, quantum-inspired imaging techniques are becoming vital in research and development. They are becoming crucial components of the ongoing quantum revolution, alongside quantum computing, quantum communication, and metrology.

1.4 One and two-photon interference

One of the fundamental properties of quantum mechanics is the quantum interference effect which can be described in terms of indistinguishability – if an event happens in more than one alternative way and we can not distinguish between the alternatives in any way, then interference takes place. Going back to Young's double-slit experiment, Feynman spoke of interference as "has in it the heart of quantum mechanics. In reality, it contains the only mystery" [43].

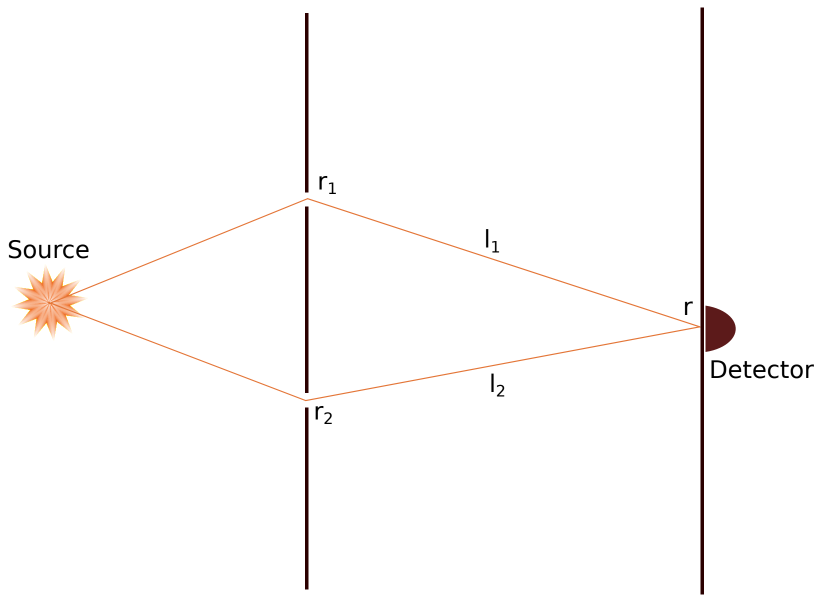

FIGURE 1.3: Sketch of the Young's double-slit experiment.

1.4.1 Overview of classical coherence and the Young's double-slit experiment

Let's start by revisiting the classical theory of coherence, using the Young's double-slit experiment as an illustrative example (Fig.1.3). In specific scenarios, one can observe interference patterns on the screen. Let the source's bandwidth be denoted by $\Delta\omega$, and let the path-length difference between the two slits be given by $\Delta l = |l_1 - l_2|$. Fringes have maximum visibility when $\Delta l \leq \frac{c}{\Delta\omega}$ is satisfied. The bandwidth determines the visibility of fringes that gradually disappear when the path length increases.

Here, the coherence length is defined as $\Delta l_{\text{coh}} = \frac{c}{\Delta\omega}$, and the corresponding coherence time is $\Delta t_{\text{coh}} = \frac{\Delta l_{\text{coh}}}{c} = \frac{1}{\Delta\omega}$.

Assuming that the polarization of the fields is uniform and that we can neglect diffraction effects at the slits (assuming their sizes to have the dimensions of the order of the wavelength of the light), the electric field at point r and time t on the detection screen can be represented as a linear combination of the electric fields originating from the slits at earlier times $t_1 = t - \frac{l_1}{c}$ and $t_2 = t - \frac{l_2}{c}$:

$$E(r,t) = K_1 E(r_1, t_1) + K_2 E(r_2, t_2). \tag{1.22}$$

Here, $E(r_i, t_i)$ stands for the complex electric field reaching the screen from the i-th slit, and K_1 and K_2 are complex factors depending on the path lengths l_1 and l_2, respectively.

Given that optical detectors measure average light intensity due to their long response times, the intensity $I(r)$ at point r can be represented as:

$$I(r) = \langle |E(r,t)|^2 \rangle. \tag{1.23}$$

For the purpose of this derivation, we assume normalized field intensities. Hence, the factor $\frac{1}{2}\epsilon_0 c$ is effectively set to 1. $\langle \cdot \rangle$ indicates time averaging. Assuming ergodicity, this time average also serves as an ensemble average. In this context, the ensemble average refers to the average over multiple realizations of the incident light wave due to statistical variations inherent in the source.

Using Eq.1.22, the intensity can be broken down as:

$$I(r) = |K_1|^2 \langle |E(r_1,t_1)|^2 \rangle + |K_2|^2 \langle |E(r_2,t_2)|^2 \rangle + 2\text{Re}\left[K_1^* K_2 \langle E^*(r_1,t_1) E(r_2,t_2) \rangle\right]. \tag{1.24}$$

Let's define individual intensities as $I_1 = |K_1|^2 \langle |E(r_1,t_1)|^2 \rangle$ and $I_2 = |K_2|^2 \langle |E(r_2,t_2)|^2 \rangle$.

Introducing the normalized first-order mutual coherence function $\gamma^{(1)}(r_1, r_2)$ as:

$$\gamma^{(1)}(r_1, r_2) = \frac{\langle E^*(r_1) E(r_2) \rangle}{\sqrt{\langle |E(r_1)|^2 \rangle \langle |E(r_2)|^2 \rangle}}. \tag{1.25}$$

This allows us to express the measured intensity in a more compact form:

$$I(r) = I_1 + I_2 + 2\sqrt{I_1 I_2} \left|\gamma^{(1)}(r_1, r_2)\right| \cos(\phi - \Delta\psi), \tag{1.26}$$

where $\phi = \arg(\gamma^{(1)}(r_1, r_2))$. The phase difference $\Delta\psi$ is defined as:

$$\Delta\psi = \psi_1 - \psi_2, \tag{1.27}$$

with ψ_1 and ψ_2 representing the phases of the light waves arriving at the detection screen from slits 1 and 2, respectively.

Interference will be observed when $|\gamma^{(1)}(r_1, r_2)| \neq 0$.

The fringe visibility V is:

$$V = \frac{I_{\max} - I_{\min}}{I_{\max} + I_{\min}}. \tag{1.28}$$

The maximum and minimum intensities are:

$$I_{\max/\min} = I_1 + I_2 \pm 2\sqrt{I_1 I_2} \left|\gamma^{(1)}(r_1, r_2)\right|. \tag{1.29}$$

Therefore, the visibility can be written in a more simplified form as:

$$V = \frac{2\sqrt{I_1 I_2}\,\left|\gamma^{(1)}(r_1, r_2)\right|}{I_1 + I_2}. \tag{1.30}$$

For a complete coherence, $|\gamma^{(1)}(r_1, r_2)| = 1$ which implies visibility to be maximum:

$$V = \frac{2\sqrt{I_1 I_2}}{I_1 + I_2}. \tag{1.31}$$

For no coherence, $|\gamma^{(1)}(r_1, r_2)| = 0$ making visibility, $V = 0$

1.4.2 One-Photon Interference

As described previously, in the quantum description, light is treated as a collection of photons. Single-photon interference can be understood using quantum mechanics. When a photon travels through the double-slit, its state can be represented as a superposition of the states corresponding to the transition through each slit. Mathematically, if the photon travels through slit r_1, its state is represented by $|r_1\rangle$, and if it travels through slit r_2, its state is represented by $|r_2\rangle$. The overall state of the photon is then given by:

$$|\psi\rangle = c_1 |r_1\rangle + c_2 |r_2\rangle\,, \tag{1.32}$$

where c_1 and c_2 are probability amplitudes associated with the photon traveling through slits r_1 and r_2 respectively.

The probability of detecting a photon at point r on the screen is proportional to $|\langle r|\psi\rangle|^2$. The term $\langle r|\psi\rangle$ quantifies the amplitude of detecting the photon at position r on the screen due to its state's superposition when passing through the slits. When multiple photons are successively sent through the slits, an interference pattern gradually forms on the detection screen. This pattern arises from the combination of the probability amplitudes c_1 and c_2 related to each slit, highlighting the inherent quantum behavior of light.

1.4.3 Two-Photon Interference

Two-photon interference (a bi-photon interfering with itself) involves more complex quantum states often described by entangled states. Imagine an experiment where two photons, a and b, are simultaneously emitted and they each have a choice of two paths to travel, denoted by r_1 and r_2. Let's consider an entangled state of these two photons:

$$|\Psi\rangle = \frac{1}{\sqrt{2}}\left(|r_{1a}, r_{2b}\rangle + |r_{2a}, r_{1b}\rangle\right) \tag{1.33}$$

In this expression, r_{ia} and r_{ib} refer to the states of photon a and b passing through slit i, respectively. The state represents a superposition where either photon a goes through r_1 and photon b goes through r_2, or vice versa.

The property of this entangled state is that the photons are intrinsically linked; neither photon in this setup has a well-defined path until a measurement is made. Due to the nature of their entangled state, measuring the path of one photon immediately reveals the path of its counterpart. The probability distribution of detecting the two photons jointly will exhibit interference patterns that depend on both a and b photons.

Some of the popular two-photon interference experiments are the Hong-Ou-Mandel effect [44], induced coherence without induced emission [45], and frustrated two-photon creation experiment [46].

1.4.3.1 The Hong-Ou-Mandel (HOM) interference

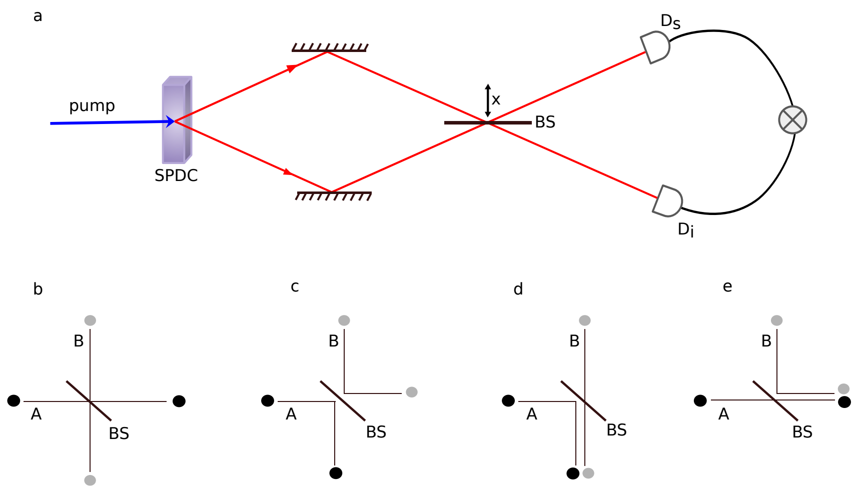

FIGURE 1.4: Hong-Ou-Mandel (HOM) interference with SPDC photons. (a) Experimental setup depicting entangled photons from SPDC source directed to a beam splitter (BS) and subsequently detected by D_s and D_i. (b-e) Possible outcomes of photon paths after interaction with the beam splitter, labeled with inputs A and B. The observed result is the photons leaving together from the same output, showcasing quantum interference.

The Hong-Ou-Mandel (HOM) interference (Fig.1.4a), first observed by Hong, Ou, and Mandel in 1987, stands as a foundational experiment in quantum optics that delves into the intricate behavior of photon pairs at a beam splitter [44]. In the setup, each photon is directed into a separate input port of the beam splitter, leading to four potential outcomes: both photons could be transmitted (Fig.1.4b), both could be reflected (Fig.1.4c), or one could be transmitted while the other is reflected (Fig.1.4d and Fig.1.4e). The initial state of the photons can be represented as $|1_A, 1_B\rangle$, where 1_A and 1_B signify a single photon in each input mode A and B, respectively. As they pass the beam splitter, the state evolves to:

$$\frac{1}{\sqrt{2}}\left(|2_A, 0_B\rangle + |0_A, 2_B\rangle\right).$$

Here, $|2_A, 0_B\rangle$ corresponds to both photons exiting from mode A and none from mode B, while $|0_A, 2_B\rangle$ indicates both photons exiting from mode B and none from mode A. Intriguingly, the scenarios where both photons are either transmitted or reflected are indistinguishable, leading to amplitude addition. At a beam splitter, a reflected photon undergoes a π-phase shift due to the change in its momentum, in contrast to a transmitted photon, which retains its initial phase [47]. This results in destructive interference, causing the amplitudes of the two indistinguishable scenarios to cancel each other out when of equal magnitude. Consequently, the only observed result is both photons leaving from the same output port. This behavior occurs because only two of the four possible outcomes for the photons cancel each other out, ensuring they leave together. This cancellation process and the inability to determine the exact path of each photon is a direct observation of the quantum interference effect.

1.4.3.2 The Induced Coherence without Induced Emission – The Zou-Wang-Mandel Experiment

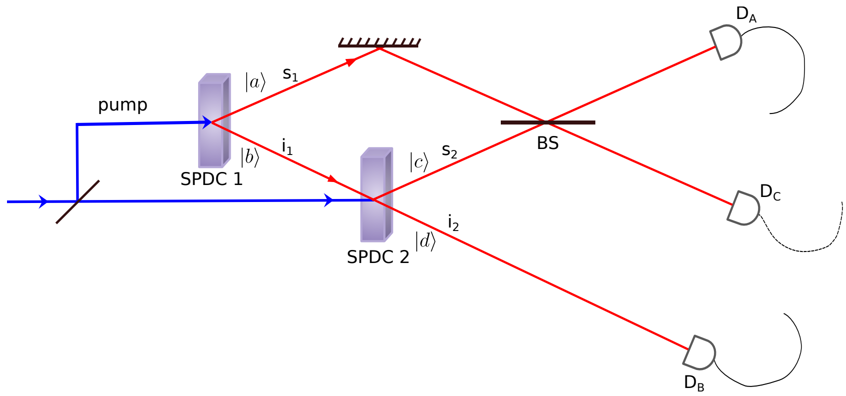

FIGURE 1.5: Schematic representation of the Zou-Wang-Mandel experiment demonstrating induced coherence without induced emission. Two spontaneous parametric downconversion sources (SPDC 1 and SPDC 2) generate photon pairs. The paths of the idler photons from each pair, originating from SPDC 1 (path b) and SPDC 2 (path d), are overlapped, making them indistinguishable and inducing coherence. Paths a and c represent the corresponding signal photons from SPDC 1 and SPDC 2, respectively.

In 1991, Zou, Wang, and Mandel demonstrated an experiment employing two photon-pair sources, specifically spontaneous parametric downconversion sources (SPDC), demonstrating the principles of path identity [45]. The paths of one photon from each pair, originating from the different sources (SPDC 1 or SPDC 2 as shown in Fig.1.5), are overlapped with each other so that it is impossible to distinguish which source they came from. This is how coherence is induced between the idler beams i1 and i2 (from paths b and d, respectively) from the two SPDC sources, without any direct interaction between them. Specifically, in this setup, each pair of photons is created in a superposition state from either of the two SPDC sources. For instance, if SPDC 1 generates photons on paths a and b, and SPDC 2 on paths c and d, the paths b and d are overlaid, yielding the path identity $|b\rangle \to |d\rangle$. The resulting state is

$$|\psi\rangle = \frac{1}{\sqrt{2}}(|a,d\rangle + |c,d\rangle) = \frac{1}{\sqrt{2}}(|a\rangle + |c\rangle)|d\rangle. \tag{1.34}$$

If a phase shift of ϕ is introduced to path d, the state is modified to:

$$|\psi\rangle = \frac{1}{\sqrt{2}}(|a,d\rangle + e^{i\phi}|c,d\rangle) = \frac{1}{\sqrt{2}}(|a\rangle + e^{i\phi}|c\rangle)|d\rangle. \tag{1.35}$$

In the states $|a,d\rangle$ and $|c,d\rangle$, the notations refer to the paths of the photons from the SPDC sources. Specifically, $|a,d\rangle$ denotes the signal photon $s1$ on path a and the idler photon $i1$ on path d, while $|c,d\rangle$ represents the signal photon $s2$ on path c and the idler photon $i2$ on path d. The expression $|\psi\rangle = \frac{1}{\sqrt{2}}(|a\rangle + |c\rangle)|d\rangle$ indicates that the idler photon (either $i1$ or $i2$) is definitively on path d, while the corresponding signal photon is in a superposition of being either on path a (from SPDC1) or path c (from SPDC2).

This experiment demonstrates that the overlap of photon paths can induce coherence between photons from different sources, even without the photons directly interacting. The induction of coherence in the Zou-Wang-Mandel experiment is a direct consequence of making the paths of the idler photons from the two SPDC sources indistinguishable. When the paths overlap and the origins of the idler photons can't be determined, the system manifests coherence. This phenomenon highlights how quantum systems can exhibit coherence solely based on path indistinguishability. The detailed procedure and implications of this experiment are discussed further in chapter 4.

1.4.3.3 Frustrated downconversion: Interference in photon pair creation

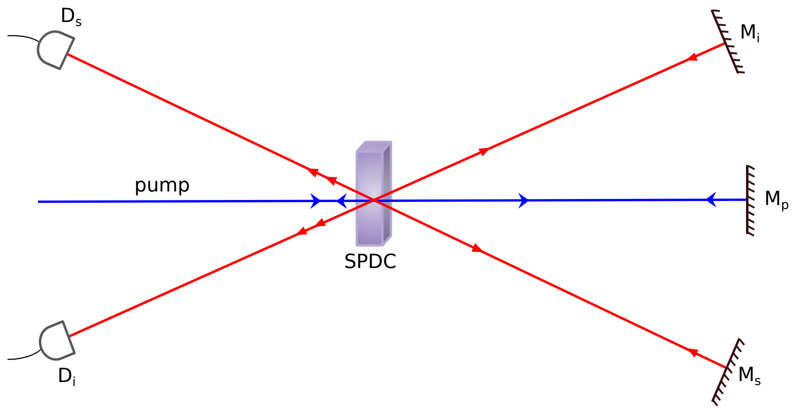

FIGURE 1.6: Schematic representation of the frustrated downconversion experiment: interference in photon pair creation. A pump beam interacts with a single nonlinear crystal responsible for spontaneous parametric downconversion (SPDC). On its first interaction, the pump generates the forward-going signal-idler photon pair (s1, i1). These photons (s1 and i1) are then reflected back into the crystal by mirrors M_s and M_i, respectively. Concurrently, after being reflected by mirror M_p, the pump beam re-enters the crystal, producing a second signal-idler pair (s2, i2). The resulting photons from the two interactions and their traversals through the crystal are detected by the detectors D_s for the signal and D_i for the idler. This configuration leads to quantum interference effects in the photon-pair production.

In the context of two-photon interference, the frustrated downconversion experiment presents an interesting case. Building on the seminal work by Zou, Wang, and Mandel's interference experiment, Herzog et al. demonstrated another fascinating phenomenon involving quantum interference, where both paths of the photon pairs are distinguishable based on their passage direction through the nonlinear crystal [46]. The experimental configuration, depicted in Fig.1.6, employs a single nonlinear crystal. Both the pump beam and the resulting downconverted photon pair (signal and idler photons) are engineered to make a double-pass through this single crystal. The interesting aspect here is the phase manipulation, represented by ϕ, which has the potential to either inhibit or enhance the creation of photon pairs.

The resulting quantum state can be mathematically represented as:

$$|\Psi\rangle = \frac{1}{\sqrt{2}}\left(|a,b\rangle + e^{i\phi}|a,b\rangle\right) = \frac{1}{\sqrt{2}}|a,b\rangle\left(1 + e^{i\phi}\right). \tag{1.36}$$

What makes this experiment notable is the potential for complete suppression of photon-pair production due to destructive interference. Alternatively, when constructive interference occurs, the intensity of the SPDC photons can be maximized. This maximum intensity is four times greater than what would be expected if the photon pairs from each pass through the crystal were produced independently and without interference. This enhancement stems from the coherent superposition of the amplitudes from both passes. When these amplitudes constructively interfere, the combined amplitude becomes twice that of a single pass. Given that the intensity is proportional to the square of the amplitude, this doubled amplitude leads to a four-fold increase in intensity compared to a scenario where only a single pass occurs without interference.

It is noteworthy that the phase ϕ in Eq.1.36 is defined as $\phi = \phi_p - \phi_s - \phi_i$, where ϕ_i and ϕ_s are phases for the idler and signal beams, and ϕ_p is the phase for the pump beam. Additionally, the symbols k_p, k_i, and k_s denote the wavevectors associated with the pump, idler, and signal beams, respectively. The phase-matching condition $k_p - k_i - k_s = 0$ ensures that the relative phases of these beams, as dictated by ϕ, remain in a specific relationship throughout the length of the crystal – serves as a prerequisite to maintain this phase relation throughout the crystal length.

This experimental scheme is used and explained in more detail in chapter 4.

Chapter 2

Characterization of the spatial structure of single photons

Quantitative characterization of the spatial structure of single photons is an important resource to facilitate free-space quantum optical communication [48, 49, 50, 51, 52], quantum computing [53, 54], quantum imaging [55, 25, 56, 26, 57], and quantum metrology [58, 59, 60]. However, the complete characterization of the two-dimensional spatial structure of a single photon presents a formidable challenge due to the inherent indeterminacy of its global phase [61].

Among the solutions to this problem are techniques using weak measurements [62, 63, 64], tomographic techniques [65, 66, 67], and quantum two-photon interference [61, 68]. Unfortunately, classical interferometric methods renowned for their reliability and precision have never been successfully applied to the characterization of a single photon's spatial wave function. However, both these weak measurement and tomographic approaches lack the straightforwardness and precision that classical interferometric methods are known for [69]. Quantum two-photon interference, as demonstrated in recent works, involves overlapping an unknown photon that has an arbitrary spatial phase profile with a reference photon possessing a constant phase profile (flattened spatial phase profile) [61, 68]. However, this method requires the reference photon to be identical to the unknown photon in all degrees of freedom except the spatial one, making the experimental preparation of the reference photon quite difficult.

In this chapter, an interferometric technique is introduced with the goal of achieving the complete characterization of the two-dimensional probability amplitude of single photons [5]. The approach reconstructs the spatial phase of single photons by utilizing the lowest-order interference fringes.

Contrasting with approaches that employ a reference photon for phase measurement, the presented technique is based on a single photon interfering with itself [5]. This fundamental difference results in practical implications, such as the elimination of the need for reference photon generation and coincidence detection, and exhibits higher loss tolerance compared to methods like those described in [61].

The manuscript of the research work presented in this chapter has been published in a peer-reviewed journal named Quantum [5].

2.1 Concept

To reconstruct the unknown spatial phase $\phi(x, y)$ of a single photon beam with the probability amplitude, $\psi_u(x, y) = |\psi_u(x, y)|e^{i\phi(x,y)}$ the schematic interferometric system is presented, as illustrated in Fig. 2.1. A spatial filter is placed in one arm of the Mach-Zehnder interferometer, ensuring the filtered photon carries only a flat phase profile. Consequently, a reference beam is created, characterized by a probability amplitude $\psi_r(x,y) = |\psi_r(x,y)|e^{i\phi_0}$, with ϕ_0 as a constant spatial phase.

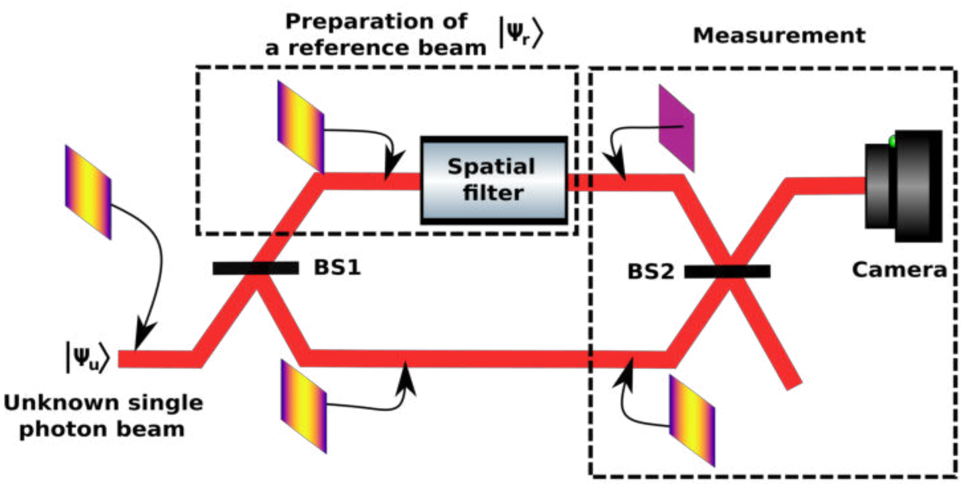

FIGURE 2.1: Schematic representation of the experiment. An incoming beam of single photons with an unknown spatial phase profile is split at the beam splitter BS1 and the resulting beams go through the two arms of a Mach-Zehnder interferometer. In the upper arm, the spatial structure of the photons is erased when the beam passes through a spatial filter which produces the reference beam $\psi_r(x,y)$. The unknown and reference beams are combined at the beam splitter BS2 and photons are registered with the help of the single photon sensitive camera. The spatial phase profile of the unknown beam is recovered from the recorded interferogram.

The unknown and reference beams are overlapped at a beamsplitter (BS2), and the positions of single photons are detected with a spatially resolving detector (Fig. 2.2(a)). After accumulating numerous photodetections, an interferogram is obtained (Fig. 2.2(b)):

$$\begin{aligned} |\psi(x,y)|^2 &= |\psi_u(x,y) + \psi_r(x,y)|^2 \\ &= |\psi_u(x,y)|^2 + |\psi_r(x,y)|^2 \\ &+ 2|\psi_u(x,y)||\psi_r(x,y)|\cos(\phi(x,y) - \phi_0). \end{aligned} \tag{2.1}$$

Notably, the last term in the equation contains the spatial phase profile $\phi(x,y)$ of the unknown photon. The unknown phase of the single-photon beam is reconstructed using Fourier off-axis holography (described in section 2.4).

2.2 Experimental setup for spatial structure characterization of a single photon beam

Our experimental setup consists of three parts: preparation of heralded single photons with a given spatial structure, reference beam preparation in a modified Mach-Zehnder interferometer, and recording of the first-order interferogram by collecting the positions of the accumulated photons (Fig. 2.3).

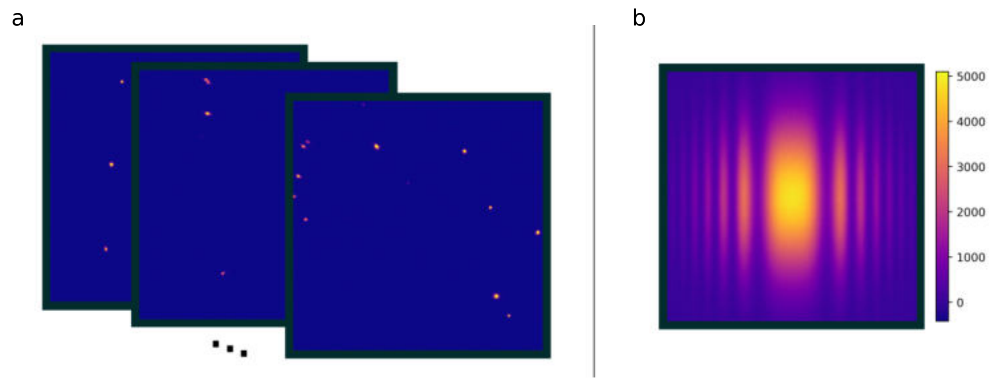

FIGURE 2.2: Photon detection with an intensified sCMOS (IsCMOS) camera and interferogram formation. **(a)** A stack of captured frames with single photon detection events visible as bright spots. **(b)** The interferogram (simulated) is obtained by creating a 2D histogram of the positions of photodetections. The color bar represents the number of detection events.

2.2.1 Heralded single-photon source configuration

The spontaneous parametric down-conversion (SPDC) process is a widely used technique for producing single photons, essential in the field of quantum information science. Within a nonlinear crystal, a high-energy pump photon originating from a laser undergoes conversion into a pair of lower-energy daughter photons, commonly referred to as signal and idler photons.

Owing to conservation laws, such as energy and momentum conservation, the generation of these daughter photons occurs in pairs. As a result, when one photon (the signal photon) is detected, it confirms the existence of its counterpart (the idler photon). While the detection process destroys the signal photon, it simultaneously heralds the presence of the idler photon, thus confirming its availability for use in a variety of quantum information applications.

This heralded single-photon generation method is vital for numerous experimental and practical implementations in quantum communication, quantum computing, and quantum sensing, where accurate control and knowledge of single-photon states are indispensable.

Due to the probabilistic nature of the photon-pair creation via down-conversion, only a small fraction of pump photons results in photon pair generation. As the pumping power of the SPDC source increases, so does the likelihood of generating a photon pair. However, this also increases the probability of producing multiple photon pairs within a brief, time window, which we refer to as simultaneously. Since the desired outcome is the generation of single photon pairs, the multi-pair probability is to be suppressed by operating the crystal at lower pumping powers.

In our experimental setup, as depicted in Fig. 2.3, heralded single photons are prepared via collinear, type-II SPDC process [70]. We pump a PPKTP (Periodically Poled Potassium Titanyl Phosphate) nonlinear crystal with a 405 nm laser beam from a continuous wave diode laser. Signal and idler photons in a generated photon pair have the same central wavelength (810 nm) but exhibit orthogonal polarization. After generation, we separate the two photons using a polarizing beam splitter (PBS). To ensure high spectral filtering, we pass the photons through an interference filter with a 3 nm FWHM. To further refine the photon characteristics, we employ spatial filtering by coupling the photons into a single mode fiber (SMF). Subsequently, an avalanche photo-diode (APD) detects one of the photons, generating a short TTL

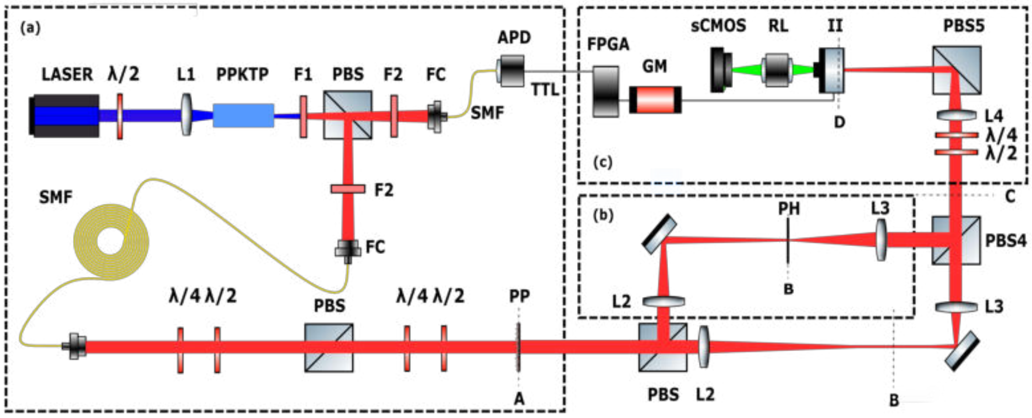

FIGURE 2.3: Experimental setup for a self-referenced measurement of a spatial structure of a single photon beam with an unknown phase profile. The setup comprises three panels: one for preparing heralded single photons with spatial structure, a second for creating a reference beam, and a third for recording the first-order interferogram by collecting the positions of accumulated photons. **(a)** Preparation of an unknown single photon beam $\psi_u(x, y)$. Orthogonally polarized collinear signal and idler photons generated in SPDC type-II process in a nonlinear PPKTP crystal, L1 - a lens with the focal length of 300 mm; after passing through the F1-long pass filter get separated by the PBS - polarizing beam splitter, F2 - bandpass filter transmitting 810 nm $\pm$ 5 nm, FC - optical fiber coupler; Photons are transmitted through the SMF - single-mode fiber, $\frac{\lambda}{2}$ - half-wave plate, $\frac{\lambda}{4}$-quarter wave plate, PP (plane A) - phase imprinting plane, APD - Avalanche photo-diode. **(b)** Preparation of the reference beam $\psi_r(x, y)$. L2, L3 - lenses with focal lengths of 150 mm, and 250 mm respectively; PH - pinhole of size 200 μm, plane B - the intermediate plane of the 4f system; plane C - image plane of the 4f system. L4 - a lens with a focal length of 125 mm. **(c)** Measurement. The intensified sCMOS camera system consists of an II - image intensifier, RL - Relay lens, and an sCMOS camera (Andor Zyla 4.2). Plane D - Image plane of the camera, FPGA - field-programmable gate array, GM - gating module.

pulse. This pulse serves as the trigger for our custom-built intensified sCMOS (IsCMOS) camera [71] via a gating module (Photek GM300-3N). The gating module works at a mean trigger rate (the mean rate at which the trigger signal is generated by the APD) of 200 kHz and is responsible for heralding the arrival of the other photon from the pair, which we use as our heralded signal.

To ensure precise synchronization between the image intensifier's gating time and the signal photon's arrival time, we transmit the signal photon through a 20 m long spool of single-mode fiber. This compensates for any processing time delays introduced by the APD and IsCMOS. The purpose of this setup is to achieve an accurate temporal correlation between the camera's operation and the arrival of the signal photon for our experimental measurements.

2.2.1.1 Preparing structured single photons

To prepare the single photon beam with an unknown spatial phase profile, we employ phase masks positioned in plane A (as illustrated in Fig. 2.3a). To investigate the influence of various phase masks on the single photon beam, we conduct a series of experiments. Each experiment involves the application of different phase masks to the single photon beam, allowing us to analyze their respective effects on the beam's spatial phase profile.

For imprinting a 2D quadratic phase onto the beam, we incorporate a spherical lens with a focal length of 125 mm in plane A. Similarly, to imprint a 1D quadratic phase profile, we position a cylindrical lens with a focal length of 75 mm at a distance of 17 mm before plane A. This extra propagation leads to an equivalent phase profile in plane A, simulating the effect of a cylindrical lens with a focal length of 58 mm.

To imprint a spiral phase mask onto the beam, we place a spiral phase plate in plane A. The spiral phase plate is a specific refractive optical element designed to impart a helical phase structure to an incident light wavefront, converting it into a beam with orbital angular momentum (OAM). When a light wave passes through a spiral phase plate, the phase of the wave changes azimuthally around the center of the plate, forming a twisted wavefront.

2.2.2 Modified Mach-Zehnder interferometer – preparation of the reference beam

In the modified Mach-Zehnder interferometer setup, the single photon beam with its spatial phase enters the interferometer. Each arm of the interferometer comprises 4f imaging systems, utilizing lenses L2 and L3 of focal lengths 150 mm and 250 mm respectively (with a magnification factor of 1.6). The object and image planes of these 4f systems are denoted as planes A and C, respectively. In one interferometric arm, lenses L2 and L3 are accompanied by a pinhole placed in plane B, which serves as a spatial filter removing high spatial frequencies. As a result after passing through the pinhole the beam can be described approximately as a Gaussian beam, acting as the reference beam [72].

However, for certain phases, such as the spiral phase, the beam to be characterized may only contain higher spatial frequencies. In such cases, the pinhole would block all light in the filter arm. To address this, the pinhole needs to be transversely shifted to optimize the transmission through the arm with the spatial filter. This shift introduces an additional linear phase to the reference beam, which does not affect the reconstructed phase.

The reference and signal beams have orthogonal polarizations. To observe interference between these beams, first, they are spatially overlapped at PBS4 – ensuring that both beams travel the same path in space. For two orthogonally polarized beams to interfere, they need to be in the same polarization state. Then their polarizations are rotated using waveplates. By introducing the half-wave plate and orienting its optical axis at 22.5° relative to the initial polarization direction of one of the beams, both beams' polarizations are rotated by 45°. For the vertically polarized beam, this rotation shifts its polarization to 45° relative to the vertical axis, and for the horizontally polarized beam, it similarly shifts its polarization to 45° relative to the horizontal axis. Consequently, both beams end up having diagonal polarizations but in the same direction. The subsequent polarizing beam splitter (PBS5) can then project them onto a common linear polarization direction allowing them to interfere (see Fig. 2.3 b, c). Additionally, plane C is imaged onto plane D, which corresponds to the photo-cathode of the image intensifier. This is done by the lens L4 of focal length 125 mm.

2.2.3 Photon detection – observing self-referenced hologram

In our experimental setup for photon detection and the observation of the self-referenced hologram, each photon that illuminates the image intensifier has the potential to eject a photoelectron, leading to a macroscopic charge avalanche and generating a bright flash on the phosphor screen located at the back of the image intensifier. To capture these flashes, we employ a relay lens comprising two photographic objectives (Fig. 2.3c) to direct the bright flashes onto the sCMOS sensor.

We use the intensified camera in the photon counting mode in which we fit a Gaussian function to the image of each flash detected by the sCMOS camera and store its central position and amplitude [29]. This technique effectively eliminates readout noise from the sCMOS sensor, as well as allows for achieving sub-pixel spatial resolution of photon detection. This will be explained thoroughly in the next chapter which is dedicated to our camera (Chapter 3).

During our experiment, the sCMOS sensor is set to acquire data at a rate of 9Hz, with a specified region of interest of 1000 px $\times$ 1000 px. The image intensifier remains open for about 20 ns after each trigger. To handle situations where two trigger signals occur in a close proximity (less than 3 μs apart), we implement an FPGA to discriminate the second signal – that is the FPGA discards the second signal whenever there are two triggers arriving very close to each other since two signals coming closer than 3 μs make the gating module operation uncontrollable. This ensures optimal operation of the gating module, maximizing the photon count rate and confirming that the photons detected by the camera are genuinely heralded.

We observe approximately on average 25 dark counts per one-second camera frame. Accidental coincidence counts represent another source of noise, occurring when photons that are not heralded, reach the image intensifier during the gate opening time. The accidental coincidence rate can reach up to 3 Hz. To enhance the signal-to-noise ratio (SNR), one could use an image intensifier that allows for shorter gate lengths (ideally the gate opening time should go down to the jitter of the detector of the order of 1 ns), effectively reducing dark counts and accidental coincident counts without compromising the signal level. Due to technical limitations of the gating module and FPGA electronics, we had to use longer gating time which in our case was 20 ns.

2.3 Experimental results

For our experimental setup, we used the following phase masks to produce beams with unknown spatial phase profiles: a spherical lens, a spiral phase plate, and a cylindrical lens as it was mentioned earlier. Separate measurements were carried out for each phase mask to quantitatively reconstruct the spatial phase profiles of the beams. This was accomplished through the evaluation of interferograms obtained from detecting $1 \times 10^7 - 2.5 \times 10^7$ heralded single photons on an intensified sCMOS camera [29], where an average of 200 to 600 photons were detected every second.

The resulting interferograms for the 2D quadratic and spiral phases are depicted in the first row of Fig. 2.4 (Fig. 2.4a and Fig. 2.4d) while their respective 2D reconstructed phases are displayed in the second row of Fig. 2.4 (Fig. 2.4b and Fig. 2.4e). The specific approach used for phase reconstruction can be found in the section 2.4. The statistical uncertainties of the reconstructed phase and intensity were calculated using a simulation: The phase retrieval process was repeated 1000 times, each time with the number of photons at each pixel drawn from a Poisson distribution based on the average photon count at that pixel. We could then calculate the mean and the uncertainty of the phase at each pixel from these 1000 trials. The statistical uncertainties for the single pixel of the reconstructed 2D phases are below $\frac{2\pi}{30}$ and $\frac{2\pi}{50}$ for the 2D quadratic phase and spiral phase in a radius of 50 pixels with maximum visibility and photon count rate respectively. The averaged values of the reconstructed

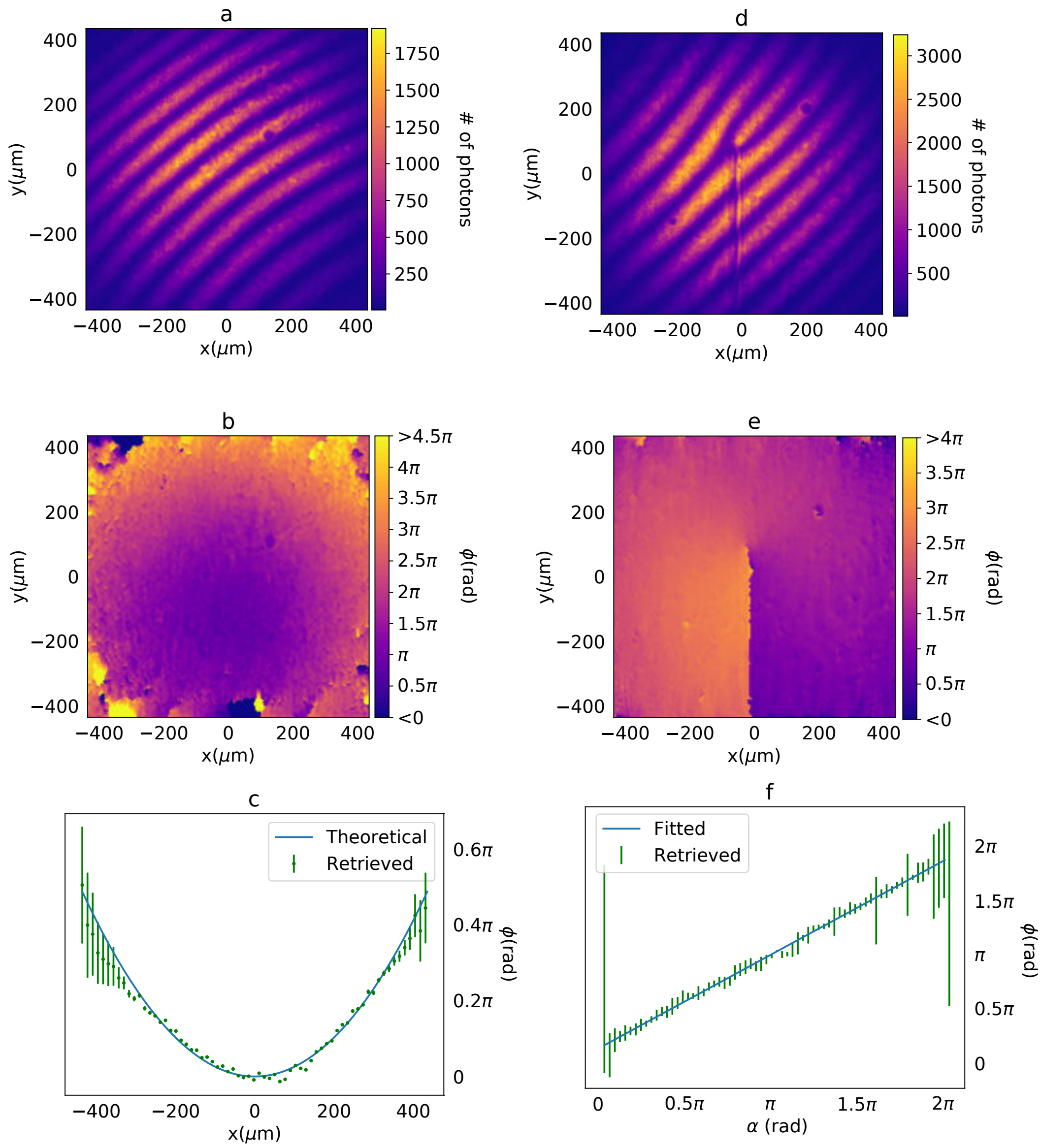

FIGURE 2.4: **(a)** the recorded interferogram for 2D quadratic phase; **(b)** the reconstructed phase for 2D quadratic phase; **(c)** plots of the theoretical quadratic phase (blue solid line) and the reconstructed phase (dots) averaged over middle 50 columns of the plot in **b** with standard deviation in case of spherical phase mask applied. In the middle part, standard deviation is smaller than $\frac{2\pi}{150}$; **(d)** the recorded interferogram for spiral phase mask; **(e)** the reconstructed phase for spiral phase mask; **(f)** plots of the reconstructed phase in case of spiral phase mask with standard deviations versus the azimuthal angle α and a fitted linear function.

2D quadratic phase taken from the central 50 columns of Fig. 2.4b are shown in Fig. 2.4c, with statistical uncertainties obtained from the simulation. The corresponding theoretical plot is also provided (Fig. 2.4c - blue line). The middle part shows a standard deviation smaller than $\frac{2\pi}{150}$. The result is largely consistent with theoretical expectations, despite the limitations imposed by systematic errors. As predicted, the reconstructed phase for the spiral phase plate is linearly dependent on the azimuthal angle (Fig. 2.4f).

Fig. 2.5a and Fig. 2.5b display the recorded interferogram and the corresponding

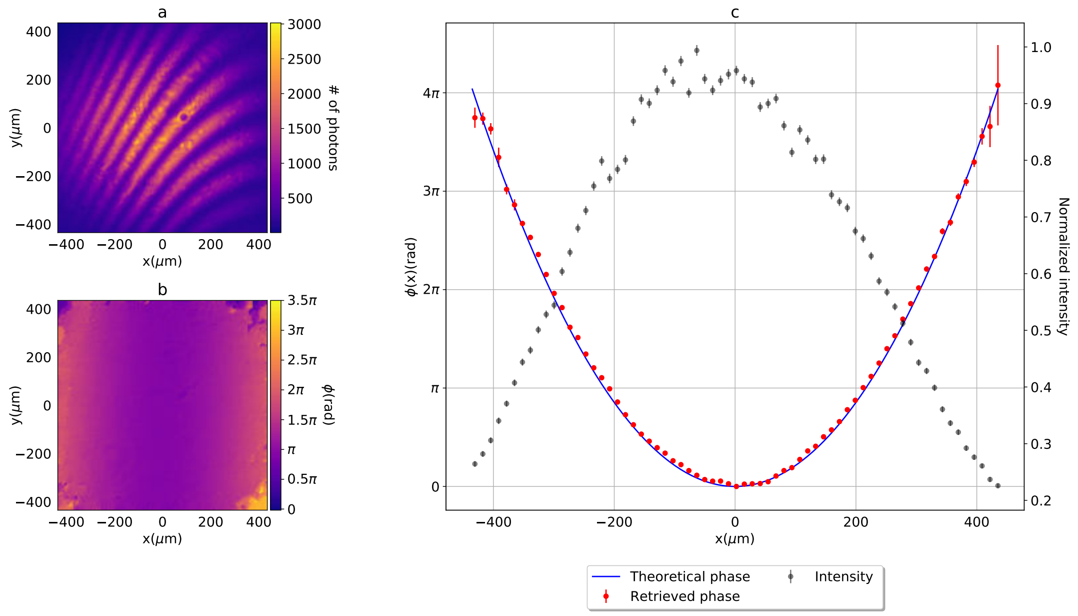

FIGURE 2.5: **(a)** Measured interferogram with 1D quadratic phase, **(b)** Retrieved phase, **(c)** Retrieved phase and amplitude with error-bars. The error-bars are scaled to 3 times their actual value for the retrieved phase and 5 times for intensity. There is a theoretical plot for comparison with the retrieved phase based on $\phi(x) = \frac{\pi x^2}{\lambda f}$; where λ is the wavelength of the photon and f is the focal length of the cylindrical lens used as a 1D quadratic phase object. In all the plots, x and y denote the positions at the plane A (Fig. 2.3).

reconstructed phase when a 1D quadratic phase mask is utilized. The single pixel uncertainty of the reconstructed 2D phase in Fig. 2.5b is below $\frac{2\pi}{50}$ in a region with a radius of 50 pixels. Fig. 2.5c illustrates the plots of the reconstructed phase and intensity profile of the single photon beam, with each point representing an average of 50 pixels from the center of Fig. 2.5b. The theoretical phase (Fig. 2.5c – blue line) for the 1D quadratic phase is also plotted, using the expression $\phi(x) = \frac{\pi x^2}{\lambda f}$, where λ is the photon's wavelength and f is the focal length of the cylindrical lens used as the 1D quadratic phase object. The plot in Fig. 2.5c displays a good match between the experimental and theoretical phases. An additional linear phase was required between the reference and unknown beam in the interferometer for the data analysis. The interference visibilities for the 2D quadratic, spiral, and 1D quadratic phases were found to be approximately 69%, 78%, and 77% respectively.

2.4 Fourier Off-Axis Holography – spatial structure reconstruction for single photons

To reconstruct the spatial structure of the single photon beam, we use Fourier off-axis holography [73]. We add the extra linear phase for the sake of our data analysis process.

The experimental design we employed involves introducing a linear phase in the interferometer by manipulating the orientation of the beams, causing an overlap only at the 4f image plane and the ultimate image plane (designated as planes C and D in Fig. 2.3). This tilt in the beams, hence adding a linear phase to the interferogram, helps the data analysis. We obtain a reference measurement of this linear phase, which is subtracted during the final phase reconstruction, making the interpretation of the measured interferograms simpler.

Let's start with the first-order interferogram, which is gathered by capturing the positions of the collected photons, as presented in Eq. (2.2):

$$
\begin{aligned}
|\psi(x,y)|^2 &= |\psi_u(x,y) + \psi_r(x,y)|^2 \\
&= |\psi_u(x,y)|^2 + |\psi_r(x,y)|^2 \\
&+ 2|\psi_u(x,y)||\psi_r(x,y)|\cos\big(\phi'(x,y) - \phi_0\big),
\end{aligned}
\tag{2.2}
$$

where, ϕ_0 represents the interferometric phase offset, and the spatial phase $\phi'(x,y)$ between the interfering beams can be written as:

$$
\phi'(x,y) = (a_1 x + a_2 y) + \phi(x,y). \tag{2.3}
$$

In this equation, $(a_1 x + a_2 y)$ signifies the linear phase introduced in the interferometer, and $\phi(x,y)$ symbolizes an arbitrary phase that we intend to reconstruct.

The first step in the analysis involves performing a 2D Fourier transform on the gathered data. Corresponding to the Fourier transform properties, adding a linear phase leads to separating the phase-dependent component of the signal with respect to the phase-independent component in the Fourier plane's center.

The Fourier transform of Eq. (2.2) results in:

$$
\begin{aligned}
\mathscr{F}[|\psi(x,y)|^2] &= \mathscr{F}[|\psi_u(x,y)|^2 + |\psi_r(x,y)|^2] \\
&+ \mathscr{F}[p(x,y)](k_x + a_1, k_y + a_2) \\
&+ \mathscr{F}[p^*(x,y)](k_x - a_1, k_y - a_2),
\end{aligned}
\tag{2.4}
$$

Here, $p(x,y) = |\psi_u(x,y)| \times |\psi_r(x,y)| \times \exp\{(-i(\phi(x,y) - \phi_0))\}$, with the first term on the right-hand side containing only phase-independent parts.

It is necessary to ensure that the linear phase magnitude is high enough to facilitate the separation of the three parts of Eq. (2.4) in the Fourier domain. Through filtering in the Fourier domain, it is possible to retain only one of the three terms from Eq. (2.4), while preserving all information regarding the phase. As a result of this analysis, we obtain $\mathscr{F}[p(x,y)]$ and its inverse Fourier transform yields $|\psi_u(x,y)| \times |\psi_r(x,y)| \times \exp\big(i(\phi'(x,y) - \phi_0)\big)$.

It is then feasible to retrieve the phase $\phi'(x,y)$ by extracting the argument of the complex number from each pixel. The final result is calculated from the wrapped phase using a 2D phase-unwrapping algorithm [74], keeping in mind the need to remove the additional linear phase. The 2D phase-unwrapping algorithm systematically scans through the wrapped phase map, pixel by pixel, resolving the discontinuities by adding or subtracting multiples of 2π. This reconstructs a continuous phase map.

The linear phase removal is accomplished by repeating the entire procedure for the reference measurement, which doesn't involve a phase mask, thereby retrieving the linear phase, $(a_1 x + a_2 y)$. By subtracting this reference linear phase and disregarding the constant phase offset ϕ_0, we finally attain the sought-after imprinted phase $\phi(x,y)$ (Fig. 2.6).

For achieving optimal reconstruction results, it is critical to ensure high visibility interference fringes, which necessitate intensity profiles of both the reference and unknown beams to be matched. This precondition, common to most interferometric techniques, is met in our experiment by using the waveplates before the Mach

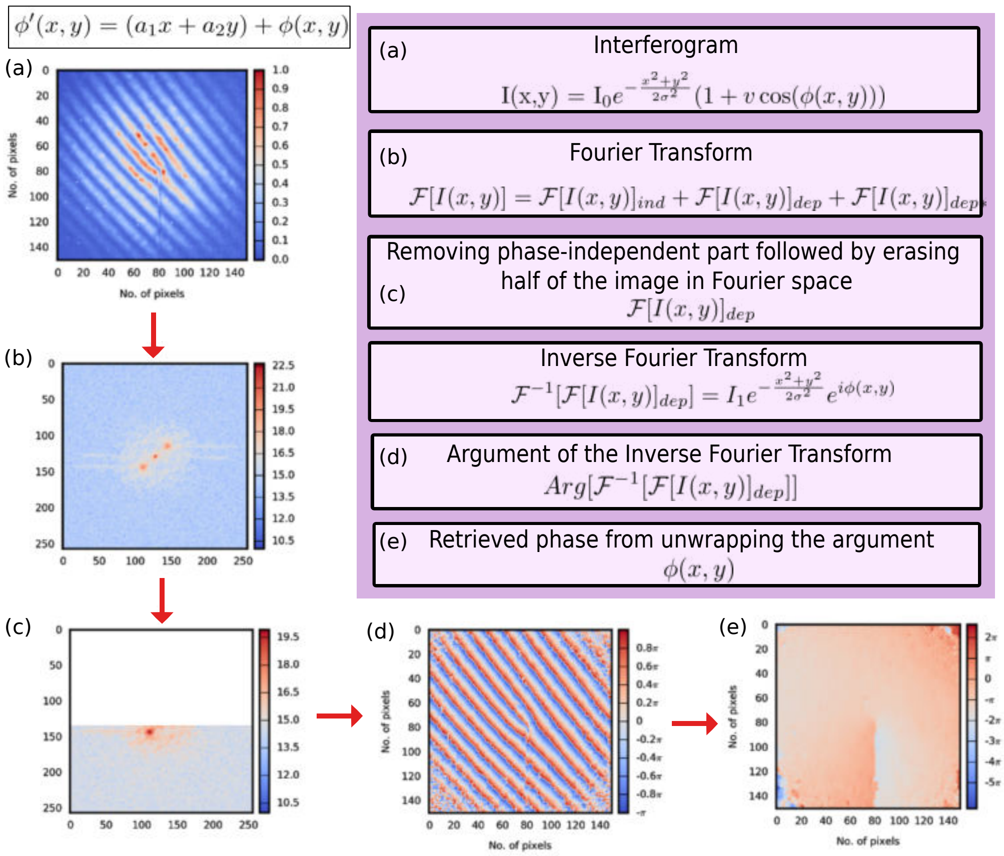

FIGURE 2.6: Fourier off-axis holography. Fourier off-axis holography involves executing a 2D Fourier transform on the gathered interferogram. The interferogram in shown in **(a)** and the 2D Fourier transform is shown in **(b)**. Initially, a linear phase is added to separate components in the Fourier domain. By filtering only one phase independent term is retained, ensuring phase information retention (**(c)**). After obtaining the inverse Fourier transform, the imprinted phase is extracted pixel-wise from the argument of the resultant complex number (shown in **(d)**). Reference measurements without a phase mask help remove any added linear phase. This phase is then unwrapped using a 2D phase-unwrapping algorithm (retrieved unwrapped phase shown in **(e)**). The summary of the phase retrieval algorithm is described on the top-right corner of the figure.

Zehnder interferometer and the polarizing beam splitter together (Fig. 2.3). This is verified by independently checking the intensity profiles of both beams with a single-photon sensitive camera. Separate measurements of both beams' intensity profiles permit the adjustment of the splitting ratios of both beamsplitters (BS1 and BS2 in Fig. 2.1), an essential step to counteract the variable loss induced by the spatial filter, contingent on the object's phase.

2.5 Conclusion

In conclusion, we have developed a self-referenced interferometric method that can successfully reconstruct both the spatial phase and the amplitude profile of an unidentified single photon beam. The unique aspect of our technique is its independence from a reference photon, making our system resilient and relatively easy to employ [5].

Contrary to techniques that hinge on the assessment of a two-photon probability distribution, such as the method presented in [61], our approach eliminates the need for coincidence detection. As a result, the self-referenced holography technique is considerably less complex from a technical standpoint and more tolerant of losses. Unlike the method described in [61], our method is currently sensitive to interferometric phase fluctuations. However, this challenge could be resolved by employing common path designs [72]. If the loss induced by the spatial filter cannot be accommodated, then shearing interferometry [75] can be utilized as an alternative to spatially filtered references.

Our method proves to be versatile, not limited to one-dimensional phase reconstruction, and capable of characterizing any single photon beam with an unknown pure spatial state, including those with orbital angular momentum modes [76]. Given its simplicity, this measurement scheme has the potential to be widely applicable in quantum communication and imaging sectors. Techniques analogous to ours could be employed to characterize the spectral degrees of freedom of photons [77]. Furthermore, similar methods could potentially be valuable in matter-wave interferometry [78, 79]. An important direction for future research would be to explore if our method could be extended to mixed [80] or entangled states.

J.S. conceived the idea. W.S. and S.K. built the experimental setup, performed the experiments, and analyzed the results. R.L. supervised the project. J.S. and R.L. designed the experiment.

Chapter 3

High dimensional quantum correlation measurements with an adaptively gated hybrid single photon camera

High-dimensional quantum correlations have emerged as a crucial resource for quantum technologies, necessitating efficient measurement techniques [81, 82, 83]. Spatial correlations, with their inherent high dimensionality and ease of manipulation via basic optical components, are particularly interesting in the fields of quantum imaging [84, 55], metrology [85], and the testing of fundamental principles of quantum mechanics [86]. However, characterizing spatially correlated photon pairs requires detectors that are highly sensitive and capable of resolving individual photons both in time and position which poses a significant challenge. These measurements demand high acquisition rates for statistically significant data, as well as good temporal resolution for observing coincidences. In recent years, various types of single photons cameras have emerged which include electron-multiplying charge-coupled devices (EMCCD) [41, 87, 24, 23, 88], intensified scientific complementary metal oxide semiconductor (IsCMOS) [29, 30, 31] or intensified CCD cameras [25, 26], single-photon avalanche diode (SPAD) arrays [89, 38, 39, 90], and intensified high-speed Timepix cameras [91, 92, 33, 93]. However, there exists a trade-off between temporal and spatial resolution, as faster cameras tend to have lower spatial resolution and vice versa. While intensified cameras offer high pixel numbers and sub-nanosecond gating times they are hindered by low-duty cycles, necessitating long measurement times for adequate statistics [94, 29]. Conversely, time-tagging single-photon avalanche diode (SPAD) arrays provide continuous readout and high temporal resolution, yet their pixel counts are orders of magnitude lower than those of cameras.

Addressing the aforementioned limitations, this chapter outlines an overview of a hybrid single photon-sensitive camera with an adaptively gated image intensifier that combines a high spatial resolution sCMOS sensor and a high temporal resolution detector – a photo-multiplier tube (PMT). Our goal is to detect and register individual photons, which is achieved by incorporating an image intensifier. The intensifier can transform a single photon into a burst of photons, maintaining its temporal and spatial information. With our hybrid camera setup, we can precisely control the number of photons registered by utilizing feedback from a high-temporal-resolution detector.

Here we describe how the hybrid camera is constructed and its working principle followed by using this hybrid camera to measure spatial correlations of photon pairs generated in the type-I SPDC process. We also study the data acquisition rate of this camera in comparison to an IsCMOS camera [6, 95].

A manuscript about the research work of this chapter has been submitted [6].

3.1 Photon detection scheme with a standard intensified camera

Intensified cameras are usually assembled in three parts: image intensifier, relay lenses for imaging, and CCD/CMOS sensor. Let's begin with how an image intensifier works.

3.1.1 Image intensifier

Fig. 3.1 depicts the parts of the image intensifier. The image intensifier is composed of a photocathode, a micro-channel plate (MCP), and a phosphor screen located at the back of the intensifier. When a photon strikes the image intensifier, it initiates

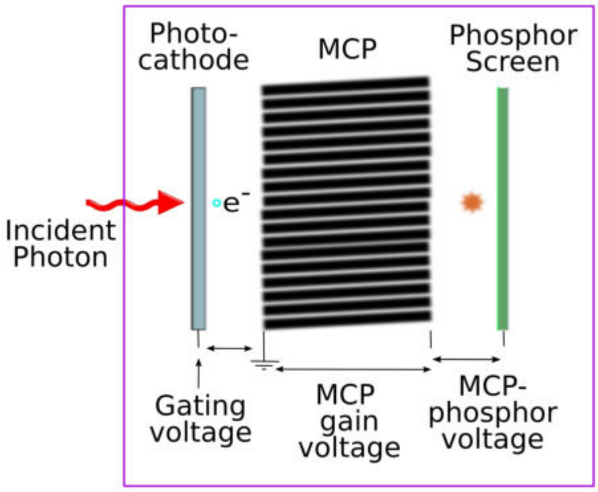

FIGURE 3.1: Schematic of the image intensifier. The image intensifier consists of a photocathode, a microchannel plate (MCP), and a phosphor screen located at the back of it. When a photon is registered by the image intensifier, it is turned into a photoelectron by the photocathode. The gating voltage is there to gate the image intensifier. When the photoelectron enters the MCP, it creates a macroscopic charge avalanche due to reflection from the channel walls. MCP gain voltage controls the amplification process in the MCP and MCP-phosphor voltage accelerates the electron cloud further. In the end, the electron cloud turns into a burst of photons on the phosphor screen. The image intensifier used in this experiment is Hamamatsu V7090D-71-G272.

the emission of a photoelectron from the photocathode with a probability described by the quantum efficiency (QE) coefficient. For photons of the wavelength of 800 nm where we operated, it has the quantum efficiency, QE = 20%.

This photoelectron's path depends on the voltage between the photocathode and the MCP. Positive voltage sends it towards the MCP, where it enters one of nearly 9 million channels. It gets accelerated by the constant voltage across the plate and reflects from the channel walls to create a macroscopic charge avalanche. Such a cloud of electrons is driven by the voltage between the MCP and the phosphor. When it impinges the phosphor screen (P47 type), it triggers the excitation of the phosphor molecules. This excitation causes them to radiate light. The light intensity reduces gradually, as described by the function, $I(t) = Ae^{-\lambda t}$, λ representing the decay constant. This results in a bright flash at the output phosphor screen. The brightness of the light can be adjusted by changing the MCP's voltage (MCP gain voltage in Fig. 3.1), with higher voltage producing brighter light.

3.1.2 Relay lenses

The bright flashes from the phosphor screen are imaged onto an sCMOS sensor by a relay lens composed of two photographic objectives: the image intensifier lens and the camera lens.

The image intensifier lens is crucial in collecting light from the image intensifier. It is positioned so that the phosphor screen lies on its focal plane. The lens has two key parameters: its focal length and F#. F# denotes the lens's f-number or aperture setting. A lower F# corresponds to a wider aperture, capturing more light from the phosphor screen. Given the image intensifier's active area (10 x 13.5 mm), focusing across the entire area is challenging. Thus, we focus on a specific section of the active area to reduce distortion. However, a smaller F# may result in increased distortion due to its limited depth of focus. Our camera setup uses the Canon 50mm f/1.0 L DSLR lens, which offers good optical properties even at F# = 1.0, capturing 20% of central light. The lens is attached to the image intensifier with a custom 3D-printed bracket ensuring proper alignment.

The selected camera lens is a manual Canon lens with an F# of 0.95 and a focal length of 50mm (Canon 50mm f/0.95 Dream Lens). This lens is configured to produce a sharp image of distant objects on the camera sensor. By ensuring that objects at infinity are focused crisply on the sensor, we simplify the alignment of the other components in the setup. When an infinite object's image is accurately formed on the camera chip, it indicates that the lens is at its focal distance from the chip. This straightforward correlation is why we opted for a manual lens in this context.

3.1.3 sCMOS camera

The camera used here is a high-resolution sCMOS sensor that captures and digitizes the positions of photons as they interact with the Image Intensifier (II). It registers light emitted from the phosphor screen of the II. Given that both the camera lens and the II lens possess a 50mm focal length, the system achieves a 1:1 magnification. The active area of the camera should therefore be at least as big as the active area of the II.

From an electronic perspective, the camera requires a connection to a computer, which, in this setup, is achieved using a dual Camera-Link cable. It's essential for the camera to signal the commencement and termination of the exposure for its first row and to indicate when the entire sensor is detecting light. Our objective is to have the II operational when the camera's entire sensor is engaged in light detection. To accomplish this synchronization, we utilized a custom FPGA in conjunction with a LabVIEW program. In this arrangement, the sCMOS camera functioned as the primary signal generator, with the II operating as a responsive device, triggered only during full-sensor light capture by the camera.

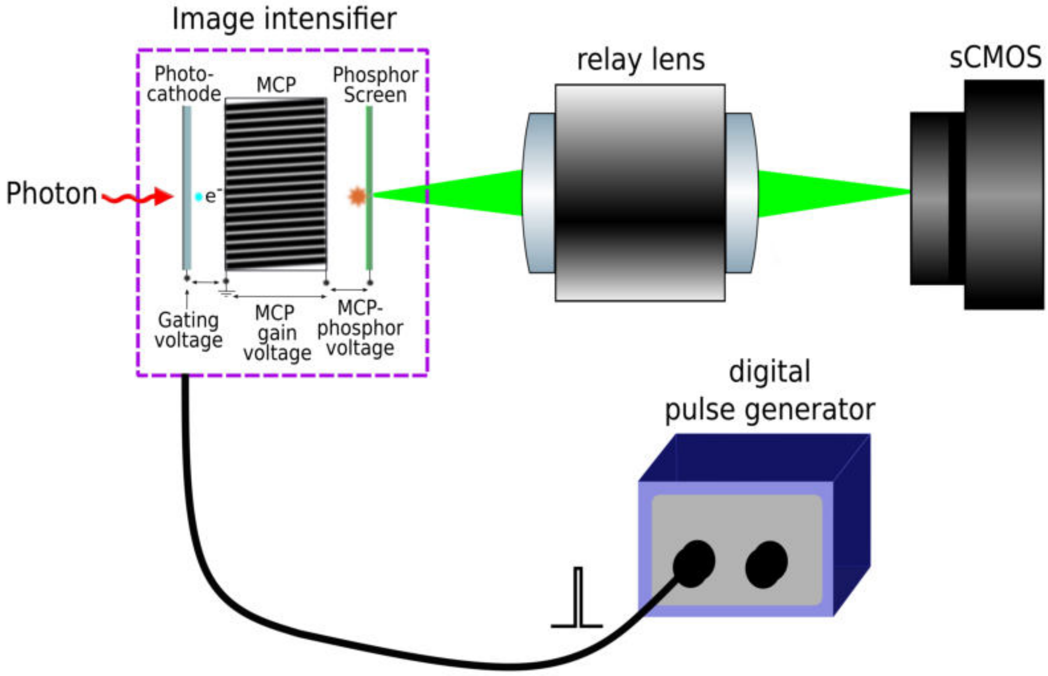

FIGURE 3.2: Intensified camera for coincidence imaging. The phosphor screen of the image intensifier is imaged onto the sCMOS camera by a relay lens composed of two photographic objectives. The image intensifier gate time is adjusted and simply synchronized with the sCMOS acquisition. The gate-triggering pulses of 150 *ns* duration are sent by a digital pulse generator Stanford DG-645.

3.1.4 Scheme for coincidence imaging with the standard intensified (IsCMOS) camera

Standard intensified cameras provide high spatial resolution, but their frame rate is slow. Due to the use of CMOS sensors, the time interval between consecutive frames is generally about six orders of magnitude longer than the minimum gating time of an IsCMOS camera. IsCMOS cameras can typically achieve frame rates between 50 *Hz* and 200 *Hz* at the full spatial resolution, with gate lengths in the nanosecond range. For instance, an IsCMOS camera Andor iStar can obtain a frame rate of 50 *Hz* at a full spatial resolution with a gate length of 2 *ns*.

To analyze the spatial correlations of photons generated simultaneously with such a detection system, it is crucial to gate the camera once per frame, which allows us to access the temporal relationship between detected events. In this scenario, we only register photons within the intensifier gating time which establishes the coincidence window for photon detections, and it is necessary to maintain the average photon flux per entire frame significantly lower than one photon per coincidence window to minimize accidental coincidence detections.

For coincidence imaging, we gate the image intensifier externally by sending nanosecond time-scale pulses from a digital pulse generator manufactured by Stanford Research Systems, model DG-645 (Fig. 3.2) [29, 94].

3.2 Hybrid intensified camera (HIC)

The hybrid intensified camera we present, as depicted in Fig. 3.3a, employs readily available off-the-shelf components and integrates an image intensifier akin to those used in typical intensified cameras. However, in addition to that, our design incorporates one high spatial resolution sCMOS camera and a fast photo-multiplier tube (PMT).

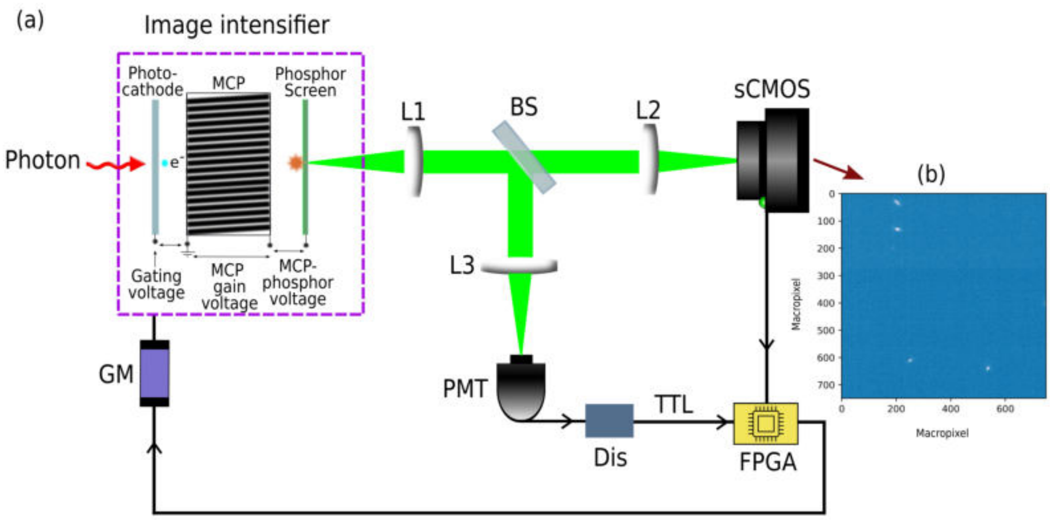

FIGURE 3.3: **(a)** Schematic of the hybrid camera setup. The output light of the image intensifier gets separated into two paths by a beam splitter: one part illuminates the fast detector (PMT) and another part is imaged onto the high spatial resolution detector (sCMOS camera). Based on the information from the fast detector (PMT), FPGA can control the gating time of the image intensifier, therefore controlling the number of registered photons. Image intensifier (Hamamatsu V7090D-71-G272); BS – beam-splitter; L1, L2, L3 – lenses; PMT – photomultiplier tube (Hamamatsu R1924A); Dis – Discriminator; sCMOS (Andor Zyla 4.2 sCMOS camera); FPGA – field-programmable gate array (NI myRIO-1900); GM – gating module (Photek GM-300-3N). **(b)** One captured sCMOS frame with single photon detection events visible as bright spots.

In the hybrid camera design, we place a flat glass plate to split the light from the image intensifier output into two detectors (shown in Fig. 3.3a). Since the photomultiplier tube is a single-pixel detector and effectively requires a much lower intensity of light, the majority of light should be diverted to the camera. Also, to ensure optimal imaging quality, the camera is placed on the go-through path, while the PMT is placed on the reflected path since the PMT does not require perfect imaging. Using the uncoated, thin glass plate at a 45-degree angle, about 10% of the light is directed towards the PMT that delivers high temporal resolution, whereas the remaining 90% is captured by an sCMOS camera that provides high spatial resolution.

The image intensifier lens produces a collimated beam with a 72 mm aperture, as detailed in section 3.1.2. A Canon EF 1.8 F#, 50mm lens is used in the PMT path. With its 50mm focal length, the system has a 1:1 magnification, allowing efficient light collection on the PMT with a 22 *mm* diameter photocathode, comparable to the image intensifier's active area. Additionally, since this lens came with a translation stage, for convenience, this lens can be adjusted via software and positioned perpendicular to the beam's optical path from the beam splitter (BS).

We image the phosphor screen of the image intensifier onto the sCMOS camera with the set of lenses L1 and L2 as described in the section 3.1.2. Each bright flash on the sCMOS camera (Fig.3.3b) signifies one corresponding photon incident on the image intensifier. We eliminate the readout noise and achieve sub-pixel spatial resolution by fitting each detected flash with a Gaussian function and recording its central position and amplitude [94, 29].

Our hybrid camera offers exceptional spatial resolution, surpassing the component sCMOS camera and limited only by the number of channels in the MCP of the image intensifier, providing almost 9 megapixels of spatial resolution. Using the fast detector PMT, we employ a feedback loop that enables us to adaptively regulate the exposure (opening) time of the image intensifier and record a pre-selected number of photons on each frame.

3.2.1 Working principle of the adaptive gating method

The hybrid camera is designed to capture photon events in real time. As illustrated in Fig. 3.4a, the image intensifier (II) is opened simultaneously with the start of signal recording on both the sCMOS and PMT. The fast detector, PMT, provides nearly instantaneous readout, enabling the setup to count the number of detected photons on the image intensifier much faster than the sCMOS camera's framerate. As the image intensifier can be gated with nanosecond resolution, feedback from the PMT could in principle disable the image intensifier after detecting the desired number of photons within nanoseconds. This allows us to capture a consistent number of photons in each frame. However, the gating and signal analysis introduce a delay at the nanosecond scale, resulting in a delay of roughly 100 ns for deactivating the image intensifier after reaching the condition of detecting the set number of photons. The delay can be reduced to a few tens of nanoseconds with custom electronics.

To register only events originating from the image intensifier, we employ a fast analog discriminator to reject noise and digitize the PMT signal, flagging each detected photon with a pulse on the discriminator output.

For fast, delay-free electronic control of gating the image intensifier, we use a FPGA that records signals from both the discriminator and the camera acquisition (Fig. 3.3a). As the sCMOS camera operates in a rolling shutter mode, where the top row starts acquiring signals first, and each subsequent row starts with a slight delay, we need to monitor the state of all rows to ensure recording all image intensifier photon detection events on the camera. To ensure all photons are registered when the camera is fully open, the FPGA registers a "Fire All" signal, indicating that all rows of the sCMOS camera are recording light.

Once the "Fire All" signal is detected, the FPGA opens the Image Intensifier (II) gate and keeps it open until either the set number of photons is detected or the "Fire All" signal becomes low, indicating that some rows of the camera have stopped the acquisition. Terminating the image intensifier's acquisition after registering a set number of photons prevents the latter photons from being detected, ensuring that a predetermined number of photons are captured in each frame. With our system, the gating time of the image intensifier is dynamically adjusted to match the event detection rate in real-time, resulting in varying intensifier gate opening durations at each frame, but with the same number of photons detected. This demonstrates the possibility of actively controlling the gating time during data acquisition, enabling an in-frame feedback loop.

In Fig. 3.4b, we present both the sCMOS camera frame and an oscilloscope screen displaying a single intensifier gate opening duration, during which 5 events are registered on both the PMT and sCMOS camera. After detecting 5 photons, acquisition by image intensifier ends preventing any subsequent photons from being detected. With this feedback control, in each frame, the gate opening time of the image intensifier is adjusted in such a way that 5 photons are registered. This demonstrate the ability of our system to capture and analyze photon events in real-time.

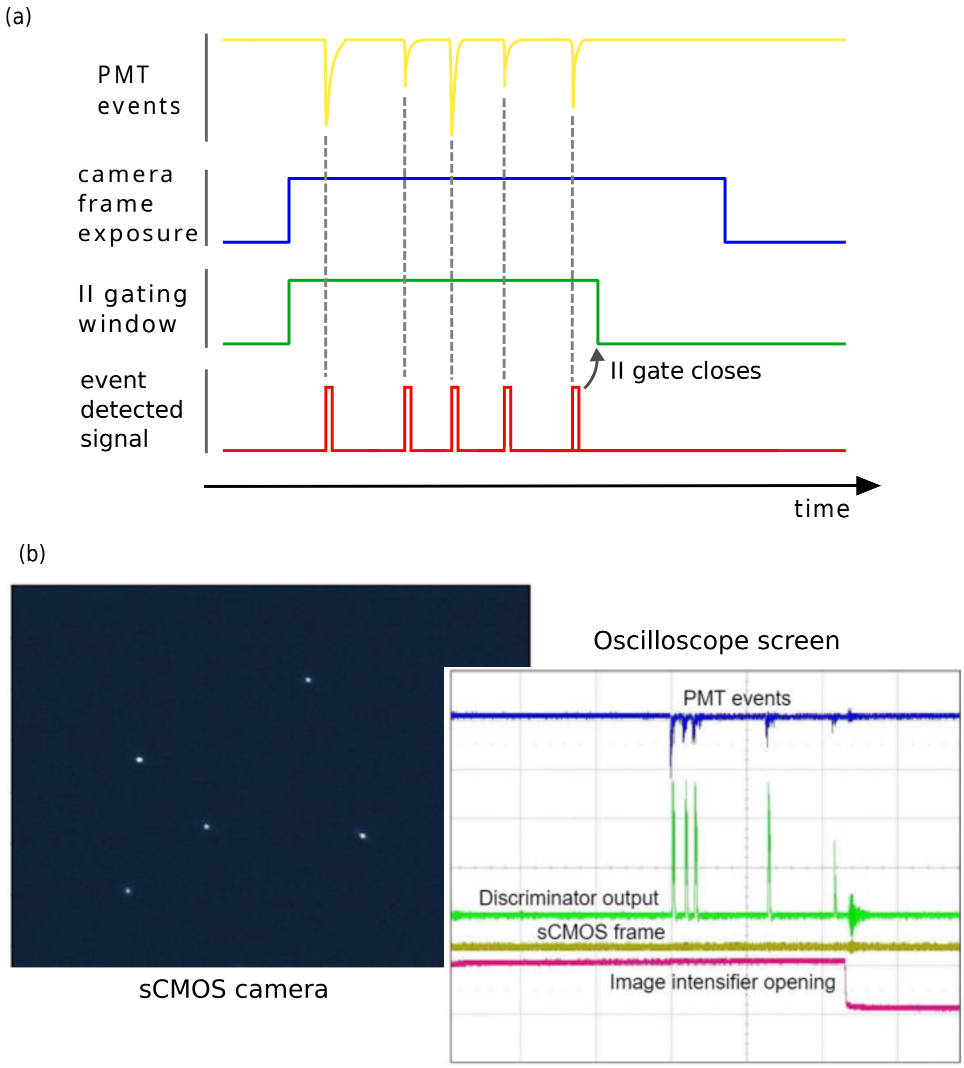

FIGURE 3.4: Hybrid intensified camera – working principle. **(a)** Illustration of the adaptive time gating algorithm with counting events. This is an example of registering 5 pre-selected events: the yellow trace represents the raw signal from the fast detector (PMT). The blue trace represents the sCMOS camera frame exposure while it registers the 5 events. The green trace represents the signal controlling the state of the image intensifier – the high signal corresponds to the image intensifier being opened. The red trace represents the 4 events as counted by the FPGA. The image intensifier closed after registering 5 photons, therefore preventing any further registration of photons. **(b)** Both the sCMOS camera frame and an oscilloscope screen displaying a single intensifier gate opening duration, during which 5 detected events are registered on both the PMT and sCMOS camera.

3.3 Brightness correlation of photon detection events with the two detectors for the time of arrival measurement

The hybrid camera configuration effectively addresses the low-duty cycle limitations commonly observed in standard intensified cameras by integrating a second detector with high temporal resolution. Both the sCMOS camera and the high temporal resolution photomultiplier tube (PMT) record the brightness of the phosphor screen flashes, enabling temporal information to be assigned to the photons captured by

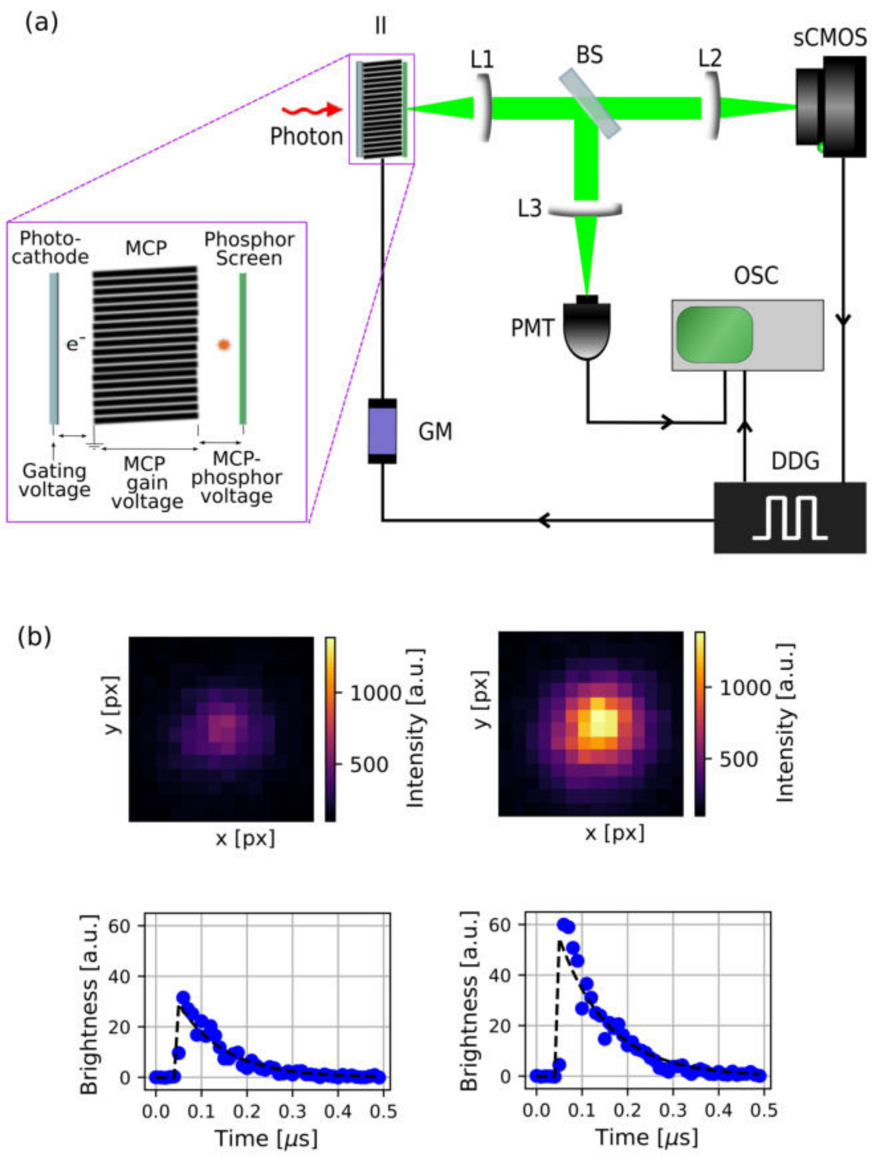

FIGURE 3.5: Hybrid camera configuration designed for precise photon arrival time measurement through photon brightness comparison. **(a)** In this configuration, to control the image intensifier's exposure time, a precise delay generator is activated after the sCMOS camera frame is fully exposed. Simultaneously, the PMT signal is captured using a digital oscilloscope. For a detailed view of the image intensifier's internal structure, refer to the inset. (II – image intensifier; BS – beam-splitter; L1, L2, L3 – lenses; PMT – photomultiplier tube; sCMOS – sCMOS camera; GM – gating module; OSC – oscilloscope; DDG – digital delay generator.) **(b)** The captured signals are presented as examples - the top row displaying zoomed-in sCMOS camera frames, and the bottom row showing corresponding PMT signals. Due to the image intensifier's approximately 20% quantum efficiency in converting photons to bursts, both detectors are capable of measuring photon bursts from each individual photon, enabling the correlation of events.

the camera frame. In this scenario, in our experimental setup (Fig. 3.5a), the light beam from the image intensifier is divided using a beam splitter and simultaneously recorded by the sCMOS camera and the photomultiplier tube (same as before).

When the camera initiates full-frame image acquisition, it sends a "Fire All" signal, indicating that all rows of the sCMOS sensor are capturing data. This signal triggers the digital delay generator (Stanford Research DG645), opening the image intensifier and initiating data recording from the photomultiplier on a digital oscilloscope (Teledyne LeCroy 610Zi) for a precisely determined time.

Consequently, our setup produces frames from the sCMOS camera and corresponding voltage waveforms from the PMT, as depicted in Fig. 3.5b. By fitting appropriate functions to the amplitudes of both signals, we can accurately extract the brightness of individual events, facilitating correlation in both the temporal and spatial domains [96]. This approach enables precise time-tagging of individual photons. Our hybrid camera method serves as a proof-of-concept, demonstrating the potential of achieving nanosecond time-tagging for photon detections in a multi-megapixel spatial resolution sensor.

3.3.1 Time of arrival measurement – time-tagging possibilities of single photons

Correlating the brightness of events recorded by both HIC detectors allows precise determination of the arrival time for each photon captured on the sCMOS camera frame. This capability can be easily combined with adaptive gating, enabling the acquisition of frames with a predetermined number of accurately timestamped photons.

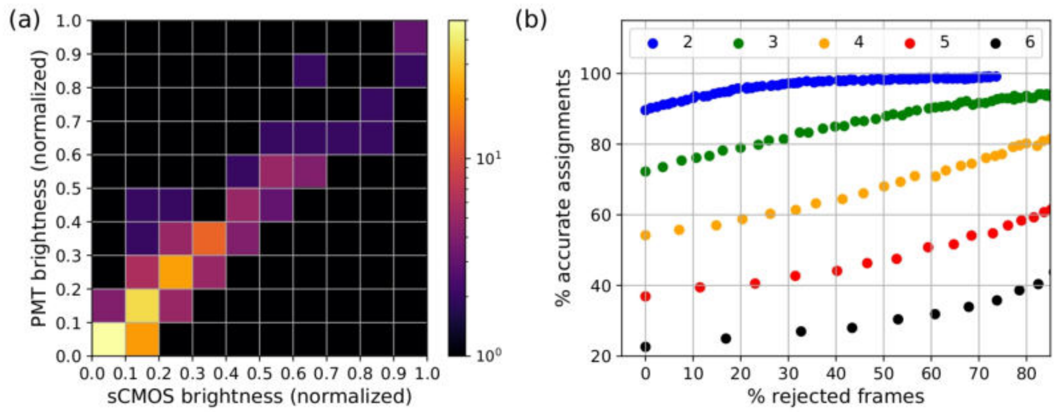

FIGURE 3.6: Brightness correlation for time tagging capabilities of the hybrid camera. (a): sCMOS and PMT brightness correlation map of recorded single photon frames, plotted in logarithmic scale. The color scale represents the number of occurrences, with black indicating at most 1 occurrence. (b): Single photon time tagging accuracy as a function of the percentage of rejected frames for two (blue), three (green), four (orange), five (red), and six (black) photon frames.

To assess the time tagging capabilities and evaluate accuracy in frames with multiple photons, we constructed a synthetic data set using camera frames containing only a single photon. For each of these single photon frames, we recorded two corresponding numbers representing the PMT and sCMOS brightness. Fig. 3.6a illustrates the distribution and linear correlation of these brightness values. Subsequently, we created n-photon frames by randomly drawing n-element tuples without repetition from the set of single photon frames. To maintain high-time tagging accuracy, we rejected pairs or tuples when the phosphor flashes exhibited similar brightness values. Each tuple could thus either possess correct or incorrect time tagging or be neglected due to the proximity in brightness values. The 0% rejected frames shown in Fig. 3.6b indicate no discarding of events based on brightness criteria, resulting in 90% time tagging accuracy for frames containing 2 photons. It is possible to achieve 80% accuracy for 3-photon frames while neglecting 20% of frames, with negligible impact on measurement time. It is worth noting that the majority of events exhibit relatively low brightness. To achieve a more uniform brightness distribution, appropriately sweeping the image intensifier voltage can help reduce the percentage of rejected frames.

3.4 Experimental setup for characterizing momentum correlation of photon-pairs in type-I SPDC with adaptively gated HIC

Here we investigate the far-field distribution of the type-I SPDC light and observe the momentum anti-correlation of the generated bi-photon state with our hybrid camera setup (Fig.3.7a). In type-I SPDC, due to the phase-matching conditions, the

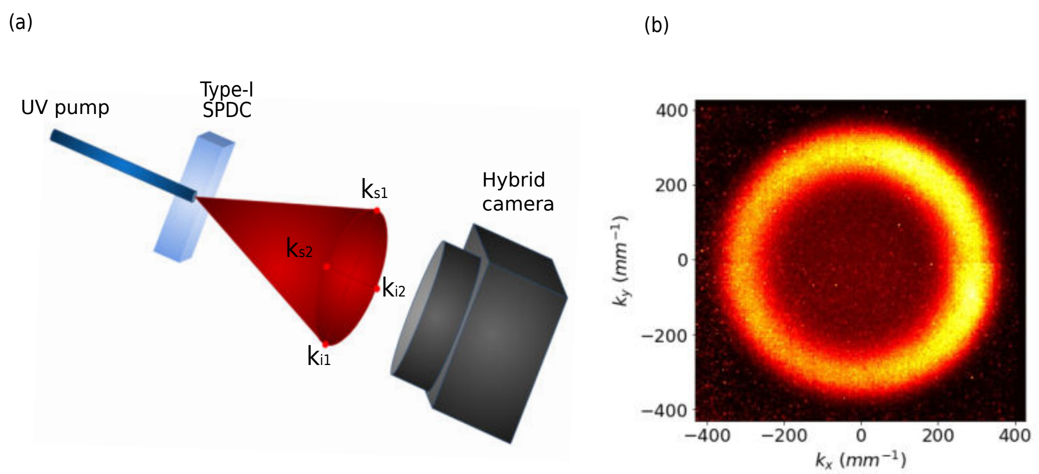

FIGURE 3.7: SPDC - I demonstration. **(a)** nonlinear crystal (χ_2) is pumped with a UV laser generating signal, s and idler, i photons in a cone-like structure in which their transverse momenta are opposite to each other. **(b)** The measured intensity distribution of the down-converted photons in the far field, where k_x and k_y are the detected transverse momenta respectively.

signal and idler photons are emitted in a cone-like structure in which their transverse momenta are opposite to each other. This phenomenon can be understood by considering the conservation of momentum in the transverse plane. When a pump photon (UV) is converted into a signal and an idler photon (NIR), the conservation of transverse momentum requires that the sum of the transverse momenta of the signal and idler photons equals the transverse momentum of the pump photon. Since the pump beam typically has a narrow transverse momentum distribution centered around zero, the signal and idler photons have approximately equal and opposite transverse momenta in order to satisfy the conservation requirement. This results in the cone-like emission pattern observed in type-I SPDC, leading to a symmetric distribution around the central axis (Fig. 3.7a). In Fig. 3.7b, we see the typical far-field SPDC type-I intensity pattern (ring) which we measured.

3.4.1 Generating type-I SPDC light

The apparatus we use for our experiment is depicted in Fig.3.8. Spatially entangled photon pairs are produced via a non-collinear, type-I spontaneous parametric down-conversion process in a 2 mm long β-barium borate (BBO) nonlinear crystal pumped with a 405 nm laser beam of approximately 20 mW from a continuous wave diode laser. The spatially filtered pump beam is focused onto the BBO crystal with the lens L_1 of focal length 400 mm. Both signal and idler photons generated as a pair by the pump beam of diameter 480 μm ($1/e^2$) in the crystal plane are of the same central wavelength (810 nm). Both photons have the same polarization. After the crystal, a combination of two long-pass filters is used to block the pump beam. In the far-field configuration, these degenerate photons propagate through a composite Fourier system with an effective focal length of f_e = 120 mm which is represented by the lens L_2 in Fig.3.8. This composite system is made of three lenses of focal lengths 75 mm, 125 mm, and 200 mm respectively. The Fourier plane of the output of the BBO crystal is imaged onto the photocathode of the image intensifier which we are gating adaptively. Before detection, the photon pairs emitted around the degeneracy are spectrally selected by a narrow-band (810 $\pm$ 2 nm) interference filter (IF). In order to meet the phase-matching condition SPDC process, a half-wave plate ($\lambda/2$) is used to set the polarization of the pump.

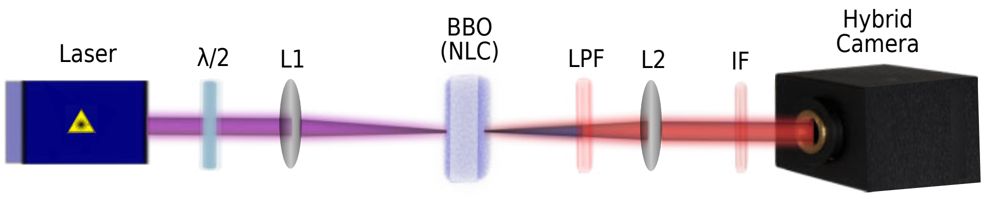

FIGURE 3.8: Experimental setup for momentum correlation characterization of photon-pairs generated via type-I SPDC source. Pump laser (cw) – 405 nm; BBO – beta-barium borate (2 mm long); L1 and L2 - lenses of effective focal lengths of 400 mm and 120 mm respectively; LPF – a combination of two long pass filters; IF – Interference filter centered at 810 nm with the bandwidth (FWHM) of 2 nm.

3.4.2 Photon transverse momentum correlation measurements with adaptively gated HIC

The experimental results of photon transverse momentum correlation measurements with our hybrid camera setup are shown in Fig. 3.9a-c. We verified the correctness of the gating by measuring the momentum correlations of signal and idler photons in the Fourier space. Since we only want to observe single photon-pair creation events, we set our camera for single photon detection. The camera should close after detecting the first photon because photons are created at the same time and the ones arriving at the camera are delayed by no more than a nanosecond.

The correlated photons have opposite transverse momenta and therefore lie on opposite sides of the center of the beam creating a ring. We can visualize it on two graphs, one per dimension (Fig. 3.9a–b). These intense anti-diagonal patterns are formed because the signal and idler photons possess opposite transverse momenta.

As a result, when the signal photon's transverse momentum increases in one direction, the idler photon's transverse momentum increases in the opposite direction, and vice versa. In a one-dimensional plot, this relationship manifests as a line with the negative slope (Fig. 3.9a–b), which represents the anti-correlation of the transverse momenta.

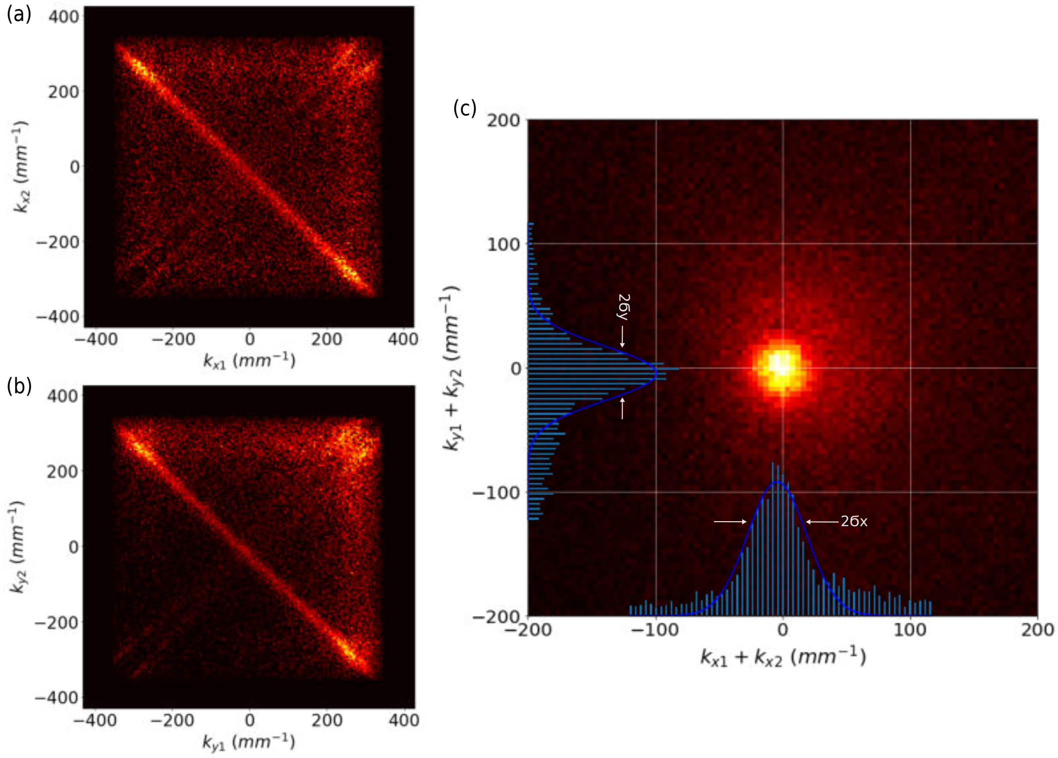

FIGURE 3.9: Results of photon transverse momentum correlation measurements. **(a-b)** Measured two-photon momentum correlations between signal and idler photons along k_x and k_y – the subscripts 1, 2 represent signal and idler generated in SPDC. Correlation plots are represented after background correlation subtraction (i.e., coincidence counts after accidental coincidence correction). **(c)** Measured correlation peak at the center of the transverse momentum sum-coordinates projection. The central peak is fitted with a Gaussian function to obtain its center and widths (standard deviations) along both k_x and k_y, where σ_x is 24.43 mm^{-1} and σ_y is 22.67 mm^{-1}.

To retrieve the two-photon momentum correlation, we remove the background noise. We measure this background noise by measuring the correlations between two photons detected on consecutive frames (accidental coincidences). Later we subtract this correlation. The peak of the correlation at the center of the sum coordinate projection (Fig. 3.9c) is a signature of strong anti-correlations between two photons imposed by momentum conservation (phase-matching) in the pair production process via SPDC. The presence of this peak indicates that the signal and idler photons have nearly equal and opposite transverse momenta in both the x and y directions. While a narrower peak is indicative of stronger anti-correlations and, thus, stronger entanglement, a broader peak suggests weaker anti-correlations and entanglement.

We obtained correlations for approximately 194 spatial modes in the momentum basis. To estimate the number of correlated modes, we divided the area of the intensity ring by the square of the correlation length. The correlation length corresponds to the size of the spatial mode in the far field, which we determined by fitting a Gaussian function to the correlation peak in the sum coordinate and extracting the standard deviations σ_x and σ_y. This result indicates how many distinct spatial modes are in the intensity ring, which represents the spatial distribution of the down-converted photons [97].

When a photon hits the photocathode of the image intensifier, it has the potential to release an electron. This electron is then accelerated towards the MCP, and upon collision with the MCP wall, secondary electrons are produced, initiating the avalanche gain process. However, some of these electrons can deflect and re-enter neighboring channels, triggering additional avalanches. Such events, known as cross-talk, can lead to strong artificial correlations when recorded in the same camera frame. To address this issue, we exclude photons detected within a proximity of 100 pixels from each other. Implementing this subtraction technique is crucial when working with an MCP to ensure the removal of these false correlations from our data [98].

3.5 Comparison between the schemes with and without adaptive gating of intensifier

We conducted a performance comparison between the adaptively gated hybrid camera setup and a non-adaptive setup using an intensified sCMOS camera, where the image intensifier is gated once per camera frame. The time interval between consecutive frames is typically 6 orders of magnitude longer than the minimum gating time of an intensified sCMOS camera[94, 29] (an intensified sCMOS camera can typically achieve a frame rate of around 100 Hz at full spatial resolution with a gate length in the nanoseconds range).

In the standard non-adaptive approach, we externally gate the image intensifier using signals from a digital pulse generator [29, 94]. In contrast, the adaptive gating approach employs a feedback loop to determine the duration of the gating window. This technique allows for the observation of a single photon triggering the adaptive exposure and any additional photons detected within the coincidence window, which is the time between the first photon detection and the closing of the image intensifier (approximately 150 ns in our case). We compared adaptive gating with standard (non-adaptive) gating with a gating time of 150 ns to achieve similar probabilities of registering false coincidences as in the adaptive case. Additionally, we conducted measurements using two other gating window sizes (500 ns and 5 μs) as reference points when comparing our adaptive gating method to the non-adaptive approach with a 150 ns gating window.

The experimental results, presented in Fig. 3.10, compare the measured histograms of frame numbers with specific photon counts for the adaptive gating approach (purple bars) and standard non-adaptive gating cases (green, red, and blue bars for 150 ns, 500 ns, and 5 μs gating windows, respectively). In both cases, the objective is to observe single photon-pair creation events. In the case of non-adaptive gating, we observed that the majority of recorded frames were empty (see green bars), which was necessary to maintain low signal levels and prevent accidental coincidence detections, mostly originating from separate photon-pair generation events.

The comparison of experimental outcomes for the number of detected photons per frame in both adaptive and non-adaptive methods (Fig. 3.10) demonstrates the potential of the adaptive gating approach to enhance data acquisition rates. As our focus is on observing single photon-pair creation events, we set our camera for single

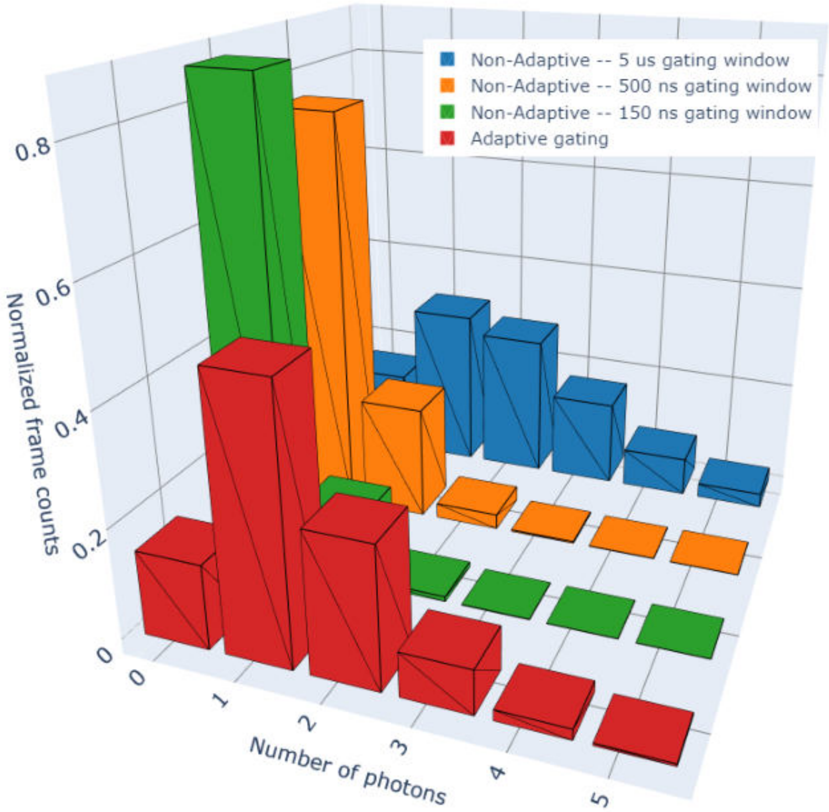

FIGURE 3.10: A comparison of frame numbers with specific photon counts between adaptive gating and non-adaptive gating scenarios. The experiment involved generating single-photon pairs through SPDC and registering them using an identical setup. Ideally, triggering a single photon detection on the camera would lead to the observation of two photons, as they naturally appear in pairs, resulting in the highest bar in the setup. However, the probabilities of registering one, two, or more photons were influenced by losses and the low quantum efficiency of the image intensifier. The success rate for adaptive gating, where one and two-photon frames were considered as indicators of success, reached approximately 77.6% frames triggered correctly. In contrast, the non-adaptive gating approach, using a 150 *ns* gate window, achieved a significantly lower success rate of only about 13.7%.

photon detection. The image intensifier gate closes after detecting the first photon, as, in SPDC, photons are generated simultaneously. Assuming no losses in the setup and a 100% quantum efficiency of the detector, we would anticipate most counts to be pairs from the SPDC, with only a small number of multi-photon events consisting of additional noise photons or multiple pair detections. However, due to factors such as electrical noise and dark counts, the PMT detects some false events that are not registered by the sCMOS camera, resulting in some empty frames in the histogram for adaptive gating (Fig. 3.10). Furthermore, the low (below 20%) quantum efficiency of the image intensifier and optical losses mean that coincidences are not always observed; hence, we consider one and two-photon frames as indicative of the adaptive gating success.

Consequently, we achieved a success rate of approximately 77.6% frames triggered correctly, while the non-adaptive gating (with a 150 ns gating window) scenario yielded a success rate of only 13.7%; an improvement of around 5.6 times. Moreover, increasing the gating window size in the non-adaptive approach results in an increased false coincidence rate despite the lower number of empty frames present (see Fig. 3.10).

3.6 Conclusions

In conclusion, our study presented a single-photon sensitive hybrid camera that allows for adaptive control of the image intensifier to select the number of detected photons. The key advantage of this approach is a significant increase in data acquisition speed compared to standard non-adaptive approaches. The possibility of gate-time adjustment to the rate of photon detection through a fast feedback loop based on FPGA was also demonstrated, providing more precise control over the acquisition process.

Furthermore, our active approach surpasses the probabilistic approach, which can only predict the expected value of a parameter, such as the opening time of the image intensifier. The approach is based on the continuous counting of photons in real-time and using the information on their number to terminate the ongoing acquisition process. This technique benefits from the dual measurement nature of the device and allows for fine-tuning of the acquisition time immediately after photon detection by the fast detector.

Our study also showed the effectiveness of our detection technique in observing quantum optical effects, such as the SPDC process. This highlights the potential of our camera in fundamental quantum information science and its prospective applications, including quantum plenoptic imaging [84, 99], quantum walks of correlated photons [100, 101], quantum correlations in scattering media [102, 103], and Boson sampling [104].

Finally, the challenges faced by conventional intensified cameras, such as intensified CCD and CMOS, have been overcome by our hybrid camera. This was achieved by adding a fast feedback loop and offering a multi-megapixel resolution that is unobtainable by the current SPAD arrays. The unprecedented capability of our camera to detect single photon events with high spatial and temporal resolution makes it highly suitable for various imaging applications, especially those requiring the detection of single photon-pair creation events.

The electronics part, optomechanics, and software for the camera control were developed by Jerzy Szuniewicz. Grzegorz helped with electronics and camera setup building and Alexander Krupinski-Ptaszek contributed to part of data analysis. Sanjukta Kundu contributed to alignment, preparing the entangled photon pair source, performing measurements, analyzing data, and writing the manuscript.

Chapter 4

Nonclassical interference of spatially entangled photon-pairs

This chapter is mainly devoted to studying the momentum correlations of photon pairs generated in the SPDC process, using a novel technique named quantum imaging with an undetected photon (QIUP) [56]. Unlike the last chapter, which relied on direct coincidence detection, this approach involves a nonlinear interferometer. We begin with reviewing two kinds of nonlinear quantum interferometers in the low-gain regime based on induced coherence without induced emission, which are known as Zou-Wang-Mandel (ZWM) type interferometer [45] and frustrated two-photon creation interferometer (FTPCI) [46] – rooted in the generation of entangled photon pairs in a quantum superposition, originating from two distinct, spatially separated SPDC sources. We provide the theoretical background for both of the aforementioned interferometers and discuss the fundamental differences. We mainly focus on the frustrated type interferometry for our experimental investigation. Later in this section, we provide a brief overview of how to reconstruct the properties of objects without requiring the detection of light that has interacted with the object being imaged [56, 105]. In this process, one photon from the SPDC pair (idler photon), interacts with the object under investigation. Remarkably, this idler photon is never detected. This is why it's called quantum imaging with undetected photons (QIUP). Later on, we characterize the momentum correlations of the two-photon pair by detecting only one of them (without coincidence detection) using the FTPI setup. We will see that the visibility of the interference pattern of signal beams depends on the momentum correlation between signal and idler photons [7] and discuss the future prospect of characterizing Einstein–Podolsky–Rosen (EPR) type correlations using such a setup for proving position-momentum type entanglement.

A manuscript about the research presented in this chapter is in preparation.

4.1 Overview of nonlinear interferometers in the low-gain regime

Quantum technology has the potential to revolutionize imaging applications, with several promising imaging techniques that harness the unique properties of quantum systems. These techniques, such as interaction-free imaging [106], ghost imaging [107, 108, 57, 25, 55], and quantum imaging with undetected photons (QIUP) [56, 105], offer unprecedented imaging capabilities that surpass the classical limits of sensitivity [109, 110, 111, 112], spatial resolution [113, 114], and phase metrology [115, 116, 117].

QIUP is a novel imaging technique that operates without directly detecting the photons that illuminate the object. Instead, it is rooted in the generation of entangled photon pairs in a quantum superposition. In this process, one photon from each pair (idler photon), interacts with the object under investigation, encoding essential information from the object within its quantum state. Remarkably, this idler photon is never directly detected.

Conversely, the other photon of the pair (signal photon) does not interact with the object but shares a strong quantum correlation with its idler counterpart. Consequently, the signal photon carries crucial information about the object, despite not interacting with it. The imaging process in QIUP capitalizes on this correlation by solely detecting the signal photons. By doing so, the image of the object is effectively reconstructed without ever directly measuring the photons that interacted with the object itself.

The concept of QUIP is based on induced coherence without emission [45] and this method is fundamentally different than the interaction-free or ghost imaging techniques since it does not require coincidence or post-selected measurements to obtain the image [56, 118].

In the field of quantum imaging with undetected photons, the majority of nonlinear interferometers employed thus far adopt one of two key configurations. The first configuration is founded upon a quantum interference experiment pioneered by Zou, Wang, and Mandel, as showcased in Fig. 4.1. On the other hand, the alternative configuration is inspired by Herzog's frustrated two-photon interferometry, which is illustrated in Fig. 4.2. Both of these two nonlinear interferometers are in the low-gain regime. These two distinct configurations have been extensively utilized in QIUP, contributing to advancements in the field of quantum imaging technologies.

4.1.1 Zou-Wang-Mandel type interferometer

One of the fundamental principles of quantum mechanics states that if an event can happen in multiple alternative ways and there are no means to distinguish between these alternatives, interference will occur. In 1991, a team consisting of Zou, Wang, and Mandel, with valuable insights from Jeff Ou, set out to investigate the relationship between quantum indistinguishability and interference [45, 119, 56, 120]. They accomplished this by creating an interferometer that couldn't be explained by classical wave optics models. Prof. Mandel and the group took the concept of indistinguishability to a new level. Instead of dealing with superpositions of individual photons, they focused on superpositions of the origin of photon pairs themselves. To achieve this, they utilized the idea proposed by Jeff Ou, which involved making the paths of one photon from each pair produced by the different SPDC sources overlap or identical, such that it cannot be distinguished from which source they originated.

In their experimental configuration (depicted in Fig. 4.1), two similar nonlinear crystals, NL1 and NL2, are subjected to optical pumping by two mutually coherent, classical pump beams. This process led to parametric down-conversions in both crystals, resulting in the emission of a signal photon and an idler photon from each crystal. We consider a regime in which it is very unlikely to generate more than one pair at a time. When the paths of the idler photons from NL1 and NL2 are aligned, interference occurs between the signal photons from each crystal at beam splitter BS2. This interference arises because the aligned paths of the idler photons induce coherence in the signal photon paths, even in the absence of induced emission from NL2. When the trajectories of the idler photons from both crystals overlap, it becomes indistinguishable as to whether the photon pairs originated from NL1 or

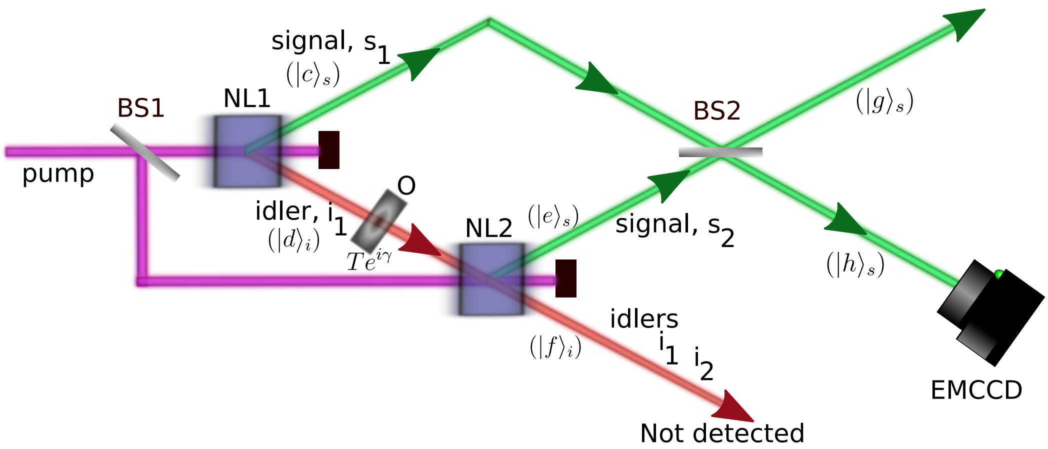

FIGURE 4.1: Schematic demonstration of a Zou-Wang-Mandel type interferometer – quantum imaging with undetected photons [56]. The setup involves pumping (purple beam) two nonlinear crystals to create a photon pair (of green and red). By making the idler photon's path indistinguishable, interference occurs at a beam splitter, BS2 with the green photon's (signal photons) superposition of the upper or lower path. Introducing an object into the overlapped idler path partially distinguishes the origins, which will be observable in the interference pattern. Remarkably, the image can be constructed without detecting any idler (red) photons. This concept differs significantly from conventional ghost imaging, which requires detecting both photons and can be done classically.

NL2. Interference between signal photons, s1 from NL1 and s2 from NL2, is influenced by their undetected idler counterparts. A lack of coherence from the idler photons diminishes the interference contrast observed at the output of BS2.

A decade later, the concept was expanded to include the imaging of an object without the need to detect the photons that interacted with the object directly. As described in the reference [56, 121], the signal-idler photon pairs generated in NL1 and NL2 can be represented as $|c\rangle_s |d\rangle_i$ and $|e\rangle_s |f\rangle_i$ states respectively (where c, d, e, and f represent the spatial modes of the photons). When the idler from NL1 passes through an object O with a real transmittance coefficient T and phase shift γ, the pair undergoes a transformation from $|c\rangle_s |d\rangle_i$ to [56]:

$$Te^{i\gamma} |c\rangle_s |d\rangle_i + \sqrt{1-T^2}\, |c\rangle_s |w\rangle_i\,, \tag{4.1}$$

where the lost idler amplitude is represented by a state $|w\rangle_i$. If the idler from NL1, after passing through the object, perfectly aligns with the idler amplitude created at NL2 (i.e., $|d\rangle_i \rightarrow |f\rangle_i$), a modulation in the interference pattern of the signal photons (s1, s2) is observed, representing the spatial features of the object O. By tracing out the idler modes, the resulting detection probabilities of signal photons at both outputs ($|g\rangle_s$ and $|h\rangle_s$) are [56]:

$$p_{g/h} = [1 \pm T\cos\gamma]. \tag{4.2}$$

To obtain the image, the interferometric phase scanned, and for each pixel, the visibility and phase of the interference signal were extracted. The image of the object is encoded in visibility. Constructive interference is seen at one output of the beam splitter and destructive interference is observed in the other output. As a result, fringes with visibility of T can be observed at either output, despite the fact that the signals combined at BS2 originate from different sources. By subtracting the outputs of BS2, the interference contrast is increased. On the other hand, adding the outputs provides the intensity profile of the signal beams.

4.1.2 Frustrated two-photon creation interferometer (FTPCI)

We focus on the frustrated two-photon creation interferometer (FTPCI) type configuration for our experimental purposes (Fig. 4.2) [46]. In this nonlinear interferometer type, only one crystal is used instead of two, achieved by double-passing the crystal. Both the pump and the signal and idler photons are reflected back through the same crystal. Thus the two possible ways of photon pair creation, i.e. forward and backward, can interfere. This type of a nonlinear interferometer bears a resemblance to the Michelson interferometer. For instance, we can modulate the idler1 beam (i1) by a spatial light modulator to imprint a phase mask to idler (i1) photons. The modulation imposed on i1 is seen in the interference fringe pattern of signal photons (s1 and s2).

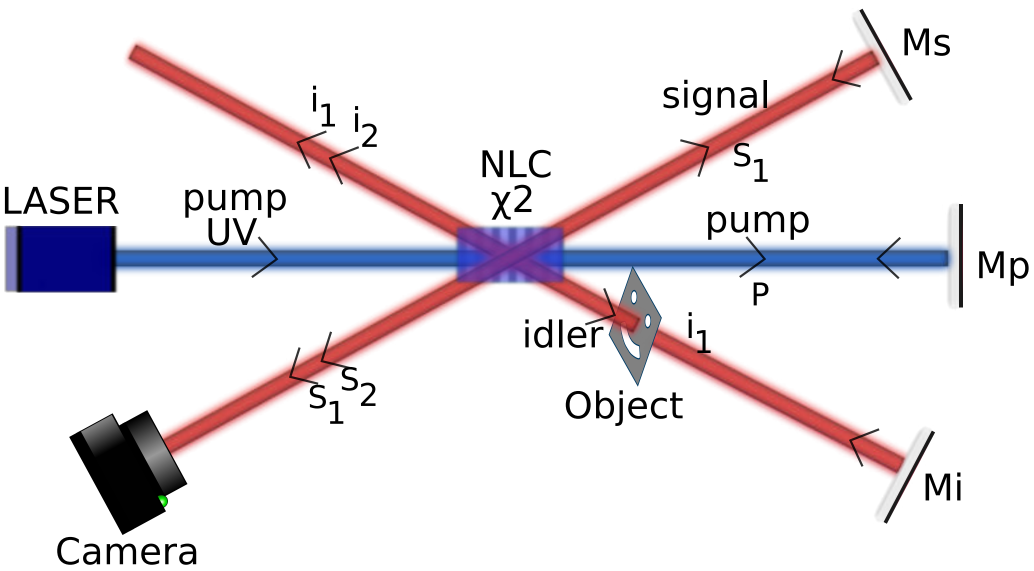

FIGURE 4.2: Schematic representation of the frustrated two-photon interferometry. This nonlinear interferometer is formed by double passing the crystal – pump and both signal and idler photons get reflected back by mirrors (M_p, M_s, M_i) and pass the same crystal twice. Interference arises from photon pair creation in either the forward (first) or backward (second) pass of the pump through the same crystal [46]. Modulating forward-generated idler1 beam (i1) using an object or spatial light modulator reveals interference fringe patterns in signal1 (s1) and signal2 (s2), resulting from induced coherence without induced emission.

Let's consider that $|a\rangle_s |b\rangle_i$ is the signal-idler pair generated at the forward propagation of the pump and ϕ_p is the phase difference accumulated by the pump beam between the two emission processes and ϕ_s and ϕ_i are the phases accumulated by the first signal and idler respectively. If we reflect the forward-generated signal-idler modes back through the crystal such that they overlap with the backward-generated signal-idler modes, the resulting two-photon state becomes:

$$\alpha[e^{i\phi_p} + e^{i(\phi_s+\phi_i)})] \, |a\rangle_s |b\rangle_i \, ; \tag{4.3}$$

where α is the amplitude for emitting the photon pair into the spatial modes $|a\rangle_s\,|b\rangle_i$. The intensities I_s (signal count rate) and I_i (idler count rate) vary identically and they will be proportional to $[1+\cos(\phi_s+\phi_i-\phi_p)]$.

4.1.3 Experimental setup for frustrated two-photon interferometry with type-I SPDC crystal

Here we introduce a frustrated two-photon-based interferometer. Initially, we decided to start with a rather simple setup to investigate the role of spatial correlations of photon pairs in non-linear interferometers and to study quantum imaging in such a setup without coincidence detection.

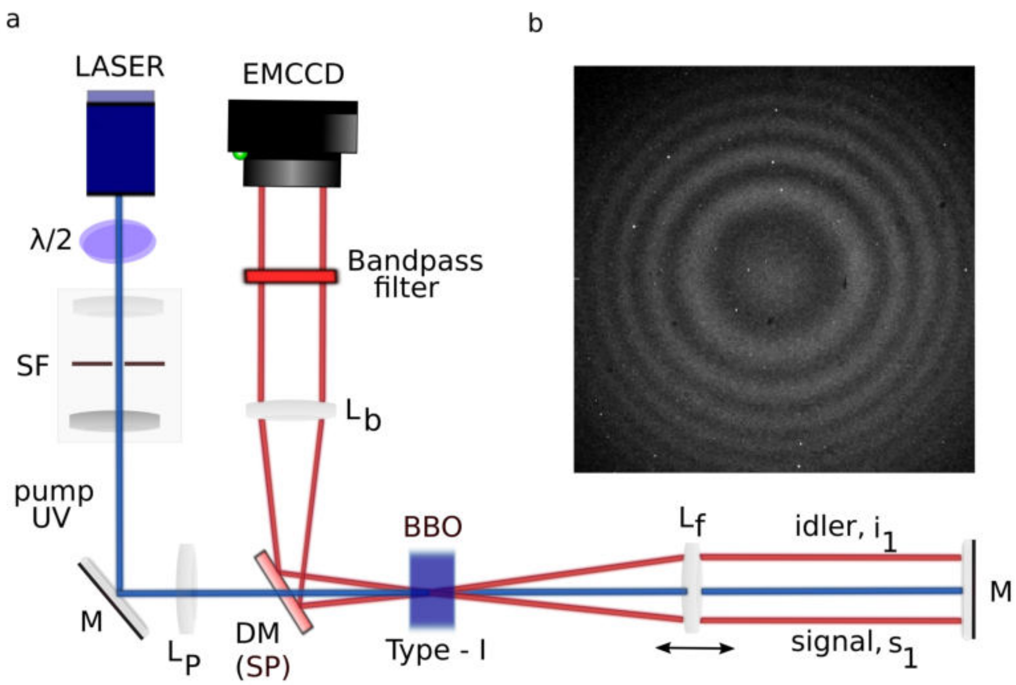

FIGURE 4.3: Frustrated two photon interferometer with type-I nonlinear crystal. **(a)** A 405 nm CW laser pumps a type-I nonlinear crystal, BBO. A mirror M is placed at the Fourier plane of BBO with respect to an achromatic lens L_f of focal length 75 mm. Generated non-colinear signal-idler pair and the pump beam get reflected back, recombined, and back propagated through BBO. The short pass dichroic mirror DM (SP) separates the pump from the signal-idler pair of 810 nm into different beam paths directing all the generated both forward and backward signal-idler photons toward the EMCCD camera. s1, s2, and i1, i2 photons are spectrally filtered with the bandpass filter of 3 nm bandwidth before detection. The Fourier plane of the BBO crystal is imaged onto the camera with a lens L_b of focal length 75 mm. **(b)** We observe the interference of the s1 with s2 and i1 with i2. Spatially dependent circular fringe interference pattern results from imaging system defocusing in the BBO crystal facilitated by achromatic lens L_f.

This setup utilizes a type - I SPDC two-photon pair source made of a 2 mm long BBO crystal (Fig. 4.3a). The crystal is pumped by a spatially filtered 405 nm laser beam of approximately 10 mW from a continuous wave diode laser. The pump beam is focused onto the BBO crystal using a lens L_p with a focal length of 400 mm. Upon reaching the crystal plane, the pump beam, with a diameter of 480 μm

($1/e^2$), produces signal and idler photon pairs in the type I process (s1, i1 – forward generated) of identical central wavelengths (810 nm) and polarization.

A mirror (M) is placed at the Fourier plane of the BBO crystal with respect to the lens L_f, reflecting the pump, forward generated signal (s1), and idler (i1) photons back. L_f is an achromatic lens with a focal length of 75 mm, which images the BBO crystal onto itself with the help of mirror M. The reflected (back-propagated) pump beam generates another signal-idler pair (s2, and i2). A short-pass dichroic mirror (DM) is employed to separate the signals (s1, and s2), and idlers (i1, and i2) from the pump beam, directing them toward the EMCCD camera. The BBO's Fourier plane is imaged onto the EMCCD using a lens L_b with a focal length of 75 mm. When perfectly aligned, a uniform interference pattern, resulting from the interferometric phase shift between the forward-generated (s1, i1) and back-propagated (s2, i2) photon pairs, should be observable as either a bright or dark spot on the camera. The spatially dependent interference pattern, characterized by circular fringes as depicted in Fig. 4.3b, arises due to the defocusing of the imaging system. This defocusing occurs during the first photon pair creation and subsequently during the second photon pair creation, by moving the achromatic lens L_f axially due to which there is some residual quadratic phase. By placing a quarter-wave plate ($\lambda/4$) designed for UV light between the crystal and the mirror, M, the polarization of the reflected pump beam is adjusted. This leads to the absence of the phase-matching condition for the SPDC process during the second pass (backward) of the pump beam through the crystal. As a result, the interference fringes disappear, thereby confirming that the observed fringes are indeed of the FTPI type.

4.1.4 Quantum Imaging with Undetected Photons: frustrated interferometry and Type-II SPDC crystal

For quantum imaging with undetected photons, we considered a different experimental setup using the colinear type - II SPDC process (Fig. 4.4). In the setup, a 405 nm UV laser light, which has undergone spatial filtering (SF), is used to pump a 2 mm long nonlinear periodically poled potassium titanyl phosphate (ppKTP) crystal maintained at a temperature of 32°C. Focusing of the pump beam into the ppKTP crystal is achieved with a lens L_{p1} of a focal length of 300 mm. This process results in the degenerate, collinear, orthogonally polarized signal and idler photon pair generation of wavelength 810 nm. To separate the pump beam from the 810 nm signal-idler beams, dichroic mirrors DM as well as long-pass (LP) and short-pass (SP) filters are utilized, directing the beams along distinct optical paths. A polarizing beam splitter (PBS) is then employed to separate the orthogonally polarized idler and signal photons. In the interferometer configuration, end mirrors for the pump, signal, and idler paths are represented by mirrors M_p, M_s, and M_i, respectively. The pump beam passes through the crystal twice, generating photon pairs during each pass. In the low pump power regime, the probability of simultaneously generating two pairs of photons is negligible. The mirror M_s is mounted on a piezo stage in order to scan the interferometric phase. A quarter-wave plate ($\lambda/4$) designed for UV light is positioned in the pump path prior to the mirror M_p to adjust the polarization of the reflected pump beam. This is for switching the backward emission off. The imaging system comprises lenses designated as L_{p2}, L_s, L_i, and L_b, each with a focal length of 200 mm. In the paths for the pump, signal, and idler, the lenses L_{p2}, L_s, L_i are utilized to image the crystal onto itself using a 4f setup. Additionally, with the lens L_b in the detection path, the EMCCD is positioned at the Fourier plane of

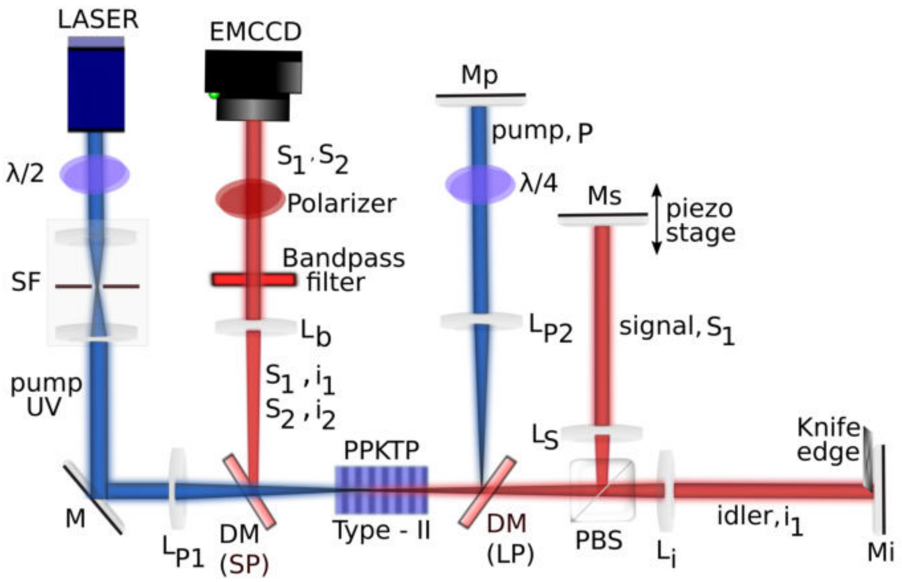

FIGURE 4.4: Experimental setup for quantum imaging with undetected photons. Laser light (UV of 405 nm) after being spatially filtered (SF) pumps the nonlinear crystal (ppKTP). A lens L_{p1} with a focal length of 300 mm focuses the pump beam in the PPKTP crystal and generates signal and idler (810 nm) beams either in the forward direction or backward direction after reflection. Dichroic mirrors DM (Long pass – LP, short pass - SP) separate the pump from the signal-idler pair of 810 nm. A polarizing beam splitter separates the orthogonally polarized idler and signal photons. The mirrors M_p, M_s, and M_i are the interferometer end mirrors in the pump, signal, and idler paths, respectively. M_s is mounted on a piezo stage to precisely move the mirror in one direction to scan the interferometric phase. In the idler beam path of the interferometer, a knife edge is used as an object in front of the mirror M_i, in such a way that a part of the idler beam, i_1 is blocked. The object (knife-edge) and the camera are placed in the Fourier planes of the nonlinear crystal (PPKTP) where the photon pairs (signal and idler) are emitted. On the EMCCD camera, we only detect interference fringes of the signal photons (s_1 and s_2) using the polarizer because idler photons are blocked by the polarizer. Due to induced coherence, the modulation imposed on i1 is still seen in the signal fringes enabling us to certify position-momentum type entanglement in the SPDC process. Lenses (L_{p2}, L_s, L_i, L_b) form the imaging system with focal distances of 200 mm. Th lenses L_{p2}, L_s, L_i are utilized to image the crystal onto itself and with the lens L_b the EMCCD is positioned at the Fourier plane of the crystal. Before detection, a narrow bandpass filter is used to spectrally select light centered at 810 nm with bandwith of 2 nm. The quarter-wave plate ($\lambda/4$) is used to adjust the polarization of the reflected pump beam so that the phase-matching condition for the SPDC process was met during the second occurrence.

the crystal. In the setup, idler photons, labeled as i_1 and i_2, generated during either the first or the second pass, are effectively blocked and go undetected. This is achieved using a polarizer positioned in front of the EMCCD. The polarizer's orientation is chosen such that it permits only the signal photons, denoted as s_1 and s_2, to pass through. As a result, any interference fringes observed on the EMCCD are exclusively due to these signal photons, with no contribution from the idler photons. A knife edge is placed as an object in front of the mirror M_i within the idler beam path of the interferometer, resulting in the partial obstruction of the idler beam (undetected photons).

The object (in this case, a knife edge) and the camera are located at the Fourier planes of the nonlinear crystal where the down-converted photon pairs are produced (Fig. 4.4). The photon pair created in the first pass of the pump beam needs to be aligned accurately to overlap with the photon pair generated during the second pass. The interference of the idler photon with itself is then observed by detecting the signal photons (s1 and s2) using an EMCCD camera.

To build this interferometer, precise alignment is crucial to avoid any off-centered or tilted elements so that the trajectories of idler photons generated forward and backward overlap. During the measurement process, the idler photons (i1) generated during the first pass of the pump through the crystal are spatially modulated using a knife-edge type object or a spatial light modulator (SLM). This modulation results in spatial interferometric fringes. A well-designed spatial modulation of the idler photons, along with imaging of the signal photons, allows for the observation of QIUP without the need for coincidence detection of signal and idler photons.

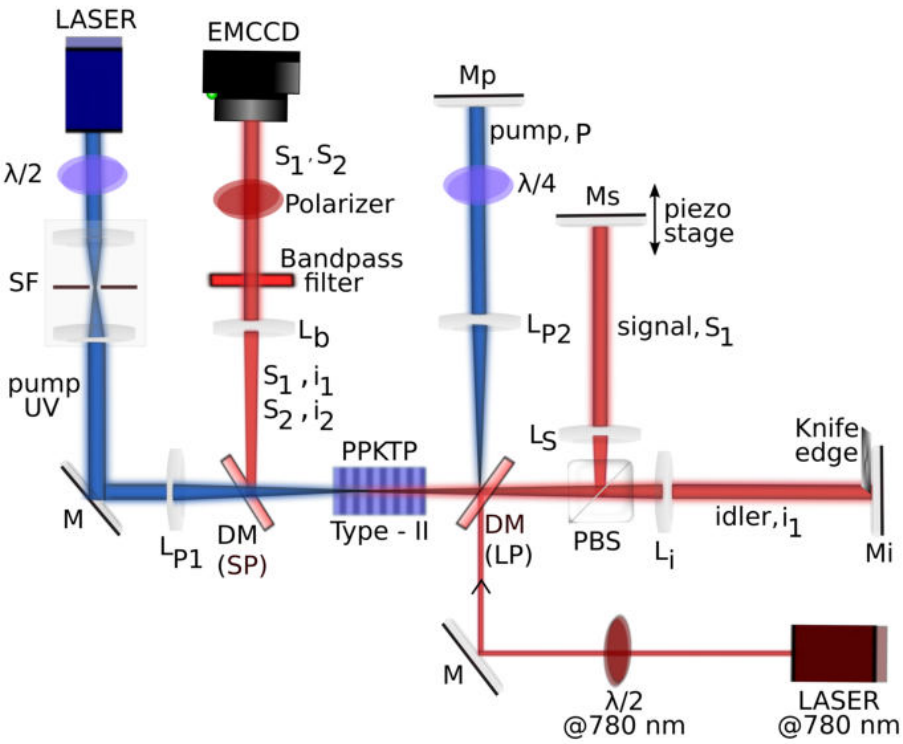

FIGURE 4.5: Zero delay adjustment in the folded interferometric geometry among the three interferometric paths respectively. We used a separate laser operating under the threshold to align all three interferometric arms to be within the zero delay.

To ensure the indistinguishability of photon pair emitted as the pump beam passes through the crystal twice, it is crucial to maintain the same time delay between the arrival of the signal and idler generated for each pass at the crystal. This requires adjusting the pump, signal, and idler's optical path lengths to achieve a zero-delay condition. To simplify the task of achieving zero delay across the three paths, we utilize an additional laser with a wavelength of 780 nm (Fig. 4.5), operating below its threshold. While the spatial coherence is still maintained, the spectral linewidth of the laser becomes broadened under this condition. This broader linewidth reduces the coherence length, making it easier to identify the zero-delay condition with a higher tolerance for small deviations in path lengths. This approach is particularly useful in such experiments where precise alignment or path length matching is challenging.

During the first pass of the pump laser (H-polarized), it generates signal and idler photons with V and H polarizations, respectively. The range of possible delays between H - and V - polarized photons is from 0 to τ, where τ corresponds to the delay for the crystal length, L = 2 mm. When the signal and idler are back-reflected, the delay varies between 0 and 2τ. The back-reflected pump beam generates the photon pair for a second time. Consequently, the path difference between the forward and backward-generated horizontally polarized idler photons ranges from 0 to τ. This results in a path difference of approximately 180 μm, calculated as $(1.84 - 1.75) \times 2$ mm $\approx$ 180 μm (Fig. 4.6a).[1] In our experiment, the coherence length of the UV pump laser is approximately 500 μm. Meanwhile, the photons' coherence length is determined by the 3 nm filtering applied, leading us to estimate their coherence length at about 200 μm.

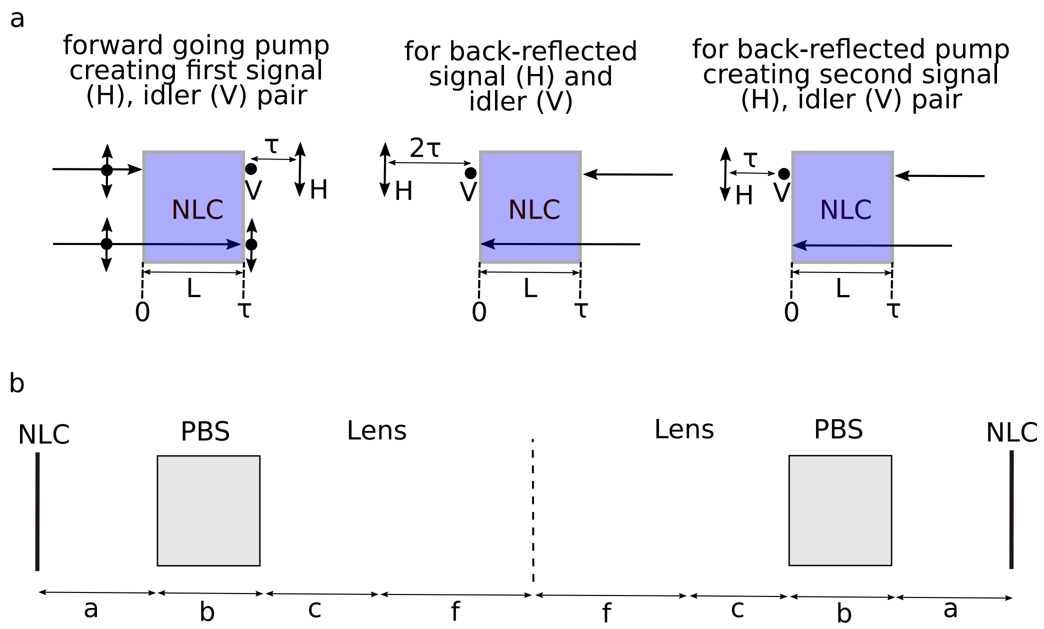

FIGURE 4.6: Path difference introduced due to the birefringence of the PPKTP crystal and a thick PBS. **(a)** represents the delay acquired between signal and idler photos generated during forward and backward propagation in the frustrated two-photon interferometer setup; τ corresponds to the delay introduced during the propagation through the full length of the nonlinear crystal L; H, and V are the polarizations of signal and idler photons, respectively. **(b)** represents the entire imaging system from the NLC to PBS, lens, mirror, and back to the lens, PBS, and NLC again. This is for a simpler visualization of the imaging system in the interferometer and to calculate the path delay introduced by the thick PBS between the signal and idler arm in the interferometer.

[1]For our ppKTP crystal (Raicol for OPO of 405→810 nm; 7 – 112213504; 1 × 2 × 2, AR@810/405 nm), the parameters for type-II SPDC are as follows:

Refractive indices: n_y (pump) = 1.840581922 (λ_{pump} = 405 nm); n_z (signal) = 1.844367226 (λ_{signal} = 810 nm); n_y (idler) = 1.756053347 (λ_{idler} = 810 nm).

We observed that using a cube PBS (1 inch thick in our case) introduces a trade-off between establishing a proper imaging system and achieving zero delay simultaneously. From the ABCD matrix calculation (Fig. 4.6b) for the crystal being imaged onto itself, with the two mirrors M_s and M_i located at the Fourier planes of the crystal, we determined that the mirrors should be further than the focal length distance, f, from the lens L_s or L_i by an amount denoted as δz for proper imaging due to refraction at the walls of the PBS.

The ABCD matrix for the PBS with a refractive index of n (1.5) and a thickness of b (2.54 cm) is given by:

$$\begin{bmatrix} 1 & b/n \\ 0 & 1 \end{bmatrix}, \tag{4.4}$$

and the ABCD matrix for a thin convex lens is given by:

$$\begin{bmatrix} 1 & 0 \\ -1/f & 1 \end{bmatrix}. \tag{4.5}$$

To calculate δz, we consider the entire imaging system from the non-linear crystal (NLC) to PBS, lens, mirror, and back to the lens, PBS, and NLC again:

$$\begin{aligned} &\begin{bmatrix} 1 & a \\ 0 & 1 \end{bmatrix} \times \begin{bmatrix} 1 & b/n \\ 0 & 1 \end{bmatrix} \times \begin{bmatrix} 1 & c \\ 0 & 1 \end{bmatrix} \times \begin{bmatrix} 1 & 0 \\ -1/f & 1 \end{bmatrix} \times \\ &\qquad \begin{bmatrix} 1 & 2f \\ 0 & 1 \end{bmatrix} \times \begin{bmatrix} 1 & 0 \\ -1/f & 1 \end{bmatrix} \times \begin{bmatrix} 1 & c \\ 0 & 1 \end{bmatrix} \times \begin{bmatrix} 1 & b/n \\ 0 & 1 \end{bmatrix} \times - \begin{bmatrix} 1 & a \\ 0 & 1 \end{bmatrix} \\ &\qquad\qquad = \begin{bmatrix} -1 & 2(f-a-b/n-c) \\ 0 & -1 \end{bmatrix}. \end{aligned} \tag{4.6}$$

We aim to understand the trade-off and determine the optimal position of the mirrors for our imaging system. Without a thick PBS, normal imaging in air results in:

$$\begin{bmatrix} -1 & 0 \\ 0 & -1 \end{bmatrix}, \tag{4.7}$$

which implies:

$$f = a + b/n + c, \tag{4.8}$$

rather than just $f = a + b + c$. This leads to the following relationship:

$$(air_n) = a + c = f - b/n \tag{4.9}$$

where

$$(air_0) = a + c = f - b. \tag{4.10}$$

air_n and air_0 represent the effective optical path lengths for imaging through the PBS and in air (without the PBS), respectively. Consequently, we have:

$$\delta_z = (air_n) - (air_0) = (b - b/n) = b \times (1 - 1/n) = b/3 \approx 8.47\text{mm}. \tag{4.11}$$

Therefore, the mirrors M_s and M_i should be placed at an additional distance of δ_z (8.47 mm) from the lenses L_s, L_i, respectively.

On the other hand, to calculate the optical path lengths of the three interferometric paths and achieve zero delay, the mirrors M_s and M_i should not be positioned at $2f$ from the crystal. Instead, they should be moved closer by an amount of 2.54 ×

(1.5 - 1) = 1.27 cm, with 1.5 being the refractive index (r.i.) of the glass material of the PBS and 1 representing the r.i. of air. However, this positioning is not in the proper imaging plane, resulting in a trade-off. Consequently, we opted for a plate PBS to better serve our experimental objectives.

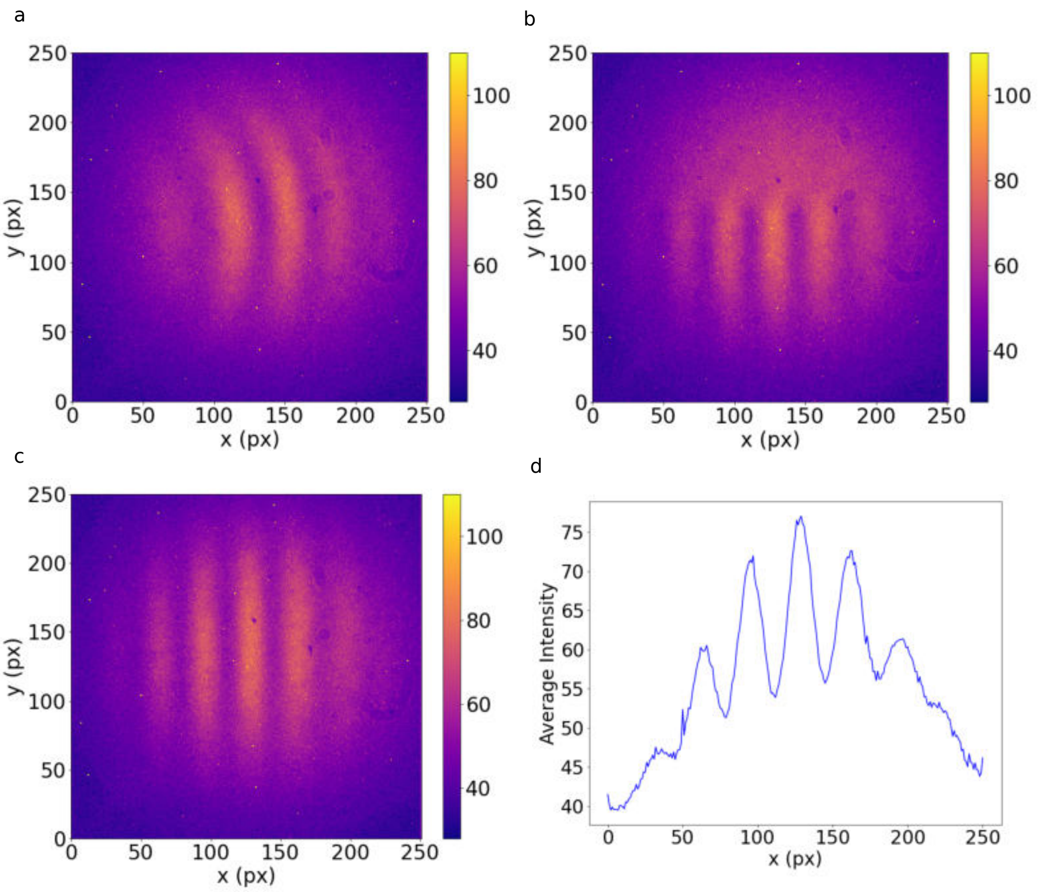

FIGURE 4.7: Experimentally observed spatially dependent interference fringes of signal photons (s1 and s2) in QIUP setup. Circular fringes are produced by slightly shifting the imaging lens L_i axially (defocusing) in the idler arm in the interferometer causing residual quadratic phase (**a**); placing a knife edge in the vicinity of the mirror M_i blocking the idler beam partially causes washing out fringes in the blocked part (**b**); where linear fringes are due to tilting the idler mirror M_i (**c**); (**d**) is an average of cross-cuts through middle 50 rows of the image (**c**).

To generate spatially dependent fringes, such as circular fringes illustrated in Fig. 4.7a, the imaging system in the idler beam is intentionally defocused. This is achieved by slightly translating a lens, denoted as L_i in Fig. 4.4, along the beam propagation axis causing a residual quadratic phase in the setup. The partial obstruction of the idler beam, i1 by the knife edge is also evident in the fringes displayed in Fig. 4.7b. By tilting the idler beam, parallel fringes (Fig. 4.7c) are produced and subsequently captured by the camera where Fig. 4.7d is 1D representation when we take an average over 50 middle rows of Fig. 4.7c.

4.1.4.1 Relationship between momentum correlation and fringe visibility

In the conventional approach, measurements of transverse momentum correlations between two photons rely on coincidence detection, where individual detectors are utilized to resolve the transverse momentum of each photon [122, 16, 123, 24]. The transverse momenta are proportional to the transverse component of the wave vector for the signal and idler photons (q_s and q_i). In such traditional methods, by varying the positions of the detectors, one can determine the conditional probability distribution ($P(q_i|q_s)$) for detecting a photon with a specific momentum, under the condition that the momentum of the other photon is already known. The variance $\Delta^2(q_i|q_s)$ derived from this conditional probability distribution provides a quantitative measure of the momentum correlation strength of the photon pair [7].

However, with the QIUP setup (Fig. 4.4), we can measure the transverse momentum correlations between two photons while detecting only one of them by using induced coherence without induced emission [7]. As described earlier, the EMCCD camera collects the superposed signal photons (forward and backward generated – s1 and s2) while none of them ever interacted with the object. It has been shown in [7] that the detected intensity pattern is:

$$I(r_{q_s}) \propto P_s(q_s) \int P(q_i|q_s)(1 + \cos[\phi_i(q_i) + \phi_0])dq_i, \tag{4.12}$$

where, ϕ_0 – constant phase terms across the beam cross-section; $\phi_i(q_i)$ – phase acquired by the idler beam for different transverse components; $P(q_i|q_s) = P(q_i, q_s)/P_s(q_s)$ – the conditional probability density of detecting an idler photon with the transverse component of the wave vector, q_i given the signal photon's transverse component of wave vector as q_s.

The visibility of the interference pattern is determined by varying the phase (ϕ_0) and calculating $v(r_{q_s}) = [I_{\max}(r_{q_s}) - I_{\min}(r_{q_s})]/[I_{\max}(r_{q_s}) + I_{\min}(r_{q_s})]$, at each pixel. It can be inferred from Eq. 4.12 that, for a given $\phi_i(q_i)$, the visibility depends solely on the conditional probability density $P(q_i|q_s)$. Consequently, the measured visibility can be used to determine $\Delta^2(q_i|q_s)$.

The EMCCD camera, placed behind a lens system, captures the superposed signal beam (s1 and s2). Through the lens, modes of the signal beam with different transverse wave vectors, q_s are recorded at distinct positions on the camera. Idler beam (i1) with different transverse components accumulates distinct phase shifts, denoted as $\phi_i(q_i)$ resulting in a spatial modulation in the interference fringes of superposed signal beams (s1 and s2). When the detected signal photon and the undetected idler photon are perfectly correlated in momentum, i.e., $P(q_i|q_s) \propto \delta(q_i + q_s)$, from Eq.4.12, we see that the intensity at any point on the camera depends on the phase introduced on exactly one q_i. As a result, the interference visibility becomes 1. Conversely, when the momentum correlation is imperfect, meaning the two photons are not strongly correlated in their momenta, the detection of a signal photon at a particular point on the camera no longer precisely determines the momentum of its partner idler photon. Instead, the phase acquired by several q_i aids intensity modulation of the signal beam at one point on the EMCCD. This varies within a range determined by the momentum correlation – leading to reduced visibility of the observed interference fringes when the momentum correlation is weak. Our current method is slightly different from [7] and can be easily applied to position and momentum correlation measurements.

In the following section, we will experimentally demonstrate the momentum correlation between the detected and undetected photons and also describe that it can be a measure of the spatial resolution in our QIUP system.

4.1.4.2 Momentum correlation and spatial resolution in QIUP

In our QIUP experimental setup, the object (knife edge) is placed in the undetected beam, and its complex transmission coefficient manifests in the interference pattern [56, 124]. As mentioned before, the interference visibility is proportional to the absolute value of the transmission coefficient [119]. The amplitude and phase introduced by the object can be extracted from the interference pattern [56]. We show later that the observed transverse momentum correlation is connected to the imaging resolution – the momentum correlation playing a dominant role in determining spatial resolution. As a result, a stronger correlation would lead to a higher spatial resolution [124].

As depicted in Fig. 4.4, a knife edge placed at the Fourier plane of the crystal partially blocks the undetected beam. We arranged the setup in such a way that it does not produce any spatial fringes, such as circular or linear fringes. Instead, we observe only a single bright spot on the camera due to constructive interference, with the knife edge partially blocking it. All other parameters of the imaging system (distances, focal lengths, etc.) are consistent with those explained in Fig. 4.4 and section 4.1.4, including the distance between the object and the camera.

Our experimental investigation of resolution is centered on purely absorptive objects. In our imaging system, the magnification factor is 1. Since the object is also situated at the Fourier plane of the crystal, the undetected photon with a given transverse momentum reaches a unique point on the object plane. This means that when the momentum correlation is ideal, the interference pattern recorded at that point contains information about only one point on the object. For instance, when the transmission coefficient at a point is zero, the measured visibility at that point is also zero.

However, if the momentum correlation is imperfect, a single point on the camera no longer corresponds to just one point on the object. This is due to the momentum of undetected photons varying over a range when the detected photon is detected with a specific momentum. The range broadens as momentum correlation weakens. As a result, information from multiple points on the object appears at a single point on the camera, indicating that a weaker momentum correlation diminishes the spatial resolution.

As the camera captures the intensity variations of the detected beams while the interferometric phase, ϕ, is modulated by a piezo scan of mirror M_s, the corresponding changes in the interference patterns become visible. We recorded a total of 360 interference patterns for 6π phase variation, each associated with a distinct value of $\phi = \phi_1, \phi_2, ..., \phi_{360}$. One transverse momentum of the undetected photon corresponds to information about one point on the object. This information is subsequently captured by the camera, where a single pixel registers one transverse momentum of the detected photon. Consequently, by analyzing the recorded interference patterns on a pixel-by-pixel basis, information about each point on the object can be independently extracted.

The image is formed by modulating the spatially independent interferometer phase, ϕ as mentioned before. To assess the phase shifts and visibility of the interference observed on the camera, we apply sinusoidal fits to the intensity data for each pixel individually. In Fig. 4.8, we show some examples of pixel intensity variation with phase scan. These sinusoidal fits allow us to extract the amplitude and phase. From this, we calculate the visibility, $V = (I_{max} - I_{min})/(I_{max} + I_{min})$, corresponding to each pixel, where I_{max} = (offset + amplitude) and I_{min} = (offset - amplitude). The amplitude describes the maximum absolute variation from the sinusoidal function's

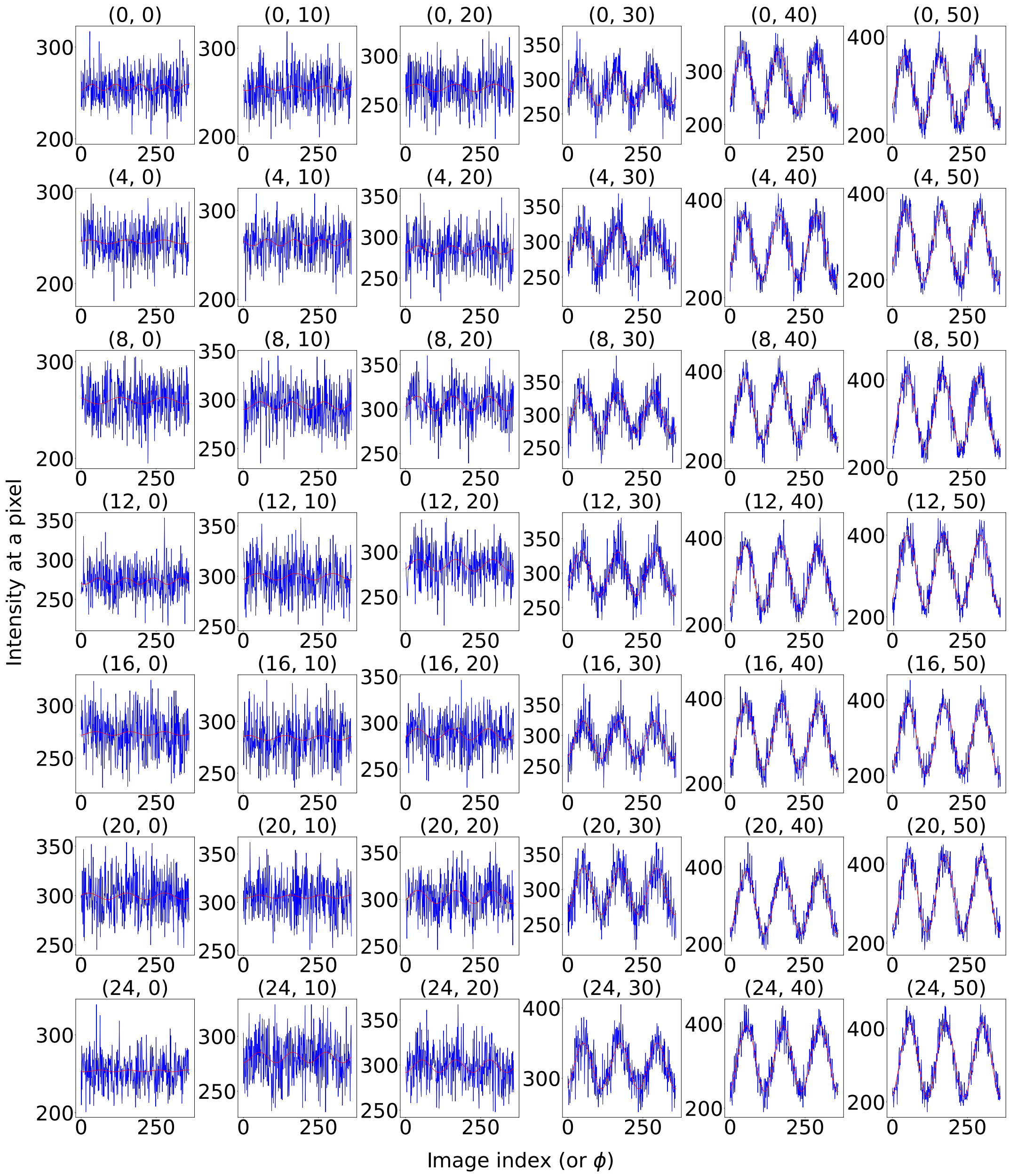

FIGURE 4.8: Illustration of the imaging process involving the EMCCD camera recording the detected beam intensity when the interferometric phase ϕ is varied – intensity changes as the phase is modified. By analyzing the recorded interference pattern pixel by pixel, independent information about each point on the object can be extracted. A sinusoidal function is fitted to the interference pattern obtained from each single pixel at different phases. This fitting process is exemplified for a few pixels. From the obtained fit, the visibility corresponding to each pixel is extracted.

mean value, spanning half the distance between its peak and trough. On the other hand, the offset provides a baseline or mean around which the function oscillates. Using these parameters, we form the visibility image of the knife edge, as depicted in Fig. 4.9.

Now to study the resolution of the imaging system, we evaluate a characteristic distance, σ from the visibility image of the knife edge – which can be considered as the edge-spread function (ESF) [124]. The knife edge that is placed parallel to the y-axis can be mathematically represented as:

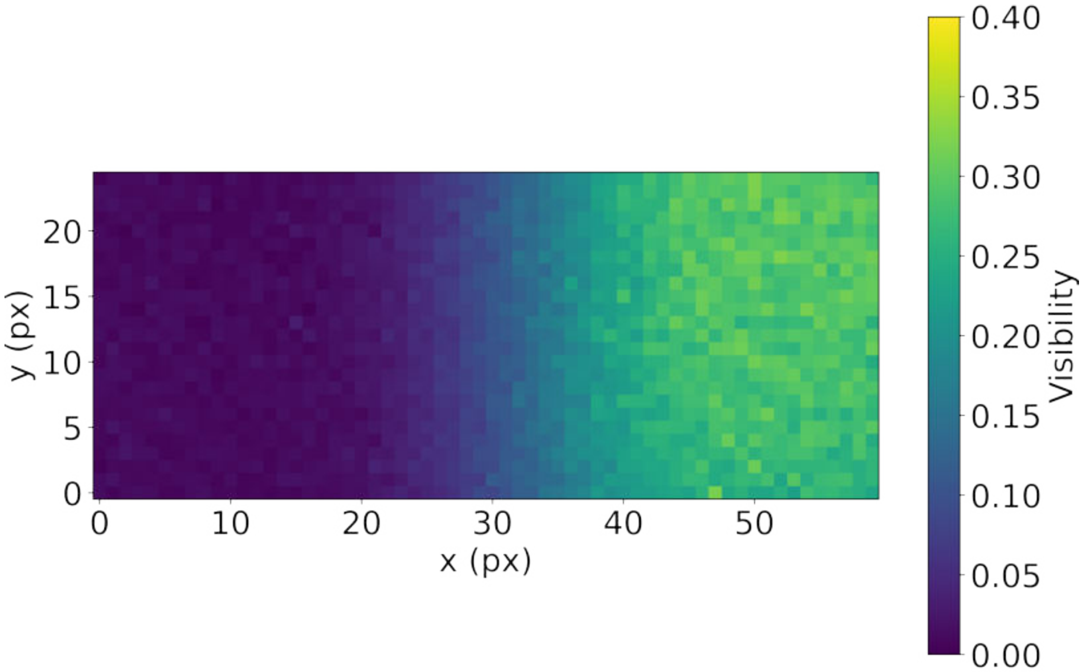

FIGURE 4.9: Experimental result for spatial resolution measurement. This figure represents the reconstructed visibility image of an absorptive sharp object (a knife edge).

$$T(x_0, y_0) = \begin{cases} 0, & \text{for } x_0 < x_0' \\ 1, & \text{for } x_0 \geq x_0' \end{cases} \tag{4.13}$$

We take a cross-section of the position-dependent visibility image and average over 20 rows, and fit it with the given function (ESF):

$$V(x) \propto 1 - \text{erf}[(x - M \times x_0')/\sigma], \tag{4.14}$$

where erf is the error function, and M is the magnification of the system and is defined by [56, 105, 124]:

$$M = \frac{f_c \lambda_d}{f_u \lambda_u}, \tag{4.15}$$

where f_c is the the focal length of the lens L_b placed before the EMCCD, f_u is the the focal length of the lens L_i in the undetected beam path, λ_d and λ_u are the wavelengths of both detected and undetected photons. In our experiment, wavelengths of both detected (λ_d) and undetected photons (λ_u) are 810 nm. Also, the focal length (f_u) of the lens L_i in the undetected beam path and the focal length (f_c) of the lens L_b placed before the EMCCD in our setup are the same (200 mm) – which gives the magnification, M of our system as 1.

Quantitatively, we assess the parameter σ as the characteristic distance on the camera plane, where the visibility increases from around 24% to 76% of its maximum achievable value. Fig. 4.10 illustrates the visibility cross-section, presenting the data points, error bars, and the fitted function. The measured value of σ using the described method is (352 ± 16.4) μm. To validate this result, we compare it with

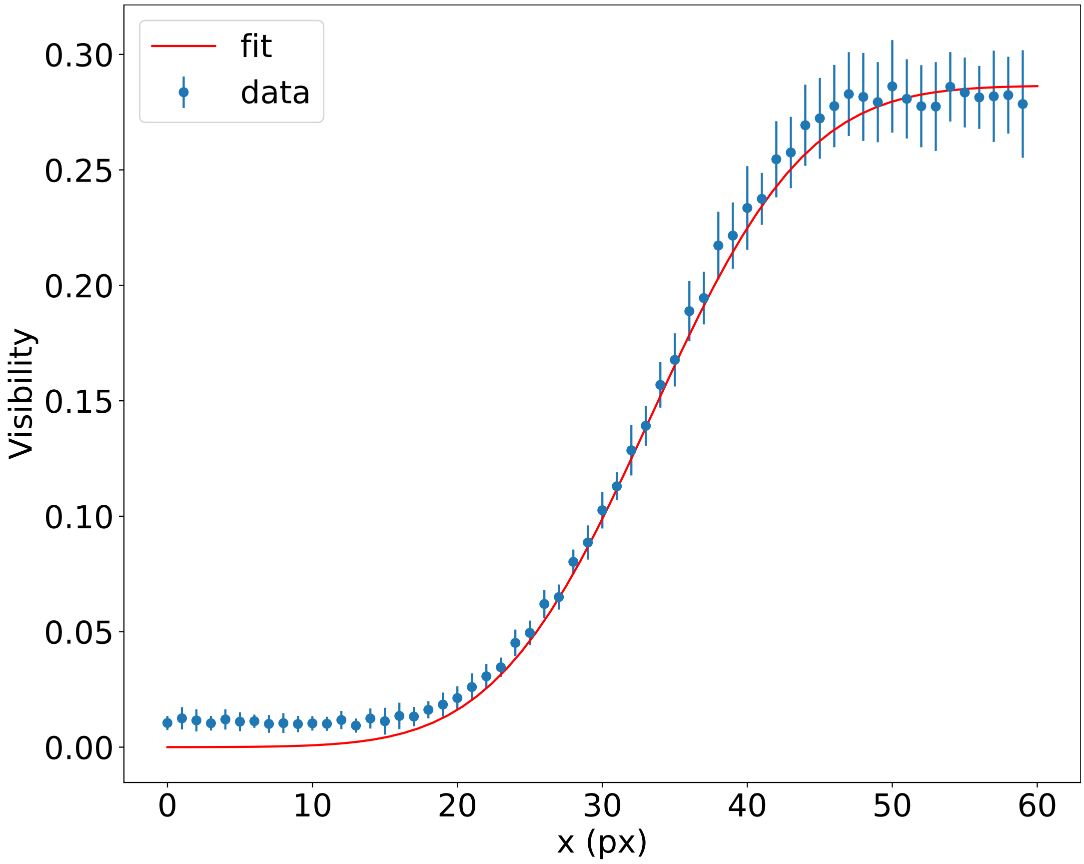

FIGURE 4.10: Experimental result for quantitative measurement of the spatial resolution, $\frac{\sigma}{M}$. This plot shows a cross-section of the reconstructed visibility image of a sharp edge object from Fig. 4.9 – averaged over 20 rows. We fit the data with an error function and measure the characteristic distance σ for which the value of visibility rises from 24% to 76%.

the value obtained from the formula for σ given in the reference [124]:

$$\sigma = \frac{f_c \lambda_d}{\sqrt{2}\pi w_p}. \tag{4.16}$$

From the experiment, we find that the measured pump waist at the crystal plane is approximately 108 μm, which yields a calculated value of σ to be 337 μm. This shows a good agreement with the measured σ.

Observing Fig. 4.10, we can notice that the visibilities at the pixels obstructed by the knife edge register slightly above zero. This occurrence is a result of the fitting process, where intensity variations are analyzed with a sinusoidal function during the phase scan (Fig. 4.8). The presence of noise in the fitting procedure leads to visibility values that exceed zero.

It is essential to emphasize that σ alone does not directly measure spatial resolution. While σ represents a distance measured on the camera, spatial resolution pertains to the minimum resolvable distance at the object. To quantify spatial resolution, we divide σ by the magnification factor M, as shown in Eq. 4.17, which derives from combining Eq. 4.16 and Eq. 4.15.

$$\frac{\sigma}{M} = \frac{f_u \lambda_u}{\sqrt{2}\pi w_p}. \tag{4.17}$$

This expression reveals that the measured spatial resolution value depends on the wavelength of the undetected photon. Although our system employs photons with the same wavelength for both detected and undetected photons, achieving a shorter wavelength for the illuminating light (undetected light) can substantially improve the resolution. This emphasizes the significance of the undetected photon's wavelength in optimizing spatial resolution.

Additionally, in the context of SPDC, spatial correlation theory and considering a Gaussian pump beam with a waist of w_p, the conditional probability governing the momentum correlation between detected (signal) and undetected (idler) photons is described as [125]:

$$P(q_i|q_s) \propto \exp\left(-|q_s+q_i|^2\frac{w_p^2}{2}\right) \simeq \exp\left(-|q_p|^2\frac{w_p^2}{2}\right), \tag{4.18}$$

In this equation, q_p represents the transverse component of the pump wave vector. Notably, a larger pump beam waist (w_p) leads to a more significant correlation between the signal and idler photons. As a result, the spatial resolution improves, as shown in Eq. 4.17. Thus, the size of the pump beam waist plays a crucial role in enhancing the imaging system's ability to resolve finer details. Therefore, σ is a direct measure of the transverse momentum correlation between the signal and the idler.

Note that in the method described above using a knife edge for measuring momentum correlation between downconverted photon pairs by detecting only one of them can be more faster by using phase-shifting digital holography [126, 127]. In such a case we only need to record four images (with global phases $\Delta\phi = 0, \pi/2, \pi, 3\pi/2$) and from these four frames only we could extract the information of the object (σ in our case as well) – which will lead to measuring the momentum correlation of photon pairs in a much simpler and straightforward way. Phase-shifting holography method with a knife edge is different and simpler than the method described in [7].

4.2 Investigating OAM modes of photon pairs in the nonlinear interferometric setup

We extended the characterization of the transverse momenta correlation of signal and idler photons to a discrete degree of freedom – the orbital angular momentum (OAM) of light.

Orbital angular momentum (OAM) in light beams is associated with a spiral phase structure in the transverse plane, defined as $e^{il\phi}$, where l represents the winding number, and ϕ is the azimuthal angle. Due to the inherent periodicity of phse, only those OAM states with integer values of l form a complete orthogonal basis in the Hilbert space. Although this space is in principle infinite-dimensional, in practice, only specific subsets can be accessed experimentally.

When discussing spontaneous parametric down-conversion (SPDC), the bi-photon states produced are characterized by a number of OAM modes with non-negligible contribution, commonly denoted as the spiral bandwidth [128, 129]. The spiral bandwidth plays a crucial role in dictating the entanglement properties and the possible quantum states the photons can occupy. The spiral bandwidth defines the range of OAM modes that are generated in the SPDC process. Each distinct OAM mode (characterized by a different winding number l) represents a possible state in which the photon can be found. So, if the spiral bandwidth encompasses N distinct

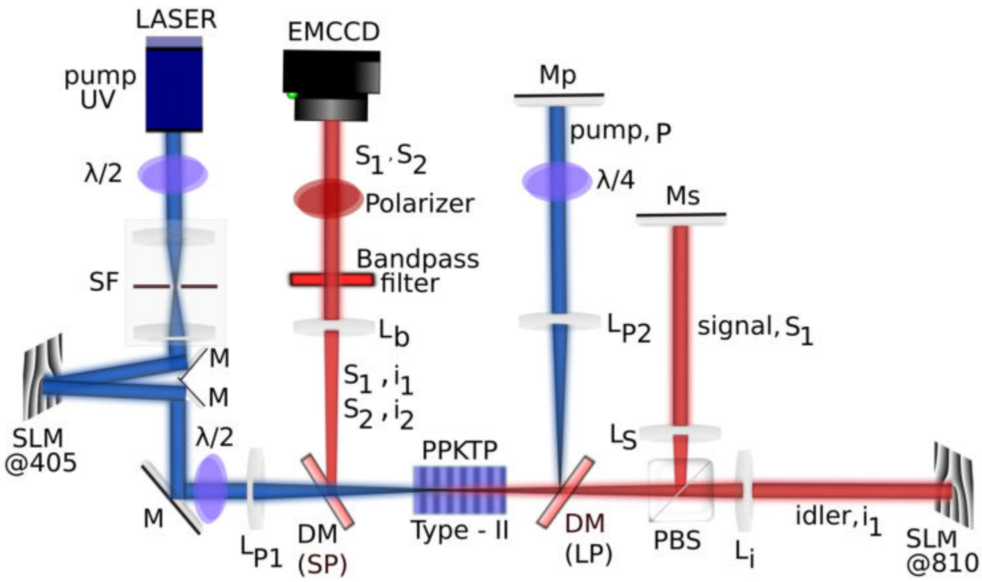

FIGURE 4.11: Experimental setup for OAM entanglement certification. This is a slightly modified version of the setup described in Fig. 4.4. Here we have two spatial light modulators (SLM) – one for the 405 nm pump laser, and another one for 810 nm SPDC light. For now we keep the pump beam as Gaussian (i.e., $l = 0$ for the pump) and use the SLM instead of the mirror M_i, to imprint higher-order OAM modes to the idler photons (i1 beam) generated in the first pass of the pump beam through the crystal. Without coincidence detection, we only detect interference fringes of the signal photons, s1 and s2. Due to the induced coherence, we can see spiral fringes.

OAM modes, this means that the entangled photon pair can exist in a superposition of these N modes. To illustrate, if the spiral bandwidth includes OAM modes from $l = -1$ to $l = +1$, then there are three possible modes, and the entangled pair can be described by a superposition of these three states. Furthermore, the extent of this bandwidth is not arbitrary. It is influenced by various factors, including the pump's waist, the phase-matching conditions, and the modes chosen for detection.

A photon carrying a phase structure dependent on the azimuthal angle, symbolized as $e^{il\phi}$, possesses an OAM quantified as $l\hbar$. Notably, the OAM state space is both discrete and infinite-dimensional.

We investigate OAM modes of signal-idler pair in such a nonlinear interferometer by building a slightly modified version of the setup shown in Fig. 4.4. In this setup (Fig. 4.11), in the idler beam path of the interferometer, a spatial light modulator (SLM) is used instead of the mirror M_i, where we spatially modulate (imprinting the phase corresponding to higher-order OAM modes, l) the idler photons generated in the first pass of the pump through the crystal (i1). Without coincidence detection, we only detect interference fringes of the signal photons (s1 and s2). Induced coherence allows the modulation imposed on i1 to be observed in the signal fringes. This has future implications for certifying OAM entanglement in the SPDC process. The interference visibility of the signal photons in the interferometer offers indirect insights into the OAM modes and spiral bandwidth. Using the SLM, we imprint extra OAM modes, l, onto the i1 beam. Subsequently, we record the interference fringes of signals, s1, and s2, as shown in Fig. 4.12.

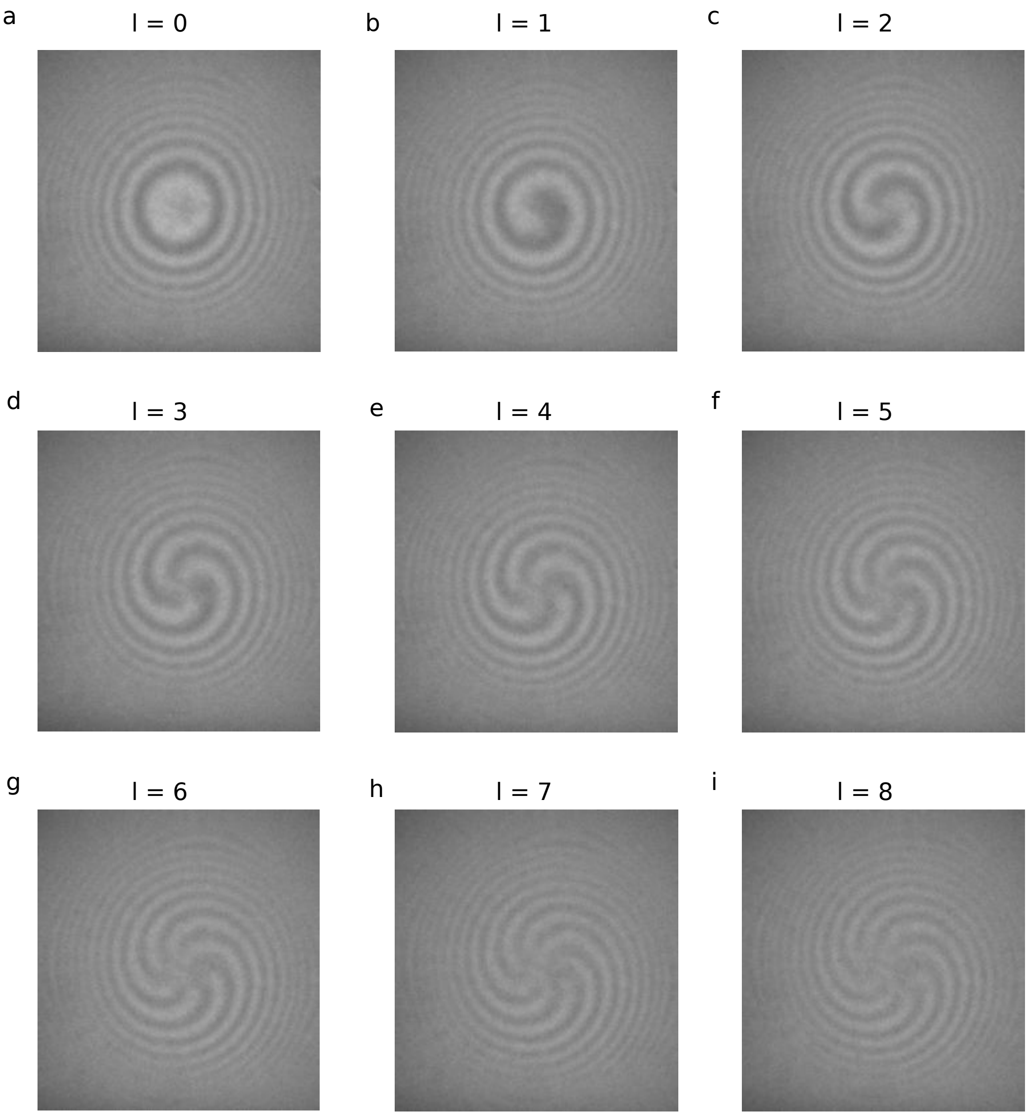

FIGURE 4.12: Experimental results of spatially dependent interference fringes of signal photons (s1 and s2) in QIUP setup while adding extra OAM, l modes to the forward going idler (i1) – from $l = 0$ to $l = 8$. Spiral fringes are due to some residual quadratic phase along with added extra l-values **(a–i)**. We see that with increasing l, the visibility of the fringes drops.

In the context of the OAM basis, entanglement implies that the OAM state of the idler photon is correlated with that of the signal photon. A maximally entangled state signifies that any modification in the OAM state of the idler photon results in a related change in the OAM state of the signal photon [130]. When increasing l values are added to the idler (i1), and there's a drop in interference visibility, it suggests that the OAM modes of the signal photons are affected in such a way that they no longer overlap well – that is the introduced OAM modes might be beyond the spiral bandwidth determined by the phase-matching conditions. Nonetheless, the observation of interference fringes at higher l values indicates persistent entanglement across several OAM states, pointing to multi-dimensional entanglement.

Notably, the addition of an SLM to the QIUP setup could enhance the applicability of our experiment which includes complex phase imaging and digital holography (for instance, phase stepping or off-axis holography) [127].

4.3 Conclusions

The main aspect of our investigation was measuring the momentum correlation between the signal and idler photons without relying on coincidence detection. This method also enabled us to measure spatial resolution in QIUP. One noteworthy outcome of our experiment was the demonstration that a known object can be used to deduce the properties of photon pairs. This approach allowed us to obtain information about one photon by solely detecting its partner and offering perspectives on photon pair-based imaging. Additionally, our investigation can be extended to measuring position correlation alongside momentum correlation, leading to insights into EPR-type correlations between the signal and idler without relying on coincidence detection for certifying position-momentum type entanglement.

In summary, we explored the role of spatial correlation in non-linear interferometers and imaging with undetected photons. We aimed to characterize the spatial resolution of the system, where both the object and camera were situated in the far field of the photon-pair source, a nonlinear crystal.

We could also extend our method to the discrete degrees of freedom to certify high-dimensional (OAM) entanglement. This work could also lead to an impact on the field of twisted photons, and high-dimensional quantum information [131, 83].

The project about EPR-type correlation for position-momentum entanglement measurement between the signal and idler without relying on coincidence detection is in collaboration with Prof. Mayukh Lahiri, and Balakrishnan Viswanathan from Oklahoma State University for theory and Prof. Gabriela Barreto Lemos from Federal University of Rio de Janeiro for experimental ideas and discussions. I built the setup in the Quantum Imaging Lab at the University of Warsaw to do the aforementioned experiment. In total in Warsaw, I built two setups of the nonlinear interferometer. Additionally, I built another modified version of the setup in the Experimental Quantum Optics group at Tampere University led by Prof. Robert Fickler for the collaborative project on high-dimensional quantum entanglement.

Chapter 5

Conclusions and outlook

5.1 Thesis summary

In summary, this thesis presented methodologies to characterize the spatial properties of single and entangled photon pairs. These methodologies arise from three distinct experiments and can find applications in the fields of quantum communication, quantum imaging, and entanglement research.

The first experiment introduced a self-referenced interferometric technique to reconstruct both the spatial phase and amplitude profile of photons from a single photon source with an unknown spatial profile. Inspired by the classical holography technique, our approach eliminates the need for a reference photon by utilizing the phenomenon of single-photon interfering with itself. This way our method offers both robustness and simplicity. We utilize a heralded single-photon source with an unknown spatial phase, in conjunction with a modified Mach-Zehnder interferometer with a spatial filter in one of its arms. The spatial filter flattens the unknown spatial phase and the filtered beam interferes with the unfiltered beam passing through the other arm of the interferometer. From the lowest-order interference fringes, we quantitatively reconstruct the unknown phase of the single photon beam. The single-pixel uncertainties of the reconstructed 2D phases are measured. For the 2D quadratic phase object, the uncertainty is below $\frac{2\pi}{30}$. The spiral phase object has an uncertainty below $\frac{2\pi}{50}$. The 1D quadratic phase object also has an uncertainty below $\frac{2\pi}{50}$. All these uncertainties are observed in a region with a radius of 50 pixels, which has maximum visibility and photon count rate. This ensures high-resolution phase reconstruction. By avoiding measurements of a two-photon probability distribution, our technique does not require coincidence detection, making it simpler and more tolerant to losses. This method's flexibility is evident as it can characterize any single photon beam with an unknown pure spatial state, including those with orbital angular momentum modes. This study's results are relevant for quantum communication and imaging.

In the second experiment, we characterize momentum correlations of photon pairs generated in type-I spontaneous parametric down-conversion process by utilizing a custom-built adaptively-gated hybrid intensified camera (HIC). This HIC combines sCMOS sensor and a high temporal resolution detector, PMT with an adaptively-gated image intensifier, facilitating spatially resolved single-photon counting. A notable feature is its increased data acquisition speed compared to standard non-adaptive methods. Using a fast feedback loop based on FPGA, our method achieves real-time photon counting, allowing immediate adjustment of acquisition time after photon detection. This configuration enables control over the number of photons detected within each frame. For this study, correlations were obtained for about 190 spatial modes on the momentum basis. With a spatial resolution of nearly 9 megapixels and nanosecond temporal resolution, this HIC setup fills a gap between the temporal resolution of time-tagging SPAD arrays and the spatial capabilities of intensified cameras, with potential applications in quantum imaging and related fields.

The third experiment focused on measuring the spatial correlation of down-converted photon pairs in non-linear interferometers without using coincidence detection, unlike the traditional methods where the transverse momentum correlation between two photons is measured by the coincident detection of both photons by scanning the relative positions of two individual detectors that resolve the transverse momentum of the respective photon. We used a technique called quantum imaging with undetected photons (QIUP) [56, 105] based on the phenomenon of induced coherence without induced emission [45]. QIUP is an imaging technique where one can reconstruct the properties of an object to be imaged without ever detecting the photons that interact with it. Instead, it is rooted in the generation of entangled photon pairs in a quantum superposition, originating from two distinct, spatially separated SPDC sources. In this process, one photon from the SPDC pair (idler photon), interacts with the object under investigation and is never detected. We show how this information can be used to obtain spatial correlation measurements of the photon pairs. Therefore, our setup facilitates the analysis of correlations of down-converted photon pairs without relying on coincidence measurements. This is enabled by the fact that the spatial resolution of QIUP is limited by the strength of momentum correlations. A stronger correlation leads to a higher resolution and vice versa. We can further employ this interferometric technique for position-momentum entanglement verification by measuring EPR type correlation [17, 18] and also explore possibilities of certifying high-dimensional entanglement (OAM).

5.2 Outlook

5.2.1 Self-referenced interferometric technique:

The ability to reconstruct spatial phase and amplitude profiles of single photon beams can be instrumental in enhancing the reliability and efficiency of quantum communication systems. Given its versatility in characterizing various photon beams, this technique can potentially improve the accuracy of quantum imaging methods. The technique's adaptability to both one and two-dimensional phase reconstruction and other complex states, like orbital angular momentum modes [76], suggests it could be valuable in broader quantum state characterization endeavors. Additionally, this technique can also find its applicability in matter-wave interferometry [78, 79]. It could also be interesting to extend our method to characterize mixed or entangled states [80].

5.2.1.1 Hybrid intensified camera (HIC):

The HIC's unique combination of spatial and temporal resolution makes it a versatile tool for quantum imaging applications. The capability of the HIC to adaptively control image intensification can speed up the photon detection process. The increased speed in data collection makes the HIC a valuable tool for quantum optical experiments that require statistically significant data in short time frames. This HIC setup provides a multi-megapixel resolution, which is currently unachievable with the time-tagging SPAD arrays and it overcomes the challenges faced by conventional intensified cameras by adding a fast feedback loop. This leads to its functionality in fundamental quantum information science as well as other applications, for instance, quantum imaging [84, 99], quantum walks of correlated photons [100, 101], Boson sampling [104], and studies of quantum correlations in scattering media [102, 103].

5.2.1.2 Spatial Correlation in Non-linear Interferometers:

This experiment highlights the ability to utilize a known object to infer properties of photon pairs, presenting a new direction in quantum imaging. This method becomes especially valuable in situations where it's challenging to observe both photons simultaneously. Furthermore, the results offer insights into investigating EPR-type correlations, setting the stage for advanced entanglement studies, including those in high-dimensional systems.

This methodology can potentially be extended to other degrees of freedom, such as spectral degrees. In [132], it has shown that imaging resolution depends on the wavelengths involved. This could lead to applications in the mid-infrared range, where images can be captured using standard near-IR cameras. Additional research has been done on detecting the infrared absorption lines of carbon dioxide molecules using visible light [118].

In the context of imaging resolution, the limit is actually determined by the wavelength of the undetected light passing through the object. This suggests that it may be possible to achieve a resolution defined by a wavelength shorter than that of the detected light [124]. Lastly, it's worth noting the differences between QIUP and ghost imaging. Specifically, QIUP doesn't require coincidence measurements and, unlike ghost imaging, cannot be explained by classical theories [56, 105].

Bibliography

[1] Leonard Mandel and Emil Wolf. *Optical Coherence and Quantum Optics*. New York: Cambridge University Press, 1995.

[2] D.N. Klyshko. *Photons and Non-Linear Optics*. New York: Gordon and Breach Science Publishers, 1988.

[3] Z.Y.J. Ou. *Multi-Photon Quantum Interference*. New York: Springer, 2007.

[4] Robert W. Boyd. *Nonlinear Optics*. 3rd. Academic Press, Elsevier, 2008.

[5] Wiktor Szadowiak, Sanjukta Kundu, Jerzy Szuniewicz, and Radek Lapkiewicz. "Self-referenced hologram of a single photon beam". In: *Quantum* 5 (Aug. 2021), p. 516. DOI: 10.22331/q-2021-08-03-516. URL: https://doi.org/10.22331/q-2021-08-03-516.

[6] Sanjukta Kundu, Jerzy Szuniewicz, Grzegorz Firlik, Alexander Krupinski-Ptaszek, and Radek Lapkiewicz. *High-dimensional quantum correlation measurements with an adaptively gated hybrid single-photon camera*. 2023. DOI: 10.48550/ARXIV.2305.16245. URL: https://arxiv.org/abs/2305.16245.

[7] Armin Hochrainer, Mayukh Lahiri, Radek Lapkiewicz, Gabriela Barreto Lemos, and Anton Zeilinger. "Quantifying the momentum correlation between two light beams by detecting one". In: *Proceedings of the National Academy of Sciences* 114.7 (Jan. 2017), pp. 1508–1511. DOI: 10.1073/pnas.1620979114. URL: https://doi.org/10.1073/pnas.1620979114.

[8] S.P. Walborn, C.H. Monken, S. Pádua, and P.H. Souto Ribeiro. "Spatial correlations in parametric down-conversion". In: *Physics Reports* 495.4-5 (Oct. 2010), pp. 87–139. DOI: 10.1016/j.physrep.2010.06.003. URL: https://doi.org/10.1016/j.physrep.2010.06.003.

[9] Lijun Wang. "Investigation of induced coherence with and without induced emission". 9231327. PhD thesis. Rochester: University of Rochester, 1992.

[10] A. K. Jha. "Coherence properties of the entangled two-photon field produced by parametric down conversion". PhD thesis. University of Rochester, 2009.

[11] D. N. Klyshko and D. P. Krindach. "Parametric Luminescence of Lithium Niobate". In: *Optics and Spectroscopy* 26 (1969), p. 532.

[12] B. Ya. Zel'Dovich and D. N. Klyshko. "Field Statistics in Parametric Luminescence". In: *Journal of Experimental and Theoretical Physics Letters* 9 (1969), p. 40.

[13] C. K. Hong and L. Mandel. "Theory of parametric frequency down conversion of light". In: *Phys. Rev. A* 31 (4 1985), pp. 2409–2418. DOI: 10.1103/PhysRevA.31.2409. URL: https://link.aps.org/doi/10.1103/PhysRevA.31.2409.

[14] Jonathan Leach, Miles J. Padgett, Stephen M. Barnett, Sonja Franke-Arnold, and Johannes Courtial. "Measuring the Orbital Angular Momentum of a Single Photon". In: *Phys. Rev. Lett.* 88 (25 2002), p. 257901. DOI: 10.1103/PhysRevLett.88.257901. URL: https://link.aps.org/doi/10.1103/PhysRevLett.88.257901.

[15] Haiqing Wei, Xin Xue, Jonathan Leach, Miles J. Padgett, Stephen M. Barnett, Sonja Franke-Arnold, Eric Yao, and Johannes Courtial. "Simplified measurement of the orbital angular momentum of single photons". In: *Optics Communications* 223.1-3 (July 2003), pp. 117–122. DOI: 10.1016/s0030-4018(03)01619-5. URL: https://doi.org/10.1016/s0030-4018(03)01619-5.

[16] John C. Howell, Ryan S. Bennink, Sean J. Bentley, and R. W. Boyd. "Realization of the Einstein-Podolsky-Rosen Paradox Using Momentum- and Position-Entangled Photons from Spontaneous Parametric Down Conversion". In: *Physical Review Letters* 92.21 (May 2004). DOI: 10.1103/physrevlett.92.210403. URL: https://doi.org/10.1103/physrevlett.92.210403.

[17] A. Einstein, B. Podolsky, and N. Rosen. "Can Quantum-Mechanical Description of Physical Reality Be Considered Complete?" In: *Phys. Rev.* 47 (10 1935), pp. 777–780. DOI: 10.1103/PhysRev.47.777. URL: https://link.aps.org/doi/10.1103/PhysRev.47.777.

[18] Gregg Jaeger. *Quantum Objects: Non-Local Correlation, Causality and Objective Indefiniteness in the Quantum World*. Springer, 2014. DOI: 10.1007/978-3-642-37629-0.

[19] D. S. Tasca, S. P. Walborn, P. H. Souto Ribeiro, F. Toscano, and P. Pellat-Finet. "Propagation of transverse intensity correlations of a two-photon state". In: *Physical Review A* 79.3 (Mar. 2009). DOI: 10.1103/physreva.79.033801. URL: https://doi.org/10.1103/physreva.79.033801.

[20] M. D. Reid and P. D. Drummond. "Quantum Correlations of Phase in Nondegenerate Parametric Oscillation". In: *Phys. Rev. Lett.* 60 (26 1988), pp. 2731–2733. DOI: 10.1103/PhysRevLett.60.2731. URL: https://link.aps.org/doi/10.1103/PhysRevLett.60.2731.

[21] M. D. Reid, P. D. Drummond, W. P. Bowen, E. G. Cavalcanti, P. K. Lam, H. A. Bachor, U. L. Andersen, and G. Leuchs. "Colloquium: The Einstein-Podolsky-Rosen paradox: From concepts to applications". In: *Rev. Mod. Phys.* 81 (4 2009), pp. 1727–1751. DOI: 10.1103/RevModPhys.81.1727. URL: https://link.aps.org/doi/10.1103/RevModPhys.81.1727.

[22] S. P. Walborn, A. Salles, R. M. Gomes, F. Toscano, and P. H. Souto Ribeiro. "Revealing Hidden Einstein-Podolsky-Rosen Nonlocality". In: *Phys. Rev. Lett.* 106 (13 2011), p. 130402. DOI: 10.1103/PhysRevLett.106.130402. URL: https://link.aps.org/doi/10.1103/PhysRevLett.106.130402.

[23] Olivier Daigle, Claude Carignan, Jean-Luc Gach, Christian Guillaume, Simon Lessard, Charles-Anthony Fortin, and Sébastien Blais-Ouellette. "Extreme Faint Flux Imaging with an EMCCD". In: *Publications of the Astronomical Society of the Pacific* 121.882 (Aug. 2009), pp. 866–884. DOI: 10.1086/605449. URL: https://doi.org/10.1086/605449.

[24] M.P. Edgar, D.S. Tasca, F. Izdebski, R.E. Warburton, J. Leach, M. Agnew, G.S. Buller, R.W. Boyd, and M.J. Padgett. "Imaging high-dimensional spatial entanglement with a camera". In: *Nature Communications* 3.1 (Jan. 2012). DOI: 10.1038/ncomms1988. URL: https://doi.org/10.1038/ncomms1988.

[25] Reuben S Aspden, Daniel S Tasca, Robert W Boyd, and Miles J Padgett. "EPR-based ghost imaging using a single-photon-sensitive camera". In: *New Journal of Physics* 15.7 (July 2013), p. 073032. DOI: 10.1088/1367-2630/15/7/073032. URL: https://doi.org/10.1088/1367-2630/15/7/073032.

[26] Robert Fickler, Mario Krenn, Radek Lapkiewicz, Sven Ramelow, and Anton Zeilinger. "Real-Time Imaging of Quantum Entanglement". In: *Scientific Reports* 3.1 (May 2013). DOI: 10.1038/srep01914. URL: https://doi.org/10.1038/srep01914.

[27] C. K. Law and J. H. Eberly. "Analysis and Interpretation of High Transverse Entanglement in Optical Parametric Down Conversion". In: *Phys. Rev. Lett.* 92 (12 2004), p. 127903. DOI: 10.1103/PhysRevLett.92.127903. URL: https://link.aps.org/doi/10.1103/PhysRevLett.92.127903.

[28] C. H. Monken, P. H. Souto Ribeiro, and S. Pádua. "Transfer of angular spectrum and image formation in spontaneous parametric down-conversion". In: *Physical Review A* 57.4 (Apr. 1998), pp. 3123–3126. DOI: 10.1103/physreva.57.3123. URL: https://doi.org/10.1103/physreva.57.3123.

[29] Radosław Chrapkiewicz, Wojciech Wasilewski, and Konrad Banaszek. "High-fidelity spatially resolved multiphoton counting for quantum imaging applications". In: *Opt. Lett.* 39.17 (2014), pp. 5090–5093. DOI: 10.1364/OL.39.005090. URL: http://opg.optica.org/ol/abstract.cfm?URI=ol-39-17-5090.

[30] Michał Dąbrowski, Mateusz Mazelanik, Michał Parniak, Adam Leszczyński, Michał Lipka, and Wojciech Wasilewski. "Certification of high-dimensional entanglement and Einstein-Podolsky-Rosen steering with cold atomic quantum memory". In: *Physical Review A* 98.4 (Oct. 2018). DOI: 10.1103/physreva.98.042126. URL: https://doi.org/10.1103/physreva.98.042126.

[31] Michał Dąbrowski, Michał Parniak, and Wojciech Wasilewski. "Einstein–Podolsky–Rosen paradox in a hybrid bipartite system". In: *Optica* 4.2 (Feb. 2017), p. 272. DOI: 10.1364/optica.4.000272. URL: https://doi.org/10.1364/optica.4.000272.

[32] Andrei Nomerotski, Michael Keach, Paul Stankus, Peter Svihra, and Stephen Vintskevich. "Counting of Hong-Ou-Mandel Bunched Optical Photons Using a Fast Pixel Camera". In: *Sensors* 20.12 (June 2020), p. 3475. DOI: 10.3390/s20123475. URL: https://doi.org/10.3390/s20123475.

[33] Christopher Ianzano, Peter Svihra, Mael Flament, Andrew Hardy, Guodong Cui, Andrei Nomerotski, and Eden Figueroa. "Fast camera spatial characterization of photonic polarization entanglement". In: *Scientific Reports* 10.1 (Apr. 2020). DOI: 10.1038/s41598-020-62020-z. URL: https://doi.org/10.1038/s41598-020-62020-z.

[34] A. Nomerotski, M. Chekhlov, D. Dolzhenko, R. Glazenborg, B. Farella, M. Keach, R. Mahon, D. Orlov, and P. Svihra. "Intensified Tpx3Cam, a fast data-driven optical camera with nanosecond timing resolution for single photon detection in quantum applications". In: *Journal of Instrumentation* 18.01 (Jan. 2023), p. C01023. DOI: 10.1088/1748-0221/18/01/c01023. URL: https://doi.org/10.1088/1748-0221/18/01/c01023.

[35] Baptiste Courme, Chloé Vernière, Peter Svihra, Sylvain Gigan, Andrei Nomerotski, and Hugo Defienne. "Quantifying high-dimensional spatial entanglement with a single-photon-sensitive time-stamping camera". In: *Opt. Lett.* 48.13 (2023), pp. 3439–3442. DOI: 10.1364/OL.487182. URL: https://opg.optica.org/ol/abstract.cfm?URI=ol-48-13-3439.

[36] A. Rochas, M. Gani, B. Furrer, P. A. Besse, R. S. Popovic, G. Ribordy, and N. Gisin. "Single photon detector fabricated in a complementary metal–oxide–semiconductor high-voltage technology". In: *Review of Scientific Instruments* 74.7 (June 2003), pp. 3263–3270. DOI: 10.1063/1.1584083. URL: https://doi.org/10.1063/1.1584083.

[37] Claudio Bruschini, Harald Homulle, Ivan Michel Antolovic, Samuel Burri, and Edoardo Charbon. "Single-photon avalanche diode imagers in biophotonics: review and outlook". In: *Light: Science & Applications* 8.1 (Sept. 2019). DOI: 10.1038/s41377-019-0191-5. URL: https://doi.org/10.1038/s41377-019-0191-5.

[38] Kazuhiro Morimoto, Andrei Ardelean, Ming-Lo Wu, Arin Can Ulku, Ivan Michel Antolovic, Claudio Bruschini, and Edoardo Charbon. "Megapixel time-gated SPAD image sensor for 2D and 3D imaging applications". In: *Optica* 7.4 (2020), pp. 346–354. DOI: 10.1364/OPTICA.386574. URL: http://opg.optica.org/optica/abstract.cfm?URI=optica-7-4-346.

[39] Bienvenu Ndagano, Hugo Defienne, Ashley Lyons, Ilya Starshynov, Federica Villa, Simone Tisa, and Daniele Faccio. "Imaging and certifying high-dimensional entanglement with a single-photon avalanche diode camera". In: *npj Quantum Information* 6.1 (Dec. 2020). DOI: 10.1038/s41534-020-00324-8. URL: https://doi.org/10.1038/s41534-020-00324-8.

[40] Radosław Chrapkiewicz. "Generation and characterization of spatially structured few-photon states of light". Ph.D. Thesis. University of Warsaw, Feb. 2016. URL: https://depotuw.ceon.pl/handle/item/1415.

[41] Matthew Reichert, Hugo Defienne, and Jason W. Fleischer. "Massively Parallel Coincidence Counting of High-Dimensional Entangled States". In: *Scientific Reports* 8.1 (May 2018). DOI: 10.1038/s41598-018-26144-7. URL: https://doi.org/10.1038/s41598-018-26144-7.

[42] Robert H. Hadfield. "Single-photon detectors for optical quantum information applications". In: *Nature Photonics* 3.12 (Dec. 2009), pp. 696–705. DOI: 10.1038/nphoton.2009.230. URL: https://doi.org/10.1038/nphoton.2009.230.

[43] Richard P. Feynman, Robert B. Leighton, and Matthew Sands. *Quantum Mechanics: The Feynman Lectures on Physics, Vol. 3*. Reading, MA: Addison-Wesley, 1965.

[44] C. K. Hong, Z. Y. Ou, and L. Mandel. "Measurement of subpicosecond time intervals between two photons by interference". In: *Phys. Rev. Lett.* 59 (18 1987), pp. 2044–2046. DOI: 10.1103/PhysRevLett.59.2044. URL: https://link.aps.org/doi/10.1103/PhysRevLett.59.2044.

[45] X. Y. Zou, L. J. Wang, and L. Mandel. "Induced coherence and indistinguishability in optical interference". In: *Physical Review Letters* 67.3 (July 1991), pp. 318–321. DOI: 10.1103/physrevlett.67.318. URL: https://doi.org/10.1103/physrevlett.67.318.

[46] T. J. Herzog, J. G. Rarity, H. Weinfurter, and A. Zeilinger. "Frustrated two-photon creation via interference". In: *Physical Review Letters* 72.5 (Jan. 1994), pp. 629–632. DOI: 10.1103/physrevlett.72.629. URL: https://doi.org/10.1103/physrevlett.72.629.

[47] Marlan O. Scully and M. Suhail Zubairy. *Quantum Optics*. Cambridge: Cambridge University Press, 1997. ISBN: 1139643061, 9781139643061.

[48] Mohammad Mirhosseini, Mehul Malik, Zhimin Shi, and Robert W. Boyd. "Efficient separation of the orbital angular momentum eigenstates of light". In: *Nature Communications* 4.1 (Nov. 2013). DOI: 10.1038/ncomms3781. URL: https://doi.org/10.1038/ncomms3781.

[49] S. P. Walborn, D. S. Lemelle, M. P. Almeida, and P. H. Souto Ribeiro. "Quantum Key Distribution with Higher-Order Alphabets Using Spatially Encoded Qudits". In: *Physical Review Letters* 96.9 (Mar. 2006). DOI: 10.1103/physrevlett.96.090501. URL: https://doi.org/10.1103/physrevlett.96.090501.

[50] S. F. Pereira, Z. Y. Ou, and H. J. Kimble. "Quantum communication with correlated nonclassical states". In: *Physical Review A* 62.4 (Sept. 2000). DOI: 10.1103/physreva.62.042311. URL: https://doi.org/10.1103/physreva.62.042311.

[51] Robert Fickler, Radek Lapkiewicz, Marcus Huber, Martin P.J. Lavery, Miles J. Padgett, and Anton Zeilinger. "Interface between path and orbital angular momentum entanglement for high-dimensional photonic quantum information". In: *Nature Communications* 5.1 (July 2014). DOI: 10.1038/ncomms5502. URL: https://doi.org/10.1038/ncomms5502.

[52] M. Aspelmeyer, T. Jennewein, M. Pfennigbauer, W.R. Leeb, and A. Zeilinger. "Long-distance quantum communication with entangled photons using satellites". In: *IEEE Journal of Selected Topics in Quantum Electronics* 9.6 (Nov. 2003), pp. 1541–1551. DOI: 10.1109/jstqe.2003.820918. URL: https://doi.org/10.1109/jstqe.2003.820918.

[53] Saroch Leedumrongwatthanakun, Luca Innocenti, Hugo Defienne, Thomas Juffmann, Alessandro Ferraro, Mauro Paternostro, and Sylvain Gigan. "Programmable linear quantum networks with a multimode fibre". In: *Nature Photonics* 14.3 (Dec. 2019), pp. 139–142. DOI: 10.1038/s41566-019-0553-9. URL: https://doi.org/10.1038/s41566-019-0553-9.

[54] A. F. Abouraddy, G. Di Giuseppe, T. M. Yarnall, M. C. Teich, and B. E. A. Saleh. "Implementing one-photon three-qubit quantum gates using spatial light modulators". In: *Physical Review A* 86.5 (Nov. 2012). DOI: 10.1103/physreva.86.050303. URL: https://doi.org/10.1103/physreva.86.050303.

[55] Paul-Antoine Moreau, Ermes Toninelli, Thomas Gregory, and Miles J. Padgett. "Imaging with quantum states of light". In: *Nature Reviews Physics* 1.6 (May 2019), pp. 367–380. DOI: 10.1038/s42254-019-0056-0. URL: https://doi.org/10.1038/s42254-019-0056-0.

[56] Gabriela Barreto Lemos, Victoria Borish, Garrett D. Cole, Sven Ramelow, Radek Lapkiewicz, and Anton Zeilinger. "Quantum imaging with undetected photons". In: *Nature* 512.7515 (Aug. 2014), pp. 409–412. DOI: 10.1038/nature13586. URL: https://doi.org/10.1038/nature13586.

[57] Ayman F. Abouraddy, Patrick R. Stone, Alexander V. Sergienko, Bahaa E. A. Saleh, and Malvin C. Teich. "Entangled-Photon Imaging of a Pure Phase Object". In: *Physical Review Letters* 93.21 (Nov. 2004). DOI: 10.1103/physrevlett.93.213903. URL: https://doi.org/10.1103/physrevlett.93.213903.

[58] Vittorio Giovannetti, Seth Lloyd, and Lorenzo Maccone. "Quantum Metrology". In: *Physical Review Letters* 96.1 (Jan. 2006). DOI: 10.1103/physrevlett.96.010401. URL: https://doi.org/10.1103/physrevlett.96.010401.

[59] Michał Parniak, Sebastian Borówka, Kajetan Boroszko, Wojciech Wasilewski, Konrad Banaszek, and Rafał Demkowicz-Dobrzański. "Beating the Rayleigh Limit Using Two-Photon Interference". In: *Physical Review Letters* 121.25 (Dec. 2018). DOI: 10.1103/physrevlett.121.250503. URL: https://doi.org/10.1103/physrevlett.121.250503.

[60] Mankei Tsang, Ranjith Nair, and Xiao-Ming Lu. "Quantum Theory of Superresolution for Two Incoherent Optical Point Sources". In: *Physical Review X* 6.3 (Aug. 2016). DOI: 10.1103/physrevx.6.031033. URL: https://doi.org/10.1103/physrevx.6.031033.

[61] Radosław Chrapkiewicz, Michał Jachura, Konrad Banaszek, and Wojciech Wasilewski. "Hologram of a single photon". In: *Nature Photonics* 10.9 (July 2016), pp. 576–579. DOI: 10.1038/nphoton.2016.129. URL: https://doi.org/10.1038/nphoton.2016.129.

[62] Jeff S. Lundeen, Brandon Sutherland, Aabid Patel, Corey Stewart, and Charles Bamber. "Direct measurement of the quantum wavefunction". In: *Nature* 474.7350 (June 2011), pp. 188–191. DOI: 10.1038/nature10120. URL: https://doi.org/10.1038/nature10120.

[63] Mohammad Mirhosseini, Omar S. Magaña-Loaiza, Seyed Mohammad Hashemi Rafsanjani, and Robert W. Boyd. "Compressive Direct Measurement of the Quantum Wave Function". In: *Physical Review Letters* 113.9 (Aug. 2014). DOI: 10.1103/physrevlett.113.090402. URL: https://doi.org/10.1103/physrevlett.113.090402.

[64] Zhimin Shi, Mohammad Mirhosseini, Jessica Margiewicz, Mehul Malik, Freida Rivera, Ziyi Zhu, and Robert W. Boyd. "Scan-free direct measurement of an extremely high-dimensional photonic state". In: *Optica* 2.4 (Apr. 2015), p. 388. DOI: 10.1364/optica.2.000388. URL: https://doi.org/10.1364/optica.2.000388.

[65] D. F. McAlister, M. Beck, L. Clarke, A. Mayer, and M. G. Raymer. "Optical phase retrieval by phase-space tomography and fractional-order Fourier transforms". In: *Optics Letters* 20.10 (May 1995), p. 1181. DOI: 10.1364/ol.20.001181. URL: https://doi.org/10.1364/ol.20.001181.

[66] Brian J. Smith, I. A. Walmsley, K. Banaszek, Emmy Killett, and M. G. Raymer. "Measurement of the transverse spatial quantum state of light at the single-photon level". In: *Optics Letters* 30.24 (Dec. 2005), p. 3365. DOI: 10.1364/ol.30.003365. URL: https://doi.org/10.1364/ol.30.003365.

[67] A. I. Lvovsky and M. G. Raymer. "Continuous-variable optical quantum-state tomography". In: *Reviews of Modern Physics* 81.1 (Mar. 2009), pp. 299–332. DOI: 10.1103/revmodphys.81.299. URL: https://doi.org/10.1103/revmodphys.81.299.

[68] A. I. Lvovsky, H. Hansen, T. Aichele, O. Benson, J. Mlynek, and S. Schiller. "Quantum State Reconstruction of the Single-Photon Fock State". In: *Physical Review Letters* 87.5 (July 2001). DOI: 10.1103/physrevlett.87.050402. URL: https://doi.org/10.1103/physrevlett.87.050402.

[69] C. C. Leary, L. A. Baumgardner, and M. G. Raymer. "Stable mode sorting by two-dimensional parity of photonic transverse spatial states". In: *Optics Express* 17.4 (Feb. 2009), p. 2435. DOI: 10.1364/oe.17.002435. URL: https://doi.org/10.1364/oe.17.002435.

[70] Christopher E. Kuklewicz, Marco Fiorentino, Gaétan Messin, Franco N. C. Wong, and Jeffrey H. Shapiro. "High-flux source of polarization-entangled photons from a periodically poled $KTiOPO_4$ parametric down-converter". In: *Phys. Rev. A* 69 (1 2004), p. 013807. DOI: 10.1103/PhysRevA.69.013807. URL: https://link.aps.org/doi/10.1103/PhysRevA.69.013807.

[71] Michał Jachura and Radosław Chrapkiewicz. "Shot-by-shot imaging of Hong–Ou–Mandel interference with an intensified sCMOS camera". In: *Optics Letters* 40.7 (Mar. 2015), p. 1540. DOI: 10.1364/ol.40.001540. URL: https://doi.org/10.1364/ol.40.001540.

[72] Gabriel Popescu, Takahiro Ikeda, Ramachandra R. Dasari, and Michael S. Feld. "Diffraction phase microscopy for quantifying cell structure and dynamics". In: *Optics Letters* 31.6 (Mar. 2006), p. 775. DOI: 10.1364/ol.31.000775. URL: https://doi.org/10.1364/ol.31.000775.

[73] Jerome Mertz. *Introduction to Optical Microscopy*. 2nd ed. Cambridge: Cambridge University Press, 2019. DOI: 10.1017/9781108552660.

[74] Miguel Arevallilo Herráez, David R. Burton, Michael J. Lalor, and Munther A. Gdeisat. "Fast two-dimensional phase-unwrapping algorithm based on sorting by reliability following a noncontinuous path". In: *Applied Optics* 41.35 (Dec. 2002), p. 7437. DOI: 10.1364/ao.41.007437. URL: https://doi.org/10.1364/ao.41.007437.

[75] W J Bates. "A wavefront shearing interferometer". In: *Proceedings of the Physical Society* 59.6 (Nov. 1947), pp. 940–950–2. DOI: 10.1088/0959-5309/59/6/303. URL: https://doi.org/10.1088/0959-5309/59/6/303.

[76] Stephen M. Barnett, Mohamed Babiker, and Miles J. Padgett. "Optical orbital angular momentum". In: *Philosophical Transactions of the Royal Society A: Mathematical, Physical and Engineering Sciences* 375.2087 (Feb. 2017), p. 20150444. DOI: 10.1098/rsta.2015.0444. URL: https://doi.org/10.1098/rsta.2015.0444.

[77] Alex O. C. Davis, Valérian Thiel, Michał Karpiński, and Brian J. Smith. "Measuring the Single-Photon Temporal-Spectral Wave Function". In: *Physical Review Letters* 121.8 (Aug. 2018). DOI: 10.1103/physrevlett.121.083602. URL: https://doi.org/10.1103/physrevlett.121.083602.

[78] Ernst M. Rasel, Markus K. Oberthaler, Herman Batelaan, Jörg Schmiedmayer, and Anton Zeilinger. "Atom Wave Interferometry with Diffraction Gratings of Light". In: *Physical Review Letters* 75.14 (Oct. 1995), pp. 2633–2637. DOI: 10.1103/physrevlett.75.2633. URL: https://doi.org/10.1103/physrevlett.75.2633.

[79] Markus Arndt, Aigars Ekers, Wolf von Klitzing, and Hendrik Ulbricht. "Focus on modern frontiers of matter wave optics and interferometry". In: *New Journal of Physics* 14.12 (Dec. 2012), p. 125006. DOI: 10.1088/1367-2630/14/12/125006. URL: https://doi.org/10.1088/1367-2630/14/12/125006.

[80] Nils Trautmann, Gergely Ferenczi, Sarah Croke, and Stephen M Barnett. "Holographic quantum imaging: reconstructing spatial properties via two-particle interference". In: *Journal of Optics* 19.5 (Apr. 2017), p. 054005. DOI: 10.1088/2040-8986/aa67b6. URL: https://doi.org/10.1088/2040-8986/aa67b6.

[81] Manuel Erhard, Mario Krenn, and Anton Zeilinger. "Advances in high-dimensional quantum entanglement". In: *Nature Reviews Physics* 2.7 (June 2020), pp. 365–381. DOI: 10.1038/s42254-020-0193-5. URL: https://doi.org/10.1038/s42254-020-0193-5.

[82] Mehul Malik, Manuel Erhard, Marcus Huber, Mario Krenn, Robert Fickler, and Anton Zeilinger. "Multi-photon entanglement in high dimensions". In: *Nature Photonics* 10.4 (Feb. 2016), pp. 248–252. DOI: 10.1038/nphoton.2016.12. URL: https://doi.org/10.1038/nphoton.2016.12.

[83] Mario Krenn, Marcus Huber, Robert Fickler, Radek Lapkiewicz, Sven Ramelow, and Anton Zeilinger. "Generation and confirmation of a (100×100)-dimensional entangled quantum system". In: *Proceedings of the National Academy of Sciences* 111.17 (Mar. 2014), pp. 6243–6247. DOI: 10.1073/pnas.1402365111. URL: https://doi.org/10.1073/pnas.1402365111.

[84] Hugo Defienne, Bienvenu Ndagano, Ashley Lyons, and Daniele Faccio. "Polarization entanglement-enabled quantum holography". In: *Nature Physics* 17.5 (Feb. 2021), pp. 591–597. DOI: 10.1038/s41567-020-01156-1. URL: https://doi.org/10.1038/s41567-020-01156-1.

[85] M. Tse et al. "Quantum-Enhanced Advanced LIGO Detectors in the Era of Gravitational-Wave Astronomy". In: *Physical Review Letters* 123.23 (Dec. 2019). DOI: 10.1103/physrevlett.123.231107. URL: https://doi.org/10.1103/physrevlett.123.231107.

[86] Tamás Vértesi, Stefano Pironio, and Nicolas Brunner. "Closing the Detection Loophole in Bell Experiments Using Qudits". In: *Phys. Rev. Lett.* 104 (6 2010), p. 060401. DOI: 10.1103/PhysRevLett.104.060401. URL: https://link.aps.org/doi/10.1103/PhysRevLett.104.060401.

[87] Markus Burkhardt and Petra Schwille. "Electron multiplying CCD based detection for spatially resolved fluorescence correlation spectroscopy". In: *Optics Express* 14.12 (2006), p. 5013. DOI: 10.1364/oe.14.005013. URL: https://doi.org/10.1364/oe.14.005013.

[88] Olivier Daigle and Sébastien Blais-Ouellette. "Photon counting with an EMCCD". In: *SPIE Proceedings*. Ed. by Erik Bodegom and Valérie Nguyen. SPIE, Feb. 2010. DOI: 10.1117/12.840047. URL: https://doi.org/10.1117/12.840047.

[89] Ivan Michel Antolovic, Claudio Bruschini, and Edoardo Charbon. "Dynamic range extension for photon counting arrays". In: *Opt. Express* 26.17 (2018), pp. 22234–22248. DOI: 10.1364/OE.26.022234. URL: http://opg.optica.org/oe/abstract.cfm?URI=oe-26-17-22234.

[90] Bruno Eckmann, Bänz Bessire, Manuel Unternährer, Leonardo Gasparini, Matteo Perenzoni, and André Stefanov. "Characterization of space-momentum entangled photons with a time resolving CMOS SPAD array". In: *Optics Express* 28.21 (Oct. 2020), p. 31553. DOI: 10.1364/oe.401260. URL: https://doi.org/10.1364/oe.401260.

[91] M. Fisher-Levine and A. Nomerotski. "TimepixCam: a fast optical imager with time-stamping". In: *Journal of Instrumentation* 11.03 (2016), pp. C03016–C03016. DOI: 10.1088/1748-0221/11/03/c03016. URL: https://doi.org/10.1088/1748-0221/11/03/c03016.

[92] Andrei Nomerotski, I. Chakaberia, M. Fisher-Levine, Z. Janoska, P. Takacs, and T. Tsang. "Characterization of TimepixCam, a fast imager for the time-stamping of optical photons". In: *Journal of Instrumentation* 12.01 (2017), pp. C01017–C01017. DOI: 10.1088/1748-0221/12/01/c01017. URL: https://doi.org/10.1088/1748-0221/12/01/c01017.

[93] Baptiste Courme, Chloé Vernière, Peter Svihra, Sylvain Gigan, Andrei Nomerotski, and Hugo Defienne. *Quantifying high-dimensional spatial entanglement with a single-photon-sensitive time-stamping camera*. arXiv:2302.03756 [quant-ph] (2023). DOI: 10.48550/ARXIV.2302.03756. URL: https://arxiv.org/abs/2302.03756.

[94] Michał Jachura and Radosław Chrapkiewicz. "Shot-by-shot imaging of Hong-Ou-Mandel interference with an intensified sCMOS camera". In: *Opt. Lett.* 40.7 (2015), pp. 1540–1543. DOI: 10.1364/OL.40.001540. URL: http://opg.optica.org/ol/abstract.cfm?URI=ol-40-7-1540.

[95] Sanjukta Kundu, Jerzy Szuniewicz, Grzegorz Firlik, and Radek Lapkiewicz. "Single-photon camera with an adaptively gated image intensifier". In: *Frontiers in Optics + Laser Science 2022 (FIO, LS)*. Optica Publishing Group, 2022. DOI: 10.1364/fio.2022.fm3c.2. URL: https://doi.org/10.1364/fio.2022.fm3c.2.

[96] Suk Kyoung Lee, Fadia Cudry, Yun Fei Lin, Steven Lingenfelter, Alexander H. Winney, Lin Fan, and Wen Li. "Coincidence ion imaging with a fast frame camera". In: *Review of Scientific Instruments* 85.12 (Dec. 2014), p. 123303. DOI: 10.1063/1.4903856. URL: https://doi.org/10.1063/1.4903856.

[97] James Schneeloch and John C Howell. "Introduction to the transverse spatial correlations in spontaneous parametric down-conversion through the biphoton birth zone". In: *Journal of Optics* 18.5 (Apr. 2016), p. 053501. DOI: 10.1088/2040-8978/18/5/053501. URL: https://doi.org/10.1088/2040-8978/18/5/053501.

[98] Michał Lipka, Michał Parniak, and Wojciech Wasilewski. "Microchannel plate cross-talk mitigation for spatial autocorrelation measurements". In: *Applied Physics Letters* 112.21 (May 2018), p. 211105. DOI: 10.1063/1.5033559. URL: https://doi.org/10.1063/1.5033559.

[99] Bienvenu Ndagano, Hugo Defienne, Dominic Branford, Yash D. Shah, Ashley Lyons, Niclas Westerberg, Erik M. Gauger, and Daniele Faccio. "Quantum microscopy based on Hong–Ou–Mandel interference". In: *Nature Photonics* 16.5 (Apr. 2022), pp. 384–389. DOI: 10.1038/s41566-022-00980-6. URL: https://doi.org/10.1038/s41566-022-00980-6.

[100] Alberto Peruzzo, Mirko Lobino, Jonathan C. F. Matthews, Nobuyuki Matsuda, Alberto Politi, Konstantinos Poulios, Xiao-Qi Zhou, Yoav Lahini, Nur Ismail, Kerstin Wörhoff, Yaron Bromberg, Yaron Silberberg, Mark G. Thompson, and Jeremy L. OBrien. "Quantum Walks of Correlated Photons". In: *Science* 329.5998 (Sept. 2010), pp. 1500–1503. DOI: 10.1126/science.1193515. URL: https://doi.org/10.1126/science.1193515.

[101] Hugo Defienne, Marco Barbieri, Ian A. Walmsley, Brian J. Smith, and Sylvain Gigan. "Two-photon quantum walk in a multimode fiber". In: *Science Advances* 2.1 (Jan. 2016). DOI: 10.1126/sciadv.1501054. URL: https://doi.org/10.1126/sciadv.1501054.

[102] W. H. Peeters, J. J. D. Moerman, and M. P. van Exter. "Observation of Two-Photon Speckle Patterns". In: *Physical Review Letters* 104.17 (Apr. 2010). DOI: 10.1103/physrevlett.104.173601. URL: https://doi.org/10.1103/physrevlett.104.173601.

[103] Ohad Lib and Yaron Bromberg. "Quantum light in complex media and its applications". In: *Nature Physics* 18.9 (Sept. 2022), pp. 986–993. DOI: 10.1038/s41567-022-01692-y. URL: https://doi.org/10.1038/s41567-022-01692-y.

[104] "Photonic implementation of boson sampling: a review". In: *Advanced Photonics* 1.03 (May 2019), p. 1. DOI: 10.1117/1.ap.1.3.034001. URL: https://doi.org/10.1117/1.ap.1.3.034001.

[105] Mayukh Lahiri, Radek Lapkiewicz, Gabriela Barreto Lemos, and Anton Zeilinger. "Theory of quantum imaging with undetected photons". In: *Physical Review A* 92.1 (July 2015). DOI: 10.1103/physreva.92.013832. URL: https://doi.org/10.1103/physreva.92.013832.

[106] Andrew G. White, Jay R. Mitchell, Olaf Nairz, and Paul G. Kwiat. ""Interaction-free" imaging". In: *Physical Review A* 58.1 (July 1998), pp. 605–613. DOI: 10.1103/physreva.58.605. URL: https://doi.org/10.1103/physreva.58.605.

[107] D. V. Strekalov, A. V. Sergienko, D. N. Klyshko, and Y. H. Shih. "Observation of Two-Photon "Ghost" Interference and Diffraction". In: *Physical Review Letters* 74.18 (May 1995), pp. 3600–3603. DOI: 10.1103/physrevlett.74.3600. URL: https://doi.org/10.1103/physrevlett.74.3600.

[108] T. B. Pittman, Y. H. Shih, D. V. Strekalov, and A. V. Sergienko. "Optical imaging by means of two-photon quantum entanglement". In: *Physical Review A* 52.5 (Nov. 1995), R3429–R3432. DOI: 10.1103/physreva.52.r3429. URL: https://doi.org/10.1103/physreva.52.r3429.

[109] Nathaniel R. Miller, Sven Ramelow, and William N. Plick. "Versatile Super-Sensitive Metrology Using Induced Coherence". In: *Quantum* 5 (May 2021), p. 458. DOI: 10.22331/q-2021-05-26-458. URL: https://doi.org/10.22331/q-2021-05-26-458.

[110] G. Brida, M. Genovese, and I. Ruo Berchera. "Experimental realization of sub-shot-noise quantum imaging". In: *Nature Photonics* 4.4 (Feb. 2010), pp. 227–230. DOI: 10.1038/nphoton.2010.29. URL: https://doi.org/10.1038/nphoton.2010.29.

[111] Catxere A. Casacio, Lars S. Madsen, Alex Terrasson, Muhammad Waleed, Kai Barnscheidt, Boris Hage, Michael A. Taylor, and Warwick P. Bowen. "Quantum-enhanced nonlinear microscopy". In: *Nature* 594.7862 (June 2021), pp. 201–206. DOI: 10.1038/s41586-021-03528-w. URL: https://doi.org/10.1038/s41586-021-03528-w.

[112] J. Sabines-Chesterking, A. R. McMillan, P. A. Moreau, S. K. Joshi, S. Knauer, E. Johnston, J. G. Rarity, and J. C. F. Matthews. "Twin-beam sub-shot-noise raster-scanning microscope". In: *Optics Express* 27.21 (Oct. 2019), p. 30810. DOI: 10.1364/oe.27.030810. URL: https://doi.org/10.1364/oe.27.030810.

[113] Manuel Unternährer, Bänz Bessire, Leonardo Gasparini, Matteo Perenzoni, and André Stefanov. "Super-resolution quantum imaging at the Heisenberg limit". In: *Optica* 5.9 (Sept. 2018), p. 1150. DOI: 10.1364/optica.5.001150. URL: https://doi.org/10.1364/optica.5.001150.

[114] Ivan F. Santos, M. A. Sagioro, C. H. Monken, and S. Pádua. "Resolution and apodization in images generated by twin photons". In: *Physical Review A* 67.3 (Mar. 2003). DOI: 10.1103/physreva.67.033812. URL: https://doi.org/10.1103/physreva.67.033812.

[115] Emanuele Polino, Mauro Valeri, Nicolò Spagnolo, and Fabio Sciarrino. "Photonic quantum metrology". In: *AVS Quantum Science* 2.2 (June 2020), p. 024703. DOI: 10.1116/5.0007577. URL: https://doi.org/10.1116/5.0007577.

[116] Géza Tóth and Iagoba Apellaniz. "Quantum metrology from a quantum information science perspective". In: *Journal of Physics A: Mathematical and Theoretical* 47.42 (2014), p. 424006. DOI: 10.1088/1751-8113/47/42/424006. URL: https://dx.doi.org/10.1088/1751-8113/47/42/424006.

[117] Gabriela Barreto Lemos, Mayukh Lahiri, Sven Ramelow, Radek Lapkiewicz, and William N. Plick. "Quantum imaging and metrology with undetected photons: tutorial". In: *J. Opt. Soc. Am. B* 39.8 (2022), pp. 2200–2228. DOI: 10.1364/JOSAB.456778. URL: https://opg.optica.org/josab/abstract.cfm?URI=josab-39-8-2200.

[118] Anna V. Paterova, Dmitry A. Kalashnikov, Egor Khaidarov, Hongzhi Yang, Tobias W. W. Mass, Ramón Paniagua-Domínguez, Arseniy I. Kuznetsov, and Leonid A. Krivitsky. "Non-linear interferometry with infrared metasurfaces". In: *Nanophotonics* 10.6 (2021), pp. 1775–1784. DOI: doi:10.1515/nanoph-2021-0011. URL: https://doi.org/10.1515/nanoph-2021-0011.

[119] L. J. Wang, X. Y. Zou, and L. Mandel. "Induced coherence without induced emission". In: *Physical Review A* 44.7 (Oct. 1991), pp. 4614–4622. DOI: 10.1103/physreva.44.4614. URL: https://doi.org/10.1103/physreva.44.4614.

[120] Armin Hochrainer, Mayukh Lahiri, Radek Lapkiewicz, Gabriela B. Lemos, and Anton Zeilinger. "Interference fringes controlled by noninterfering photons". In: *Optica* 4.3 (2017), pp. 341–344. DOI: 10.1364/OPTICA.4.000341. URL: https://opg.optica.org/optica/abstract.cfm?URI=optica-4-3-341.

[121] Armin Hochrainer, Mayukh Lahiri, Manuel Erhard, Mario Krenn, and Anton Zeilinger. "Quantum indistinguishability by path identity and with undetected photons". In: *Rev. Mod. Phys.* 94 (2 2022), p. 025007. DOI: 10.1103/RevModPhys.94.025007. URL: https://link.aps.org/doi/10.1103/RevModPhys.94.025007.

[122] David C. Burnham and Donald L. Weinberg. "Observation of Simultaneity in Parametric Production of Optical Photon Pairs". In: *Physical Review Letters* 25.2 (July 1970), pp. 84–87. DOI: 10.1103/physrevlett.25.84. URL: https://doi.org/10.1103/physrevlett.25.84.

[123] Jian-Wei Pan, Zeng-Bing Chen, Chao-Yang Lu, Harald Weinfurter, Anton Zeilinger, and Marek Żukowski. "Multiphoton entanglement and interferometry". In: *Reviews of Modern Physics* 84.2 (May 2012), pp. 777–838. DOI: 10.1103/revmodphys.84.777. URL: https://doi.org/10.1103/revmodphys.84.777.

[124] Jorge Fuenzalida, Armin Hochrainer, Gabriela Barreto Lemos, Evelyn A. Ortega, Radek Lapkiewicz, Mayukh Lahiri, and Anton Zeilinger. "Resolution of Quantum Imaging with Undetected Photons". In: *Quantum* 6 (Feb. 2022), p. 646. DOI: 10.22331/q-2022-02-09-646. URL: https://doi.org/10.22331/q-2022-02-09-646.

[125] C. H. Monken, P. H. Souto Ribeiro, and S. Pádua. "Transfer of angular spectrum and image formation in spontaneous parametric down-conversion". In: *Phys. Rev. A* 57 (4 1998), pp. 3123–3126. DOI: 10.1103/PhysRevA.57.3123. URL: https://link.aps.org/doi/10.1103/PhysRevA.57.3123.

[126] Ichirou Yamaguchi and Tong Zhang. "Phase-shifting digital holography". In: *Optics Letters* 22.16 (Aug. 1997), p. 1268. DOI: 10.1364/ol.22.001268. URL: https://doi.org/10.1364/ol.22.001268.

[127] Sebastian Töpfer, Marta Gilaberte Basset, Jorge Fuenzalida, Fabian Steinlechner, Juan P. Torres, and Markus Gräfe. "Quantum holography with undetected light". In: *Science Advances* 8.2 (Jan. 2022). DOI: 10.1126/sciadv.abl4301. URL: https://doi.org/10.1126/sciadv.abl4301.

[128] Wei Li and Shengmei Zhao. "Generation of two-photon orbital-angular-momentum entanglement with a high degree of entanglement". In: *Applied Physics Letters* 114.4 (Jan. 2019). DOI: 10.1063/1.5081779. URL: https://doi.org/10.1063/1.5081779.

[129] J. P. Torres, A. Alexandrescu, and Lluis Torner. "Quantum spiral bandwidth of entangled two-photon states". In: *Physical Review A* 68.5 (Nov. 2003). DOI: 10.1103/physreva.68.050301. URL: https://doi.org/10.1103/physreva.68.050301.

[130] J. Romero, D. Giovannini, S. Franke-Arnold, S. M. Barnett, and M. J. Padgett. "Increasing the dimension in high-dimensional two-photon orbital angular momentum entanglement". In: *Physical Review A* 86.1 (July 2012). DOI: 10.1103/physreva.86.012334. URL: https://doi.org/10.1103/physreva.86.012334.

[131] Robert Fickler, Radek Lapkiewicz, William N. Plick, Mario Krenn, Christoph Schaeff, Sven Ramelow, and Anton Zeilinger. "Quantum Entanglement of High Angular Momenta". In: *Science* 338.6107 (Nov. 2012), pp. 640–643. DOI: 10.1126/science.1227193. URL: https://doi.org/10.1126/science.1227193.

[132] Inna Kviatkovsky, Helen M. Chrzanowski, Ellen G. Avery, Hendrik Bartolomaeus, and Sven Ramelow. "Microscopy with undetected photons in the mid-infrared". In: *Science Advances* 6.42 (Oct. 2020). DOI: 10.1126/sciadv.abd0264. URL: https://doi.org/10.1126/sciadv.abd0264.